Florida State University Libraries

Electronic Theses, Treatises and Dissertations The Graduate School

2019

Understanding Microphysics of Snowflakes and Snow Precipitation Process Using Spaceborne Microwave Measurements

Mengtao Yin

Follow this and additional works at the DigiNole: FSU's Digital Repository. For more information, please contact lib-ir@fsu.edu

FLORIDA STATE UNIVERSITY

COLLEGE OF ARTS AND SCIENCES

UNDERSTANDING MICROPHYSICS OF SNOWFLAKES AND SNOW PRECIPITATION PROCESS USING SPACEBORNE MICROWAVE MEASUREMENTS

By

MENGTAO YIN

A Dissertation submitted to the
Department of Earth, Ocean and Atmospheric Sciences
in partial fulfillment of the
requirements for the degree of
Doctor of Philosophy

2019

Mengtao Yin defended this dissertation on March 07, 2019.
The members of the supervisory committee were:

Guosheng Liu
Professor Directing Dissertation

Eric Chicken
University Representative

Jon E. Ahlquist
Committee Member

Mark A. Bourassa
Committee Member

Ming Cai
Committee Member

The Graduate School has verified and approved the above-named committee members, and certifies that the dissertation has been approved in accordance with university requirements

ACKNOWLEDGMENTS

First and most importantly, I would like to express my particular appreciation to my major advisor, Professor Guosheng Liu. He gave me a precious opportunity to continue my PhD degree in this department. I really received a good training and a lot of useful advices on research from Professor Liu. The experience working with him is unforgettable.

Special acknowledgement is also given to Professor Ming Cai, one of my committee member. He really helped me a lot in preparing my master thesis and beginning my PhD study.

I would like to thank my rest of committee members, Professor Eric Chicken, Professor John Ahlquist and Professor Mark Bourassa for their insightful comments and meaningful questions.

I would like to thank all members in Dr. Liu's lab for their support. They are Yulan Hong, Ryan Honeyager, Beth Sims, Jiamei Li and Shangyong Shi. I also acknowledge my friends at FSU, who make my life better.

Finally, I would like to thank my family members, who always understood and supported me during the period of my PhD study.

TABLE OF CONTENTS

List of Tables vi

List of Figures vii

Abstract xi

1 Introduction and Background 1

2 Theoretical Basis for Snowfall Remote Sensing 5

2.1 Radiative Properties of Snow Clouds 5

2.2 Active and Passive Microwave Remote Sensing 7

3 Instrument Characteristics and Coincident Dataset 11

3.1 Satellite Instrument Characteristics 11

3.2 CloudSat–GPM Coincidence Dataset 13

4 Triple Frequency Radar Signature Analysis 16

4.1 Introduction 16

4.2 Data Sources and Methods 17

4.2.1 Satellite and Analysis Data 17

4.2.2 Attenuation Correction on Radar Reflectivity 19

4.2.3 Data Selection 20

4.3 Discussion on Triple-frequency Radar Signatures 21

4.3.1 Observed Difference between Stratiform and Convective Cases 21

4.3.2 Modeled Triple-frequency Signatures 23

4.3.3 Statistics of Particle Type versus Temperature 28

4.4 Conclusions for Triple-frequency Radar Signature Analysis 29

5 Assessment of GPM High Frequency Microwave Measurements 36

5.1. Introduction 36

5.2 Data and Methods 39

5.2.1 Data Sources 39

5.2.2 Data Processing 41

5.2.3 Input Hydrometeor Profiles 42

5.2.4 Radiative Transfer Model 45

5.3. GMI Bias Characteristics at 166 and 183 GHz 45

5.4. Analysis of GMI Remaining Biases at 166 and 183 GHz 48

5.5. Conclusions for Assessment of Microwave High Frequency Measurements 51

6 Snowfall Retrieval Algorithm for GPM Microwave Imager 66

6.1 Introduction 66

6.2 Data Sources and Method 69

6.2.1 Data Sources and Processing 70

6.2.2 Initial Hydrometeor Profiles 71

6.2.3 Radiative Transfer Model 72

6.3. Developing Database Using 1D-Var Optimization 72

6.3.1 1D–Var Optimization Method 72

6.3.2 Case Studies 76

6.3.3 Statistics of the Constructed *a priori* Database 78

6.4. Applying Database to Bayesian Retrieval 81

6.4.1 Bayesian Retrieval Method 81

6.4.2 Retrieval Results 83

6.5 Conclusions for Passive Microwave Snowfall Retrieval Algorithm 87

7 Summary and Discussions 109

Bibliography 113

Biographical Sketch 122

LIST OF TABLES

3.1 Specifications of GMI channels at 89 GHz and higher frequencies. 14

5.1 Biases and standard deviations of O–B for GMI channels at 166 and 183 GHz under clear–sky and snowfall conditions. 54

LIST OF FIGURES

2.1 Imaginary part of refractive index of water and ice for a microwave wavelength range from 0.1 to 100 mm. 9

2.2 Normalized backscatter cross sections at 13.6 GHz (left panel), 35.5 GHz (middle panel) and 94 GHz (right panel) for selected snow particles..... 10

2.3 Simulated brightness temperatures from 80 to 200 GHz at nadir for different weather conditions. 10

3.1 An example of collocation among CPR, DPR and GMI (166 GHz) footprints on June 07, 2014..... 14

3.2 Vertical cross sections of (a) CPR, (b) DPR Ku NS, (c) Ka MS and (d) Ka HS radar reflectivities as well as (e) GMI brightness temperatures at 89 GHz and higher frequencies for a single case on March 09, 2014..... 15

4.1 Normalized occurrence frequencies of observed triple-frequency signatures (shading) for stratiform and convective cases in 1 dB × 1 dB boxes with time differences between CPR and DPR smaller than 7.5 minutes (top panels) and larger than 7.5 minutes (bottom panels). 30

4.2 Same as Fig. 4.1 except that x-axis is DFR Ku/W..... 31

4.3 Modeled triple-frequency signatures for large particles (Λ= 1 cm^{-1}) and small particles (Λ = 7 cm^{-1}). 32

4.4 Model triple-frequency signatures (black lines) and normalized occurrence frequencies of observed triple-frequency signatures (shading) in 1 dB × 1 dB boxes for stratiform and convective cases. 33

4.5 Relative frequencies of classified snowflake types for stratiform and convective cases using set 1 (DFR Ku/Ka and Ka/W) and set 2(DFR Ku/Ka and Ku/W)..... 34

4.6 Relative frequency distributions of classified snowflake types over temperature intervals for stratiform and convective cases using set 1 (top panels) and set 2 (bottom panels)..... 35

5.1 Jacobians of GMI channels at 166V/H, 183.31±3V, and 183.31±7V GHz with respect to snow water content. 54

5.2 Number of clear–sky (top panels), cloudy without precipitation (middle panels) and snowfall (bottom panels) data points within 5°×5° boxes. 55

5.3 Vertical cross section of CPR derived snow water content for a single case on April 11, 2015 (top panel) and GMI brightness temperature depressions at 166 and 183 GHz (bottom panel)..... 56

5.4 Biases (top panel) and standard deviations (bottom panel) of observed minus simulated brightness temperature (O–B) for GMI channels at 166 and 183 GHz under clear–sky, cloudy without precipitation and snowfall conditions. Only data points with latitudes poleward of 40° are included..... 57

5.5 Relation between observed minus simulated brightness temperature (O–B) and simulated brightness temperatures (B) for GMI channels at 166 and 183 GHz under clear–sky (left panels) and snowfall (right panels) conditions. Shading represents the occurrence frequency. 58

5.6 Biases of observed minus simulated brightness temperature (O–B) for GMI channels at 166 and 183 GHz under the snowfall condition assuming different snow particle types in the radiative transfer model 59

5.7 Same as Fig. 5.6 except for standard deviations. 60

5.8 Dependence of observed minus simulated brightness temperature (O–B) on ice water path (IWP) for GMI channels at 166 and 183 GHz under snowfall conditions. Shading represents the occurrence frequency. 61

5.9 Same as Fig. 5.8 except for dependence on snow water path (SWP). 61

5.10 Biases of observed minus simulated brightness temperature (O–B) in two–dimensional space of ice and snow water paths for GMI channels at 166 and 183 GHz under snowfall conditions. 62

5.11 Dependence of biases of observed minus simulated brightness temperature (O–B) on snow top height for GMI channels at 166 and 183 GHz under snowfall conditions. The length of the bar represents the twofold of standard deviations of observed minus simulated brightness temperature (O–B). 63

5.12 Dependence of biases of observed minus simulated brightness temperature (O–B) on snow layer depth for GMI channels at 166 and 183 GHz under snowfall conditions. The length of the bar represents the twofold of standard deviations of observed minus simulated brightness temperature (O–B). 64

5.13 A case for shallow snow clouds on June 12, 2015 (top panel) and a case for deep convective snow clouds on March 11, 2015 (bottom panel). 65

6.1 Flowchart for developing an *a priori* database for passive microwave snowfall retrievals over ocean using 1D–Var optimization method. SWC: snow water content. BT: brightness temperature. 90

6.2 Z_e–SWC relations for average 1 (sector, dendrite, and aggregate), average 2 (rosettes, sector, and dendrite), and average 3 (sector and aggregate)..... 91

6.3 Four vertical profiles of snow water content from CPR initial estimate using Z_e–SWC relation in (6.1) (black solid curve), CPR initial estimate using Z_e–SWC relation in (6.3) (black dash curve), analysis using Z_e–SWC relation in (6.1) (blue curve), and analysis using Z_e–SWC relation in (6.3) (red curve). Only Braham relation is employed..... 92

6.4 Four vertical profiles of snow water content from CPR initial estimate (black curve), analysis using Braham relation (blue curve), analysis using Rutledge and Hobbs relation (red curve), and analysis using Braham relation with a channel subset excluding 166 GHz (green curve). 93

6.5 Vertical cross sections of snow water content from (a) CPR initial estimate, (b) analysis using Braham relation, (c) analysis using Rutledge and Hobbs relation, and (d) analysis using Braham relation with a channel subset excluding 166 GHz for a case on March 11, 2015. 94

6.6 Relations between observed (O) and simulated (B or A) brightness temperatures for GMI channels at 89 GHz and higher frequencies with snow water content profiles of CPR initial estimate (left column) and analysis (right column) as input to radiative transfer model. The shading represents the occurrence frequency. 95

6.7 Standard deviations of observed (O) minus simulated (B or A) brightness temperature for GMI channels at 89 GHz and higher frequencies, grouped for data with $\Delta T_b^{166V} > 1$ K (top panel) and $\Delta T_b^{166V} < 1$ K (bottom panel), with snow water content profiles of CPR initial estimate (blue) and analysis (red) as input to radiative transfer model. 97

6.8 Frequency distributions of analyzed snow water content profiles in terms of total precipitable water (top panel) and 2–m air temperature (bottom panel). 98

6.9 Number of analyzed snow water content profiles within 5°×5° boxes. 99

6.10 Contoured frequency by altitude diagrams for analyzed snow water content profiles. 99

6.11 Occurrence frequency distributions of analyzed surface snow water content (red), retrieved surface snow water content using all profiles (yellow), retrieved surface snow water content using clear–sky and snowfall profiles (green), and retrieved surface snow water content using snowfall profiles (blue). 100

6.12 Vertical cross sections of (a) analyzed snow water content, retrieved snow water content using (b) full database, (c) subsets of the database with moisture constraint, (d) subsets of the database with temperature constraint, (e) CPR initial snow water content, and (f) retrieved snow water content using CPR initial estimate as database for a case on March 11, 2015..... 101

6.13 Same as Fig. 6.12 except for a single case on December 5, 2014. 103

6.14 Northern hemisphere mean distributions of surface snow water content within 5°×5° boxes over ocean for year 2015 retrieved from (a) CPR radar reflectivities, and GMI brightness temperatures using (b) full database, (c) subsets of the database with moisture constraint, (d) subsets of the database with temperature constraint, and (e) CPR initial snow water content profiles as database. 105

6.15 Same as Fig. 6.14 except for southern hemisphere..... 106

6.16 Differences of northern hemisphere mean surface snow water contents within 5°×5° boxes over ocean for year 2015 between those retrieved from CPR radar reflectivities and those retrieved from GMI brightness temperatures using (a) full database, (b) subsets of the database with moisture constraint, (c) subsets of the database with temperature constraint, and (d) CPR initial snow water content profiles as database..... 107

6.17 Same as Fig. 6.16 except for southern hemisphere..... 108

ABSTRACT

Snow, another precipitation form besides rain, affects the Earth's climate distinctly by modifying hydrological and radiative processes. The radiative properties of nonspherical snowflakes are much more complicated than their spherical counterparts, raindrops. Snowflakes with different structures tend to have different scattering properties. Thus it is important for us to enhance the knowledge in falling snow. However, only a few sensors have been available so far that can provide global snowfall measurements including those onboard he Global Precipitation Measurement (GPM) core observatory and the CloudSat satellites. The GPM satellite carries two important instruments for studying snow precipitations, i.e., the Dual–frequency Precipitation Radar (DPR) and the GPM Microwave Imager (GMI). By combining the GPM instruments with another active sensor onboard the CloudSat satellite, the Cloud Profiling Radar (CPR), an unprecedented opportunity arises for understanding the microphysics of snowflakes and the physical processes of snow precipitation. Seizing this opportunity, in this study, we firstly investigate the microphysical properties of snow particles by analyzing their backscattered signatures at different frequencies. Then, the accuracy of simulating passive microwave brightness temperatures at high frequencies is examined under snowfall conditions using the CPR derived snow water content profiles as radiative transfer model inputs. Lastly, a passive microwave snowfall retrieval method is developed in which the *a priori* database is optimized by tuning snow water content profiles to be consistent with the GMI observations.

To understand the microphysical properties of snow clouds, the triple-frequency radar signatures derived from the DPR and CPR collocated measurements are analyzed. It is noticed that there is a clear difference in triple-frequency radar signatures between stratiform and convective clouds. Through modeling experiments, it is found that the triple-frequency radar

signatures are closely related to the size and bulk density of snow particles. The observed difference in triple-frequency radar signatures are mainly attributed to the difference in prevalent particle modes between stratiform and convective clouds, i.e., stratiform snow clouds contain abundant large unrimed particles with low density, while dense small rimed particles are prevalent in convective clouds.

To assess the accuracy of radiative transfer simulation for passive microwave high frequency channels under snowfall conditions, we evaluate the biases between observed and simulated brightness temperatures for GMI channels at 166 and 183 GHz. A radiative transfer model is used, which is capable to handle the scattering properties of nonspherical snowflakes. As inputs to the radiative transfer model, the snow water content profiles are derived from the CPR measurements. The results indicate that the overall biases of observed minus simulated brightness temperatures are generally smaller than 1 K except for the 166 GHz horizontal polarization (166H) channel. Large biases for GMI channels are found under scenes of low brightness temperatures. Further investigations indicate that the remaining biases for GMI channels are associated with specific cloud types. In shallow clouds, errors in cloud liquid water profiles are likely responsible for the large positive bias at the 166H channel. In deep convective clouds, strong attenuation in CPR radar reflectivities and possible sampling bias both contribute to the GMI remaining negative biases.

A snowfall retrieval algorithm is then developed for GMI observations. The data sources and processing methods are adopted from the above study of GMI bias characterization. First, an *a priori* database is created which contains the snow water content profiles and their corresponding brightness temperatures simulated for GMI channels. A one–dimensional variational (1D–Var) method is employed to optimize the CPR derived snow water content

profiles. The so developed *a priori* database is applied in a Bayesian retrieval algorithm. The retrieval results show that the 1D–Var optimization can improve the vertical structure of retrieved snow water content. Additionally, this method can bring the global mean distribution of GMI retrieved surface snow water closer to the CPR estimates.

This research explores the application of spaceborne microwave measurements to snowfall studies by combining CloudSat and GPM instruments. It provides new knowledge on snowflake microphysics and applicable methods in retrieving three–dimensional snow water distribution from passive high frequency microwave measurements.

CHAPTER 1

INTRODUCTION AND BACKGROUND

Snow is a dominant precipitation form at high latitudes during winter seasons [*Levizzani et al.*, 2011]. It has a distinctive impact on hydrological and climatological cycles [*Liu*, 2008a]. Falling snow over ocean can affect the deep–water formation by the complex interaction with ocean surface [*Curry et al.*, 1996; *Liu and Curry*, 1997]. The modulation of surface albedo by snow cover affects the energy budget [*Trenberth et al.*, 2007]. Therefore, studying snow precipitation allows us to better manage water resource and understand the global energy balance [*Hou et al.*, 2014]. Historically, ground-based instruments have provided most of the hitherto snowfall information. However, the scarcity of these instruments over ocean and unpopulated areas prevents a comprehensive measurement of global snowfall events [*Heymsfield et al.*, 2017]. To study snow precipitation globally, satellite instruments are clearly in demand [*Kidd and Levizzani*, 2011].

Unlike satellite rainfall studies that have a long history of development [*Adler et al.*, 2001; *Kummerow et al.*, 2001], satellite snowfall studies are still in an early stage. Not many sensors are suitable for detecting falling snow. Early studies mainly utilized passive microwave instruments with channels at 85 GHz and higher frequencies to detect global snowfall events [*Liu and Curry*, 1997; *Skofronick-Jackson et al.*, 2004; *Noh et al.*, 2006] until the launch of CloudSat satellite in 2006 that carried the first spaceborne active sensor at 94 GHz, the Cloud Profiling Radar (CPR) [*Stephens et al.*, 2002]. *Liu* [2008a] firstly derived the global snow cloud characteristics from the CPR radar reflectivities. Subsequently, several snowfall studies utilized the CPR measurements to retrieve global snowfall information and demonstrated that the CPR is able to detect the snow scattering signatures in light snowfall events [*Hiley et al.*, 2011;

Skofronick-Jackson et al., 2013; *Wood et al.*, 2014]. Although the CPR is more sensitive to precipitating particles than passive microwave instruments, it suffers from significant attenuation in deep convective clouds [*Cao et al.*, 2014]. It was also mentioned by *Liu and Seo* [2013] that the CPR only observes a strip of 1.5 km width on the ground for each satellite orbit, since it is not a scanning instrument. These drawbacks largely limit the application of CPR measurements on snowfall studies.

In 2014, the Global Precipitation Measurement (GPM) core satellite [*Hou et al.*, 2014] was successfully launched by National Aeronautics and Space Administration (NASA) and Japan Aerospace Exploration Agency (JAXA). The carried Dual–frequency Precipitation Radar (DPR) is a first spaceborne radar that consists of Ku and Ka bands. While its main goal is to improve the global rainfall estimations [*Hou et al.*, 2014], the radar measurements at Ku and Ka bands will provide the essential information of heavy snowfall events, since the impact of attenuation on Ku and Ka bands is relatively small [*Kneifel et al.*, 2011]. The combination of Ku and Ka bands also allows the quantification of precipitation particle size distribution. The carried GPM Microwave Imager (GMI), as a successor of the Tropical Rainfall Measuring Mission (TRMM) Microwave Imager (TMI), provides the global microwave radiance measurements with unprecedentedly high spatial resolution. At 89 GHz and higher frequencies, the spatial resolutions of GMI channels (~ 6 km) are one order higher than other microwave instruments sharing similar channels, such as the Special Sensor Microwave Imager/Sounder (SSMIS) [*Kunkee et al.*, 2008] onboard the Defense Meteorological Satellite Program (DMSP) satellites and the Advanced Technology Microwave Sounder (ATMS) [*Weng et al.*, 2012] onboard the Suomi National Polar–orbiting Partnership (NPP) satellite. Utilizing the DPR and GMI

measurements is greatly beneficial for understanding the microphysics of snowflakes and the snow precipitation process.

While applying the DPR and GMI measurements has a great potential in improving snowfall studies, we need to pay attention to their limitations. As shown by *Hamada and Takayabu* [2015], the post–launch DPR Ku band sensitivity is about 12 dBZ and 13 dBZ over ocean and land, respectively. *Kubota et al.* [2016] also discussed the sidelobe clutter effect of DPR which further impedes the use of DPR radar reflectivity, since DPR is a scanning instrument. As a result, the DPR tends to miss most light and moderate snowfall events [*Casella et al.*, 2017]. On the other hand, while the GMI provides the precious radiance measurements at 166 and 183 GHz, it is challenging to simulate brightness temperatures at those channels by radiative transfer models, which have been included as a part of many recent snowfall retrieval algorithms [*Kummerow et al.*, 2015; *Meng et al.*, 2017].

As discussed above, any single spaceborne instrument has its specific limitation. It is desirable to find an approach to maximize the capabilities in detecting snow scattering signatures by combining measurements from multiple sensors onboard different satellites, since the particular limitation of a single sensor can be alleviated by simultaneously using other sensors. Recently, several studies employing radar measurements at three frequencies have demonstrated that the triple-frequency radar signatures are closely related to the microphysics of snowflakes [*Kneifel et al.*, 2011; *Leinonen et al.*, 2012; *Stein et al.*, 2014]. In addition, several previous studies explored the joint use of spaceborne active and passive microwave instruments for snowfall retrievals [*Liu and Seo*, 2013; *Seo et al.*, 2016; *Rysman et al.*, 2018]. Their encouraging results have indicated that the combination of active and passive microwave sensors can reduce the uncertainty in snowfall retrievals. Inspired by those studies, we will explore the methods to

make the full use of satellite microwave measurements for snowfall studies. Specifically, we will examine the spaceborne triple-frequency radar signatures by combining the DPR and CPR radar reflectivities. In addition, we will use the GMI brightness temperature and CPR radar reflectivity measurements to develop a snowfall retrieval algorithm that includes the model simulations of GMI high frequency channels.

The remainder of this dissertation is organized as follows. Chapter 2 provides the theoretical basis for active and passive microwave snowfall detection. In chapter 3, the primary instrument characteristics and the coincident dataset of GPM and CloudSat are introduced. Chapter 4 gives the triple-frequency radar signature analysis. Chapter 5 provides the assessment of GPM high frequency measurements with radiative transfer simulations under snowfall conditions. Chapter 6 introduces a snowfall retrieval algorithm for GMI. In chapter 7, the summary and discussions are presented.

The ultimate goal of this study is to enhance the knowledge of snowflake structure and three–dimensional distribution of falling snow. By analyzing the triple-frequency radar signatures from DPR and CPR measurements, we are able to better understand the microphysical properties of different snow particles. The snowfall retrieval algorithm developed for GMI high frequency channels is beneficial for studying the global snow precipitation process by improving the estimation of three–dimensional snow water distribution.

CHAPTER 2

THEORETICAL BASIS FOR SNOWFALL REMOTE SENSING

In this chapter, we will introduce the basic radiative properties of snow clouds in section 2.1. In section 2.2, the physics behind active and passive microwave remote sensing will be discussed.

2.1 Radiative Properties of Snow Clouds

Since this dissertation focuses on snow clouds, the interference by raindrops is negligible. In snow clouds, we mainly consider the absorption and scattering by cloud liquid droplets and snow particles.

In snow clouds, the size of liquid droplets usually ranges from 5 to 50 μm [*Vivekanandan et al.*, 2001]. Spaceborne microwave sensors generally operate in a frequency range from 10 to 200 GHz, corresponding to a wavelength range from 1500 to 30000 μm. We use the nondimensional size parameter as

$$x=\frac{2\pi r}{\lambda}, \tag{2.1}$$

where λ is the wavelength, and r is the spherical particle radius. When the particle size is sufficiently small compared to the wavelength ($x \ll 1$), the scattering by particles is considered as Rayleigh scattering [*Strutt*, 1871]. In this condition, the sufficiently small particle experiences the approximately uniform external electric field. An electric dipole moment is then induced in the particle. The particle is now an electric dipole and generates its own electric filed as the outward radiation. Therefore, the scattering by cloud liquid droplets for a microwave wavelength ($\lambda > 1$ mm) is usually Rayleight scattering [*Stephens*, 1994]. As shown by *Petty* [2006], for Rayleight scattering, the scattering (Q_s) and absorption (Q_a) efficiencies can be expressed as

$$Q_s = \frac{8}{3} x^4 \left| \frac{m^2 - 1}{m^2 + 2} \right|^2 \tag{2.2}$$

and

$$Q_a = 4x \, \mathrm{Im}\{\frac{m^2 - 1}{m^2 + 2}\}, \tag{2.3}$$

where m is the complex refractive index of particle. Im{} represents the imaginary part of {}. It is seen that Q_s is proportional to x^4, while Q_a is proportional to x. Since m for liquid water has a nonzero imaginary part (recall x<<1 for Rayleugh scattering), we can get

$$Q_a \gg Q_s. \tag{2.4}$$

Consequently, the scattering by cloud liquid droplets for microwave wavelengths is negligible relative to the absorption by liquid droplets.

To investigate the radiative effect of snow particles in clouds, we examine the imaginary part of complex refractive index (n_i). It is proportional to the absorption rate of material. Fig. 2.1 shows the imaginary part of the index of refraction of water and ice for a wavelength range from 0.1 to 100 mm. The imaginary part of refractive index of water ($n_{i,\mathrm{water}}$) was calculated by *Segelstein* [1981]. It is implemental to the study of *Hale and Querry* [1973] by extending the wavelength range. The imaginary index of refraction of ice ($n_{i,\mathrm{ice}}$) was provided by *Warren and Brandt* [2008]. It is seen that for $\lambda > 1$ mm, the magnitudes of $n_{i,\mathrm{ice}}$ is about two or three orders smaller than the magnitudes of $n_{i,\mathrm{water}}$. As a result, the absorption by snow particles for microwave wavelengths is negligible. Additionally, the snow particles are usually much larger than liquid cloud droplets with maximum dimensions ranging from 0.1 to 10 mm [*Liu*, 2008b; *Kneifel et al.*, 2011]. The Rayleigh scattering assumption is no longer valid for those large snow particles at some microwave wavelengths. Therefore, the scattering by snow particles for microwave wavelengths is often significant.

2.2 Active and Passive Microwave Remote Sensing

Active microwave sensors, or radars, have been widely used in monitoring global precipitation events [*Kummerow et al.*, 2000; *Liu, 2008a*; *Hou et al.*, 2014]. The radar transmitter emits a series of microwave radiation, then the radar receiver measures the backscattered radiation from the target. The time delay between transmitted and backscattered radiation can be used to determine the distance between radar and target. Hence, radars are able to provide the information of vertical distribution of specific objects. The effective radar reflectivity factor (Z_e) in logarithmic scale (dBZ) at each vertical bin is typically recorded by radars. Z_e can be expressed as

$$Z_e = \frac{\lambda^4}{\pi^5 |K|^2} \int_{D_{min}}^{D_{max}} N(D)\sigma_{bsc}(D)dD, \qquad (2.5)$$

where D_{min} and D_{max} are the lower and upper limits of the snowflake size, N(D) is the particle size distribution, λ is the wavelength, K is a function of the refractive index of water, and $\sigma_{bsc}(D)$ is the backscatter cross section of the snowflake. When the Rayleigh scattering is valid, $\sigma_{bsc}(D)$ is proportional to λ^{-4}. The wavelength dependence of Z_e is canceled out. Under this condition, Z_e varies little with wavelength or frequency.

Fig. 2.2 shows the normalized backscatter cross sections at 13.6 GHz (~22 mm), 35.5 GHz (~8.4 mm) and 94 GHz (~3.2 mm) for rosettes, sectors and dendrites as a function of size parameter. r_e is the effective radius of snow particle. σ_{bsc} is computed by the discrete dipole approximation (DDA) method [*Draine and Flatau*, 1994] and adopted from the database of scattering properties of nonspherical snow particles developed by *Liu* [2008b]. The particle maximum dimension range for selected snow particles is from 0.05 to 10 mm. It is seen that at 13.6 GHz, the scattering is always Rayleigh even for large snow particles ($x \ll 1$). The $\sigma_{bsc}/\pi r_e^2$

increases sharply with size parameter, indicating that larger particles are more effective in scattering radiation. At 35.5 GHz, when the snow particle effective radius is large, the Rayleigh scattering assumption is partly deviated (x~1). At 94 GHz, the scattering is no longer Rayleigh for large snow particles as the size parameter exceeds one, where $\sigma_{bsc}/\pi r_e^2$ increases gradually with size parameter. Consequently, when the snow particle effective radius is large, Z_e varies evidently with frequency, which provides the theoretical basis for triple-frequency radar signature analysis.

Passive microwave sensors typically measure the bulk emission from the Earth's surface and atmosphere system, which is different from radars. The often–used quantity by passive microwave sensors is brightness temperature. In the microwave band, the Rayleigh–Jeans approximation is valid. A simple relationship between brightness temperature and temperature is introduced as

$$T_b = \varepsilon T , \qquad (2.6)$$

where ε is the emissivity of material. Polarization is usually not neglected in the microwave band. In particular, it can affect ocean surface emissivity strongly. Passive microwave sensors generally employ a set of channels at different frequencies and polarizations to detect solid precipitating particles in clouds. The study by *Bennartz and Bauer [2003]* has shown that the scattering signatures from snow particles are only evident at 85 GHz and higher frequencies. In the following, we will carry a radiative transfer modeling experiment to examine the sensitivity of high microwave frequencies to snow scattering signatures.

In this experiment, we will simulate the brightness temperatures from 80 to 200 GHz for clear–sky and cloudy conditions. Cloud liquid water is assumed as a constant of 0.05 g m^{-3} in the lowest 2 km layer. Snow water is assumed as a constant of 0.2 g m^{-3} in the layer between 0.5

and 3.5 km. The sensor's Earth incidence angle is set to zero for nadir viewing. Brightness temperatures are simulated by a radiative transfer model developed by *Liu* [1998]. The radiative transfer modeling results are presented in Fig. 2.3. It is seen that the effect of liquid water is generally to increase the brightness temperature through its emission (green curve). On the other hand, the snow water tends to decrease the brightness temperature, but this effect is not significant at low frequencies (orange curve). When the liquid and snow water coexist in snow clouds, their effects compete with each other. It is found that the effect of snow water only dominates over the effect of liquid water at 140 GHz and higher frequencies (red curve). In the later chapters, high frequency microwave channels are used to retrieve snow–related quantities.

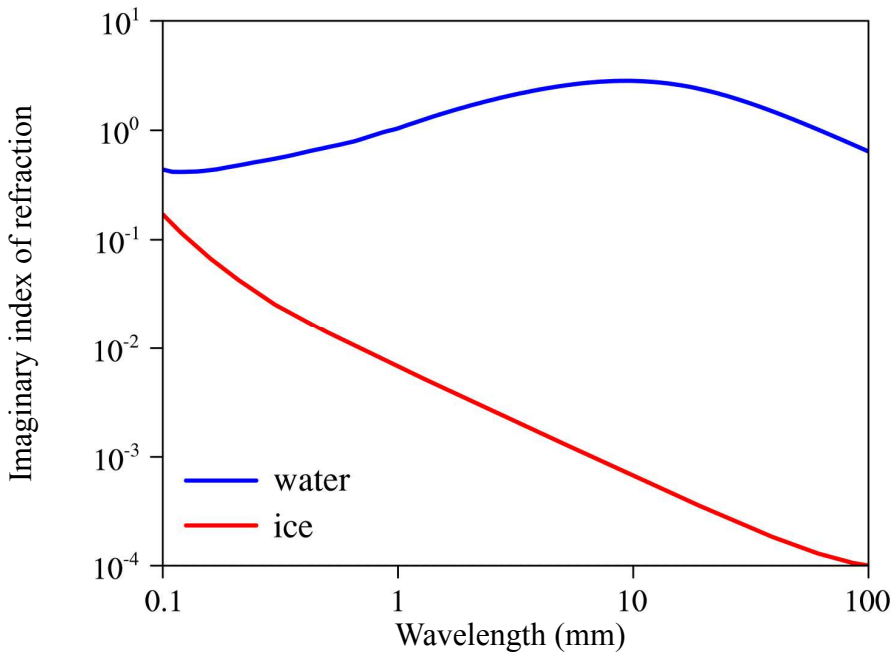

Fig. 2.1. Imaginary part of refractive index of water and ice for a microwave wavelength range from 0.1 to 100 mm.

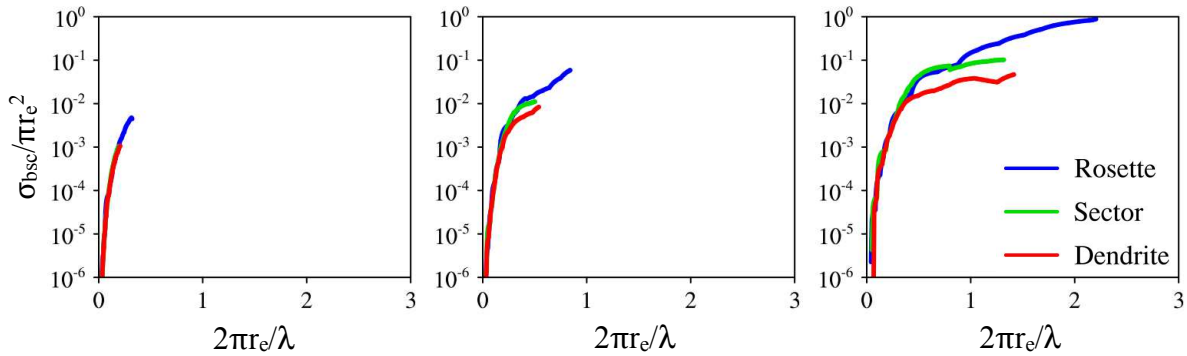

Fig. 2.2. Normalized backscatter cross sections at 13.6 GHz (left panel), 35.5 GHz (middle panel) and 94 GHz (right panel) for selected snow particles.

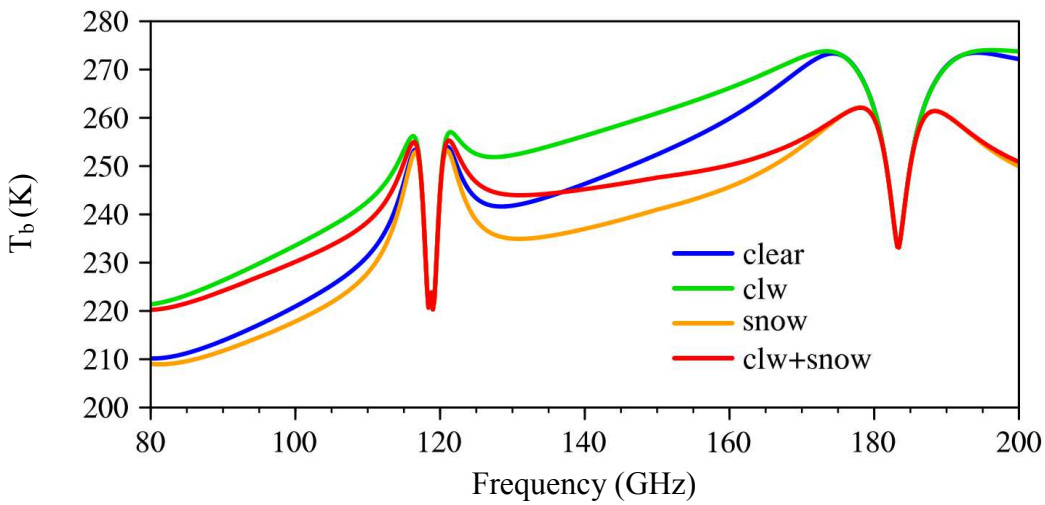

Fig. 2.3. Simulated brightness temperatures from 80 to 200 GHz at nadir for different weather conditions.

CHAPTER 3

INSTRUMENT CHARACTERISTICS AND COINCIDENT DATASET

In this chapter, we will introduce the characteristics of primary satellite instruments for this study in section 3.1. The CloudSat–GPM coincident dataset is then described in section 3.2.

3.1 Satellite Instrument Characteristics

The CPR is the first spaceborne radar that measures the backscattered power from cloud and precipitation systems at 94 GHz (W band). It has been operating since June 2, 2006 after the launch of CloudSat on April 28, 2006. During 2006 to 2017, the CloudSat flies as part of the Afternoon Constellation of satellites (A–Train) with two other NASA satellites, AQUA and CALIPSO, enabling the combination of CPR and other instruments such as Moderate–resolution Imaging Spectro–radiometer (MODIS) onboard AQUA and Cloud–Aerosol Lidar with Orthogonal Polarisation (CALIOP) onboard CALIPSO. The CloudSat has exited the A–Train since February 22, 2018. As a nadir–looking radar, the CPR provides the global information of cloud vertical structures with a vertical resolution of about 485 m. A single radar reflectivity profile contains 150 bins with a vertical bin size of about 240 m. The footprint size of CPR is about 1.4 km across the track and 2.3 km along the track. Its minimum detectable reflectivity factor is about –30 dBZ, allowing the CPR to capture most light frozen precipitations.

The DPR onboard the GPM core satellite is an inheritor from the Precipitation Radar (PR) onboard the TRMM satellite. The DPR consists of Ku (13.6 GHz) and Ka bands (35.5 GHz). Its Ku band channel is similar to that of PR. The adding of Ka band on DPR is a major breakthrough compared to PR. The joint use of Ku and Ka bands can provide the information on raindrop particle size distribution which is thought to be the major uncertainty source in rainfall retrievals. Additionally, the Ka band channel can improve the estimation of freezing level height,

an important parameter in both rainfall and snowfall retrievals. Finally, Ka band has a higher sensitivity to light rain and snow compared with Ku band and therefore expands the observing range of DPR. The DPR is a cross–track instrument. A single scan has 49 footprints for Ku and Ka bands with a footprint size of about 5 km at nadir. The Ka band operates in two modes, match scan (MS) and high sensitivity scan (HS). In the MS mode, the 25 Ka MS band footprints are exactly matched to the Ku normal scan (NS) band footprints (index from 13 to 37). In the HS mode, the 24 Ka HS band footprints are interlaced within the Ka MS band footprints. This mode is mainly employed for light rain and snow. The vertical resolution of Ku NS and Ka MS bands is about 250 m, while the vertical resolution of Ka HS band is about 500 m.

The GPM GMI represents a new generation of conical–scanning microwave imager. It carries channels from 10 to 89 GHz similar to those carried by TRMM TMI with additional four channels at 166 and 183 GHz. The use of these frequencies extends its capability in measuring snow precipitations. Compared with TMI, the spatial resolutions of GMI channels are greatly improved with an antenna diameter of 1.2 m. Its earth incidence angle is 52.8° for channels between 10 and 89 GHz, identical to that of TRMM TMI. For channels at 166 and 183 GHz, the GMI earth incidence angle is slightly different at 49.2°.The swath of GMI is about 900 km on the ground, much broader than that of DPR Ku band (245 km). Therefore, the DPR Ku NS band swath only overlaps the central part of GMI swath. Only GMI channels at 89 GHz and higher frequencies are employed in this study, the detailed specifications of these channels are presented in Table 3.1. At 89 GHz and higher frequencies, the spatial resolutions of GMI channels are about 6 km.

3.2 CloudSat–GPM Coincidence Dataset

The coincident dataset between CloudSat and GPM satellites [*Turk*, 2017] are employed for this study. It mainly combines CPR radar reflectivity, DPR radar reflectivity and GMI brightness temperature. When the ground tracks of GPM and CloudSat satellites are coincident within 15 minutes, a DPR footprint is matched to the nearest CPR footprint. For a single CPR bin, the first DPR bin lying above this CPR bin is searched from the bottom, and this DPR bin is matched to this CPR bin. In the vertical direction, the CPR bin size is about 240 m, while the DPR Ku NS/Ka MS band bin size is about 125 m. Therefore, only every other Ku NS/Ka MS bin is matched to a CPR bin. For DPR Ka HS band, all bins are matched due to its vertical bin size of about 250 m. The procedure in matching CRP and GMI measurements is similar. Since the GMI first nine channels (10 to 89 GHz) are located slightly different from other four channels at 166 and 183 GHz, the footprint of GMI first nine channels are firstly matched to a nearest CPR footprint, then the nearest footprint of other four channels is searched to match this footprint of GMI first nine channels within 5 km. While the CPR footprint size is much smaller than those of DPR and GMI, no pixel averaging or resampling is implemented in this dataset. Fig. 3.1 shows an example of collocation among CPR, DPR and GMI (166 GHz) footprints on June 07, 2014. It is seen that five CPR footprints can generally cross one DPR or GMI footprint. Using the matching method above, some GMI footprints are not overlapped by any CPR footprint. It is necessary to remove those GMI footprints when we use the collocated GMI and CPR measurements.

Fig. 3.2 shows the vertical cross sections of CPR and DPR radar reflectivities as well as the GMI brightness temperatures at high frequencies for a deep convection case. The strong attenuation in CPR radar reflectivity is obvious in this case, since some surface radar reflectivity echoes are almost gone. The DPR Ka band radar reflectivity also experience the moderate

attenuation. The surface clutter effect is evident for DPR Ku band, especially on the two sides of swath. The low brightness temperatures at 89 GHz and higher frequencies generally correspond to the most intense convections around 25°S. In the following chapters, we will further refine this coincident dataset by considering the respective characteristics of CloudSat and GPM instruments.

Table 3.1. Specifications of GMI channels at 89 GHz and higher frequencies.

Central freq (GHz)	Polarization	Beam width (deg)	Footprint (km)	NEDT (K)
89.00	V	0.390	7.2×4.4	0.57
89.00	H	0.390	7.2×4.4	0.57
166.00	V	0.396	6.3×4.1	1.50
166.00	H	0.396	6.3×4.1	1.50
183.31±3	V	0.361	5.8×3.8	1.50
183.31±7	V	0.361	5.8×3.8	1.50

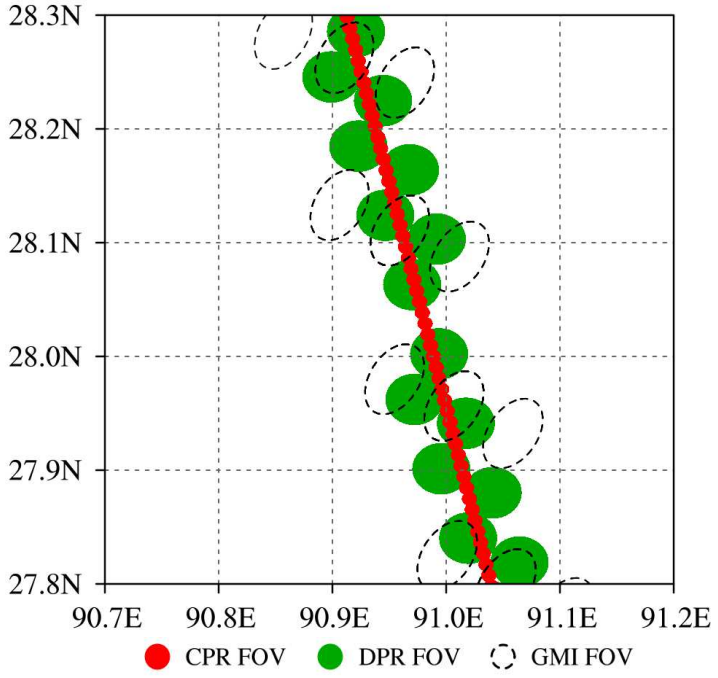

Fig. 3.1. An example of collocation among CPR, DPR and GMI (166 GHz) footprints on June 07, 2014.

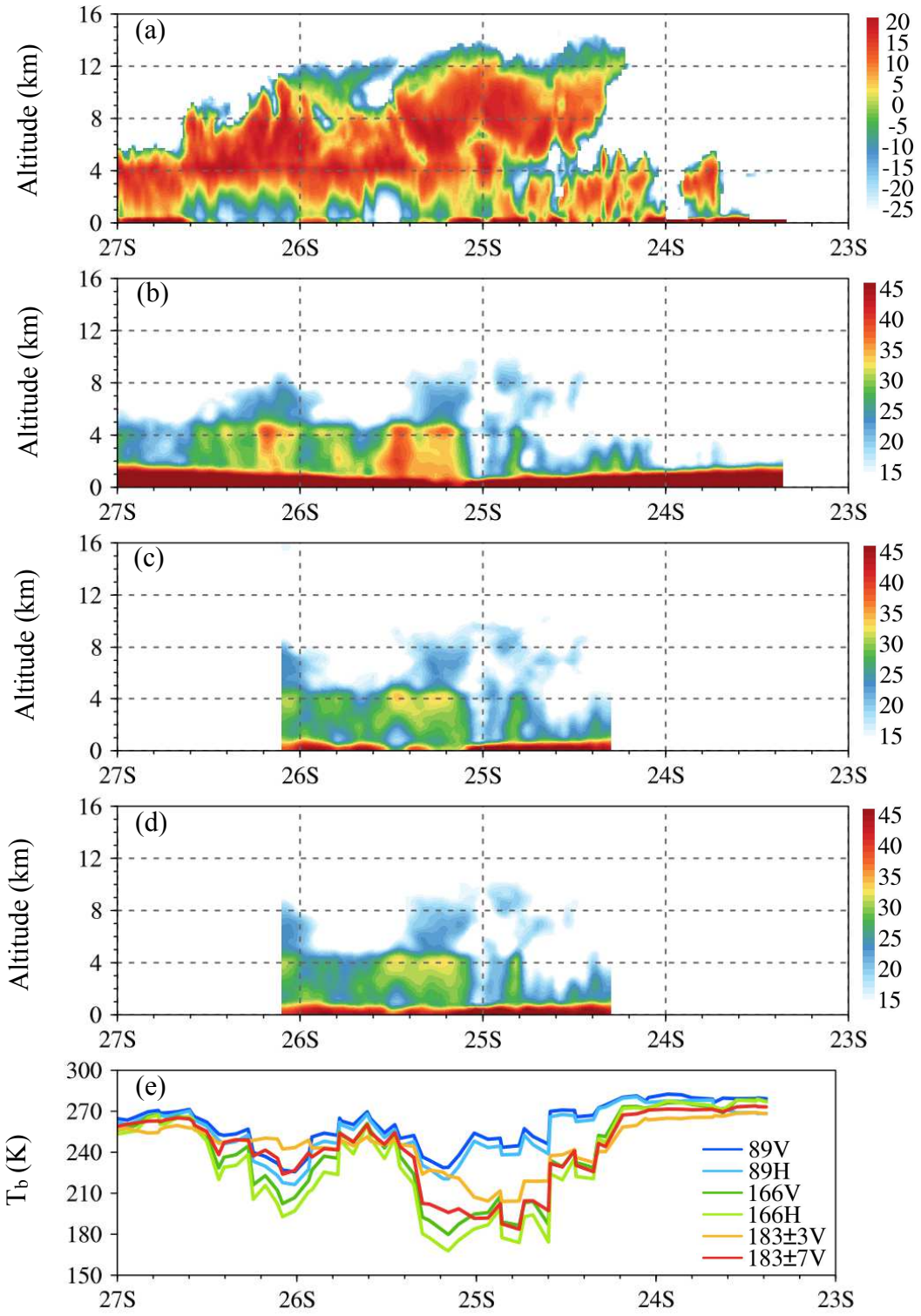

Fig. 3.2. Vertical cross sections of (a) CPR, (b) DPR Ku NS, (c) Ka MS and (d) Ka HS radar reflectivities (unit: dB) as well as (e) GMI brightness temperatures at 89 GHz and higher frequencies for a single case on March 09, 2014.

CHAPTER 4

TRIPLE FREQUENCY RADAR SIGNATURE ANALYSIS

This chapter is organized as follows. Section 4.1 provides the brief introduction to triple-frequency radar signatures. Section 4.2 describes the data sources and methods. Section 4.3 discusses the observed difference in triple-frequency radar signatures between stratiform and convective clouds. Section 4.4 provides the conclusions for this chapter.

4.1 Introduction

Snow is a dominant form of precipitation at high latitudes. Since the scattering properties of snowflakes are sensitive to their structures in the non-Rayleigh regime [*Kulie et al.*, 2001; *Liu*, 2004], any progress in inferring snowflake structures can potentially reduce the uncertainty in snowfall retrievals. A modeling study by *Kneifel et al.* [2011] explored the joint use of two dual-frequency ratios (DFRs) at Ku, Ka and W bands. They suggested that different snowflake habits possess distinctive triple-frequency signatures, which allows a possible identification of snowflake habits. Subsequent investigations by *Leinonen et al.* [2012] and *Kulie et al.* [2013] employed radar measurements to verify this approach. They both found that most observed triple-frequency signatures can be explained by aggregate particle models. *Stein et al.* [2014] also utilized triple-frequency radar measurements to retrieve the fractal dimension of snow aggregates in stratiform ice clouds. The results indicated that the fractal snowflake model rather than spherical and spheroidal models describe the observed snow aggregates better. The modeling experiments by *Leinonen and Moisseev* [2015], *Leinonen and Szyrmer* [2015] as well as *Tyynelä and Chandrasekar* [2014] examined the triple-frequency behaviors of unrimed and rimed aggregates. The triple-frequency signatures of rimed aggregates approach those for spheroidal snowflakes but still deviate from spheroids. A recent study using triple-frequency

Doppler radar spectral [*Kneifel et al.*, 2016] also demonstrated that the scattering properties of spheroids do not fit the observed rimed aggregates. Although those studies implied the possible utilities of triple-frequency signatures, there is still a need in using this approach to understand cloud microphysical properties and assist developing snowfall retrieval algorithms.

In this chapter, a combined dataset of CloudSat CPR [*Stephens et al.*, 2002] and GPM DPR [*Iguchi et al.*, 2002] is utilized to provide observed triple-frequency signatures over ocean. As shown in Section 4.3, a distinct difference is found in the observed triple-frequency signatures between snow particles in stratiform and convective clouds. The main goal is to find the possible cause of the observed difference so that this information could be used in future cloud physics and remote sensing studies.

4.2 Data Sources and Methods

4.2.1 Satellite and Analysis Data

The primary data used in this study is the coincident dataset, 2B–CSATGPM, available from NASA data center at: https://storm.pps.eosdis.nasa.gov/storm/, which combines GPM DPR and CloudSat CPR radar reflectivities, as well as GMI brightness temperatures and several geophysical variables from European Centre for Medium-range Weather Forecasts (ECMWF) analysis. The CPR is a nadir-looking radar that measures the backscattered power from cloud systems at 94 GHz (W band). The DPR has 13.6 GHz (Ku band) and 35.5 GHz (Ka band) channels. In this collocated dataset, each CPR profile is matched with a nearest DPR profile when their satellite tracks coincide within 15 minutes. The data duration for this study is from March 2014 to April 2016. Since the focus of this study is on triple-frequency signatures of snowflakes over ocean, we will analyze radar bins that are above freezing level heights with CPR surface type classified as ocean. In deep convections, strong updrafts may carry raindrops above

freezing levels. To minimize this possible contamination, we only select cases that have freezing level heights lower than 3 km. This criterion helps remove those deep convective cases, i.e., deep convective clouds in the tropics and those in mid latitudes during summer where the freezing level height is about 5 km and strong updrafts usually exist. For the remaining cases at mid and high latitudes, deep convections (or strong updrafts) are less likely to form, so it is expected that raindrops are less likely to be lifted to high altitudes above freezing level. The use of 3 km freezing level height to select cases is based on the balance of limiting raindrop contamination and preserving a reasonable sample size. Using a stricter criterion (e.g., selecting data only from profiles with near-surface air temperature lower than freezing point) will largely reduce the sample number, which leads to unstable statistics. To better match CPR and DPR data, we only retain those radar bins within DPR scan angle range of ±2.8°. Additionally, radar bins in the lowest 1 km are discarded to avoid surface contamination. It should be cautioned that the coincident CPR and DPR data cannot be matched exactly to make the measurements at three frequencies from the same volume, because CPR and DPR are onboard different satellites and have different spatial resolutions. The vertical bin size of CPR is about 240 m, and DPR Ku and Ka bands are reported at a vertical bin size of about 125 m. For a single CPR bin, the matched DPR Ku/Ka bin is the nearest one that lies above this CPR bin, so approximately every other DPR Ku/Ka bin is matched to a CPR bin. It is worth mentioning that there are still some mismatching errors between CPR and DPR due to their different vertical resolutions and platforms. However, this matching method might be the best one that can be used now. The footprint size of CPR is about 1.4 km across the track and 2.3 km along the track. The footprint of DPR has a size of about 5.2 km at nadir. The horizontal resolutions between CPR and DPR are quite different. To account for the impact of this spatial mismatch, all CPR profiles that are

originally matched with the same DPR profile are averaged to obtain a mean CPR profile to match the corresponding DPR profile. To evaluate the impact of temporal mismatch, the distributions of observed triple-frequency signatures are calculated separately from data with time differences shorter than 7.5 minutes and longer than 7.5 minutes. The results are presented in the next section and do not show a systematic difference.

4.2.2 Attenuation Correction on Radar Reflectivity

For snowfall conditions, attenuation due to snow itself is negligible for Ku and Ka bands but can be significant for W band. As shown by *Matrosov* [2007], the total attenuation at W band can exceed 1 dB for thick snow layers, while the attenuation at Ka band is about one order magnitude smaller than that at W band. A first-order correction method is adopted from *Kulie et al.* [2013] to account for the attenuation at W band caused by snow. An averaged linear relationship using both of dendrite [*Liu*, 2004] and oblate rosette aggregate [*Honeyager et al.*, 2016] is developed between W band specific attenuation (dB km^{-1}) and Ku band radar reflectivity (mm^6 m^{-3}). An exponential particle size distribution is employed:

$$N(D)=N_0\exp(-\Lambda D) \tag{4.1}$$

where N_0 is the intercept parameter, Λ is the slope parameter, and D is the maximum dimension of snowflake. The use of the exponential form of particle size distribution is based on previous experimental and modeling studies such as *Braham* [1990] and *Senn and Barthazy* [2014]. It has been used in other triple-frequency radar signature studies. Forty-nine (49) pairs of N_0 and Λ are taken from *Braham* [1990] to calculate W band specific attenuation and Ku band radar reflectivity. Cloud liquid water is another important factor that contributes to the attenuation. Assuming a liquid water content of 0.5 g m^{-3}, the specific attenuation at Ku band is smaller than 0.2 dB km^{-1}, while the specific attenuations at Ka and W bands can reach about 1 dB km^{-1} and 4

dB km^{-1}, respectively [*Kneifel et al.*, 2011]. Cloud liquid water profiles are obtained from GPM combined radar-radiometer product [*Olson and Masunaga*, 2011]. This product applied a Bayesian method and *a priori* database that connects environmental parameters and simulated GMI brightness temperatures to retrieve cloud liquid water profiles. Currently, the *a priori* database only supports estimates of cloud liquid water profiles over ocean. Therefore, only triple frequency data over ocean is selected in this analysis. This product may contain some retrieval errors, but it is still a good data source for correcting cloud liquid water attenuation. The specific attenuation due to cloud liquid water at Ka and W bands can be estimated using cloud liquid water content, frequency and complex dielectric permittivity [*Salonen and Uppala*, 1991]. The complex dielectric permittivity as a function of frequency and temperature is calculated by a double-Debye model [*Manabe et al.*, 1987]. Additionally, the attenuation due to atmospheric gases including water vapor at W band is corrected based on values obtained directly from CloudSat CPR product 2B–GEOPROF.

4.2.3 Data Selection

A minimum detection threshold of 13 dB is used for DPR Ku band reflectivity according to the evaluation results of *Toyoshima et al.* [2015], which approximately corresponds to 11 dB for Ka MS and 2 dB for W band reflectivities in their scatterplots versus Ku band reflectivity. In the following analysis, we only use data with reflectivities greater than 13, 11 and 2 dB for Ku, Ka and W bands, respectively.

The CloudSat CPR product 2B-CLDCLASS [*Sassen and Wang*, 2008] is utilized to determine cloud type, i.e., stratiform versus convective. A case is considered as stratiform when at least 94% of qualified radar bins were classified as nimbostratus. Similarly, in convective cases, at least 94% of qualified radar bins were classified as cumulus or cumulonimbus. We

require that a nimbostratus or cumulonimbus case has to contain at least 20 qualified radar bins to avoid random error, while no restriction is made for cumulus cases due to their smaller dimensions. All selected cases are located 35° latitude poleward. A total of 65 stratiform cases (4164 qualified radar bins) and 23 convective cases (907 qualified radar bins) are finally selected. About 40 % of qualified radar bins in convective cases have freezing levels below 1 km and are likely associated with convective snow showers.

4.3 Discussion on Triple-frequency Radar Signatures

4.3.1 Observed Difference between Stratiform and Convective Cases

Fig. 4.1 and 4.2 show the normalized occurrence frequencies of observed triple-frequency signatures (shading) for stratiform and convective cases in 1 dB × 1 dB boxes for data with time differences between CPR and DPR smaller than 7.5 minutes (top panels) and larger than 7.5 minutes (bottom panels). The DFR is defined as the logarithmic difference of equivalent radar reflectivity factors at two frequencies. We use DFR X/Y to denote the DFR between X and Y bands. Some negative DFR values mainly for DFR Ku/Ka are found associated with small DPR Ku radar reflectivities. Since large negative DFR values are physically meaningless and primarily caused by observation uncertainties, DFR values smaller than –0.5 dBZ have been excluded in the data selection procedure. It is worth noting that even large snow particles at Ku band are usually Rayleigh scatterers, which makes Ku band a good Rayleigh reference. DFR Ku/Ka thus is an indicator of large particles, because large particles would become non-Rayleigh scatterers at Ka band. At W band, the deviation from Rayleigh scattering depends on both particle size and density. A small but dense snow particle can become a non-Rayleigh scatterer at W band. Hence, DFR Ku/W or DFR Ka/W is sensitive to particle size and density. Two sets of

DFRs are used as x-axis. In addition to use DFR Ka/W as x-axis (Fig. 4.1) as done in previous triple-frequency studies, DFR Ku/W is also employed (Fig. 4.2).

When using DFR Ka/W as x-axis, it is found that data points in stratiform cases are confined by 14 dB along x-axis but can extend to 9.5 dB along y-axis, while data points in convective cases can exceed 15 dB along x-axis but can only reach about 8 dB along y-axis. Similarly, when using DFR Ku/W as x-axis, data points in stratiform cases rarely exceed 16 dB along x-axis, while data points in convective cases can reach about 19 dB along x-axis. In general, the observed triple-frequency signatures of stratiform cases are distributed more in the DFR Ku/Ka direction, while those of convective cases are distributed more in the DFR Ku/W or Ka/W directions. The distributions of triple-frequency signatures in stratiform cases are mainly monomodal, while the ones in convective cases show certain bimodality. This bimodal feature of convective cases seems to be clearer using DFR Ka/W, because the effects of particle size and density on triple-frequency signatures separate themselves more in the DFR Ka/W–Ku/Ka diagram. This general feature is the same for both data groups with DPR-CPR observation time difference 0–7.5 minutes and 7.5–15 minutes. In other words, within the maximum 15-minute time difference limit, the data selection by restricting them to a shorter time difference does not seem to alter our general conclusions. To preserve a large enough sample size, in the following, all data within 15-minute time difference are analyzed together without further dividing them into multiple groups.

The occurrence frequency distributions indicate a distinct difference between stratiform and convective cases. Since DFR values are directly related to scattering properties of concerned snowflakes, this distinction between stratiform and convective cases is expected to convey information about snow particle structures in their respective environments.

4.3.2 Modeled Triple-frequency Signatures

In order to understand the observed difference between stratiform and convective cases, calculations of the backscattering properties for several snow particle models are conducted. Specifically, 3–, 4–, 5– and 6–bullet rosettes (R3–R6), sectors (S) and dendrites (D) [*Liu*, 2004] are selected to represent pristine crystals. Rounded rosette aggregates (Ar) [*Nowell et al.*, 2013] and oblate rosette aggregates (Ao) [*Honeyager et al.*, 2016] are used to represent snow aggregates. One type of unrimed dendrite aggregates (Lu), five types of rimed dendrite aggregates from model A and five types of rimed dendrite aggregates from model B of *Leinonen and Szyrmer* [2015] are also employed to represent snow aggregates. In the Leinonen and Szyrmer models, a parameter, called effective liquid water path (ELWP), controls the riming extent. Lightly rimed aggregates (i.e., ELWP = 0.1, 0.2 and 0.5 kg m^{-2}) still maintain dendrite features well, while heavily rimed aggregates (i.e., ELWP = 1.0 and 2.0 kg m^{-2}) are almost shapeless. We denote the former "La" and the latter "Lb" in the following discussions. Finally, three oblate spheroids with volume fractions of 0.1, 0.2 and 0.3 (S1–S3) [*Honeyager et al.*, 2016] are also investigated using the T-matrix method [*Barber and Yeh*, 1975]. The aspect ratio of these spheroids is fixed at 0.6 based on observations from *Matrosov* [2015].

Using size distribution (4.1), modeled triple-frequency signatures for large particles (Λ= 1 cm^{-1}) and small particles (Λ = 7 cm^{-1}) are presented in Fig. 4.3. DFR values are independent of N_0. The maximum particle sizes for rosettes, sectors and dendrites [1] are truncated at 5 mm [*Kulie et al.*, 2013; *Kneifel et al.*, 2015]. Rounded rosette aggregates [*Nowell et al.*, 2013] have the maximum particle sizes up to 12 mm, oblate rosette aggregates [*Honeyager et al.*, 2016] have the maximum particle sizes up to 11 mm, and dendrite aggregates [*Leinonen*

and Szyrmer, 2015] have the maximum particle sizes up to 22 mm. DFR Ku/Ka values (y-axis) in top and bottom figures are the same.

For small particles (blue), DFR Ku/Ka values for rosettes, sectors and dendrites are similarly small at about 1–3 dB, while aggregates have DFR Ku/Ka values in a range of 3–8 dB. For large particles (red), rosettes, sectors and dendrites still produce small DFR Ku/Ka values of about 1–3 dB. Rosette aggregates produce DFR Ku/Ka values around 6–7 dB, and dendrite aggregates have DFR Ku/Ka values of about 10–13 dB. When using DFR Ka/W for small particles (top panel, blue), rosettes, sectors and dendrites have values at about 2–6 dB. Unrimed dendrite aggregates and lightly rimed dendrite aggregates have larger values at about 6–9 dB. The largest values occur for rosette aggregates and heavily rimed dendrite aggregates at about 11–14 dB. Similarly, for DFR Ku/W values of small particles (bottom panel, red), rosettes, sectors and dendrites have the smallest values (4–8 dB), while rosette aggregates and heavily rimed dendrite aggregates have the largest values (15–20 dB). Unrimed dendrite aggregates and lightly rimed dendrite aggregates have moderate values about 9–13 dB. When particle size increases (i.e., from blue to red), the increases in DFR Ka/W values of nonspherical snowflakes are small, for some rosettes and heavily rimed dendrite aggregates, there are even decreased values because large particles become non-Rayleigh at both Ka and W bands. In contrast, DFR Ku/W values of nonspherical snowflakes increase significantly. Spheroids are distinctive from other nonspherical snowflakes with particularly large DFR Ku/Ka values. For large particles, although not shown in this figure, their DFR Ku/Ka values can reach about 15–17 dB.

A novel study on relations between snowflake microphysical properties and triple-frequency signatures has been done by *Kneifel et al.* [2015], in which triple-frequency observations were combined with ground-based in situ snow particles measurements. Through

three case studies, it was found that when large aggregates (> 5 mm) are present in the in situ measurements, there is a bending (in the DFR Ka/W–Ku/Ka diagram) of observed triple-frequency signatures away from the averaged spheroidal line, and rimed particles are connected to horizontal distributions of observed triple-frequency signatures. To be specific, large DFR Ku/Ka values can be assigned to large aggregates, and a combination of small DFR Ku/Ka and large DFR Ka/W values is connected to dense rimed particles. In the region with small DFR values at both frequency combinations, it is difficult to infer snowflake structures due to their similar DFR values. From this present work, it is seen that higher DFR Ku/Ka values are associated with larger particle sizes. Dendrite aggregates have the largest DFR Ku/Ka values, because their maximum particle sizes are the largest. On the other hand, even increasing particle sizes, DFR Ku/W or Ka/W values do not show significant variations. It seems that large DFR Ku/W or Ka/W values are connected to those heavily aggregated (Ar and Ao) or rimed particles (Lb). For those simple crystals with the smallest maximum particle sizes (R3–R6, S and D), their DFR values are similarly small at all frequency combinations. Generally, the finding from this modeling experiment is consistent with the one from *Kneifel et al.* [2015]. This work also implies that if unrimed aggregates (Ar and Ao) are dense enough [*Nowell et al.*, 2013; *Honeyager et al.*, 2016], they can produce similar DFR Ku/W or Ka/W values to those heavily rimed particles (Lb). Based on this finding and those results from *Kneifel et al.* [2015], three types (or modes) of nonspherical snow particles are classified. Type A contains a wide range of small particles (i.e., R3–R6, S and D) with similar triple-frequency signatures. Type B contains unrimed or lightly rimed particles (Lu and La). Type C contains heavily aggregated and/or rimed particles (Ar, Ao and Lb) that represent very dense snowflakes. This grouping of different snowflake types, while somewhat arbitrary, reflect their common characteristics in a simple way.

Fig. 4.4 shows modeled triple-frequency signatures and normalized occurrence frequencies of observed triple-frequency signatures. The average of modeled triple-frequency signatures from R3–R6, S and D is used to represent type A particles. Similarly, the average of triple-frequency signatures from Lu and La is used to represent type B particles, and type C particles are represented by the average of triple-frequency signatures from Ar, Ao and Lb except two rimed dendrite aggregates with ELWP = 2.0 kg m^{-2}. The minimum particle sizes for these two aggregates are 2.9 mm, which makes their modeled lines separated far from those for other particle types in a triple-frequency space when Λ is very small (see Fig. 3.5 in *Leinonen and Szyrmer* [2015]). The maximum particles sizes for all rosettes, sectors and dendrites are still truncated at 5 mm. Λ in the particle size distribution of Eq. (1) is varied from 1 to 45 cm^{-1} to produce black curves in Fig. 4.4. This range of Λ is similar to that used in *Leinonen and Moisseev* [2015] (1 to 50 cm^{-1}). Commonly, type A particles can only explain a small portion of observed triple-frequency signatures where their DFR values are relatively small. Type B particles seem to be more appropriate for those observed signatures with large DFR Ku/Ka values in stratiform cases. Type C particles explain those observed signatures with large DFR Ka/W or Ku/W values and small DFR Ku/Ka values in convective cases better. When using DFR Ka/W as x-axis (top panels in Fig. 4.4), a typical hook feature of observed triple-frequency signatures is found for stratiform cases, and observed triple-frequency signatures follow horizontal curves for convective cases. It is suggested that more snowflakes in stratiform cases have large particle sizes, and convective cases contain more dense snow particles that are heavily aggregated and/or rimed. In order to further explore the relation between observed triple-frequency signatures and snowflake structures, a snowflake classification is conducted as follows. For a bin of radar observation, the particle type it represents is determined by the nearest

modeled line in Fig. 4.4. The statistics of classified snowflake types for stratiform and convective cases are shown in Fig. 4.5. It is seen that set 1 (using DFR Ka/W as x-axis) and set 2 (using DFR Ku/W as x-axis) produce similar results. For stratiform cases, type B particles are more prevalent than other two particle types. Type A particles take up the smallest portion. For convective cases, type A and C particles are more abundant than in stratiform cases. When using set 2, type C particles seem to have the largest proportion. Since this grouping of modeled snowflake types is somewhat arbitrary, instead of claiming which snowflake type is the best fit for stratiform or convective cases, it is more important to notice that the percentage of type B particles in stratiform cases is greater than that in convective cases, while type C particles take up a larger percentage in convective cases than in stratiform cases. It is plausible that a significant portion of snow particles are unrimed particles or aggregates with large particle sizes (type B) in stratiform cases, while heavily aggregated and/or rimed particles (type C) with relatively small particle sizes are prevalent in convective cases. It is worth mentioning that an increasing percentage of very small particles (type A) in convective cases also contribute to the horizontal distributions of observed triple-frequency signatures, as they are usually associated with small DFR Ku/Ka values. Hence, the difference in triple-frequency signatures between stratiform and convective cases can be attributed to their different snowflake modes. As mentioned in *Kneifel et al.* [2015], when the DFR values for both frequency combinations are very small, it is difficult to distinguish detailed structures of snow particles from their similarly weak triple-frequency signatures. It is admitted that type A particles in stratiform cases might differ from those in convective cases, as type A include various small crystals or aggregates.

4.3.3 Statistics of Particle Type versus Temperature

Upon knowing that the triple-frequency signatures carry the information of snowflake structures, an interesting question may arise: how are the three snowflake types defined above distributed in natural clouds? In the following, we investigate their distribution with temperature using all selected cases.

The relative frequency distributions of snowflake types (as determined by method described in previous section) over temperature range of 255 to 273 K for stratiform and convective cases are shown in Fig. 4.6. When using set 1 (DFR Ku/Ka and Ka/W), for stratiform cases, the relative frequencies of type A particles are less than 20 %. The relative frequencies of type B particles generally increase with temperature and become the highest above 265 K. The relative frequencies of type C particles tend to decrease with temperature, but remain above 30 % over a broad temperature range from 255 to 270 K. For convective cases, the relative frequencies of type A particles can exceed 30 % below 259 K. Type B particles take up a larger percentage over warmer temperatures. The relative frequencies of type C particles can dominate a wide temperature range and remain above 40 % below 265 K. Similar distributions of relative frequencies are found using set 2 (DFR Ku/Ka and Ku/w) with some differences as described below. In stratiform cases, the relative frequencies of type A particles are only about 10 % near 273 K. The relative frequencies of type B particles become the highest above a colder temperature 258 K. Similarly, in convective cases, less type A particles are found near 273 K, while the relative frequencies of type B particles seem to become higher.

In summary, in stratiform clouds, type A particles are relatively rare, type B particles are dominant at warm temperatures, and type C particles take up a large portion at cold temperatures. In convective clouds, type A particles are primary at very cold temperatures, type B particles are popular at warm temperatures, and type C particles dominate over a wide

temperature range. The results suggest that stratiform cases contain a lot of unrimed snow particles with large particle sizes (type B), while a large percentage of small dense snowflakes that are heavily aggregated and/or rimed (type C) exist in convective cases.

4.4 Conclusions for Triple-frequency Radar Signature Analysis

A clear difference of observed triple-frequency signatures between snowflakes in stratiform and convective cases over ocean is discovered from combined CloudSat CPR and GPM DPR observations. Modeling experiment of various snow particles and previous relevant studies indicates that this difference is likely caused by the difference in prevailing particle modes between stratiform and convective snow clouds. A simple classification of snowflake types is developed, based on which the fraction of three defined particle types and their dependence on temperatures are investigated. The statistics indicate a large fraction of large unrimed snow particles over warm temperatures in stratiform clouds and abundant heavily aggregated and/or rimed particles with relatively small particle sizes in convective clouds.

Several useful implications can be gained from this work. First, for modeling scattering properties of snowflakes in different types of clouds, our study suggests that large unrimed snow particles might be more appropriate for stratiform clouds, while small dense particles that are heavily aggregated and/or rimed are probably better for convective clouds. Additionally, both of these two particles modes are popular in snow clouds over ocean. However, since the distinction among various snow crystals or aggregates is not obvious from their DFR values when snow particles are small, a further study that utilizes higher radar frequencies is needed [*Battaglia et al.*, 2014]. Second, it seems that DFR Ku/Ka is highly related to snow particle sizes, and DFR Ku/W or Ka/W is closely associated with snowflake density or internal mass in a triple-frequency space. Finally, the useful particle mode information shown in

this study suggests that spaceborne triple-frequency radar observations are beneficial in future snowfall retrievals. It is also noted that the results of this study are still partly subject to the impact of spatial and temporal mismatches between CPR and DPR even after several data processing steps are performed, which further emphasizes the necessity of spaceborne radar that makes observations at three different frequencies from the same satellite platform.

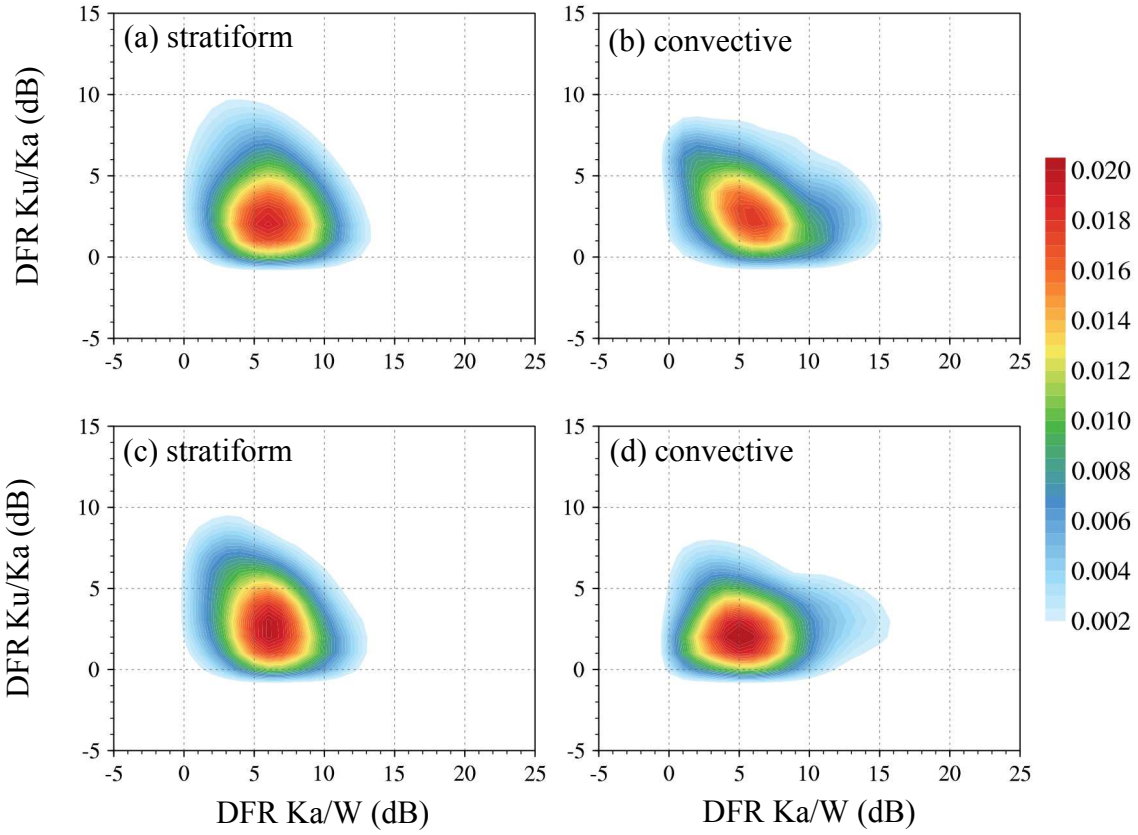

Fig. 4.1. Normalized occurrence frequencies of observed triple-frequency signatures (shading) for stratiform and convective cases in 1 dB × 1 dB boxes with time differences between CPR and DPR smaller than 7.5 minutes (top panels) and larger than 7.5 minutes (bottom panels).

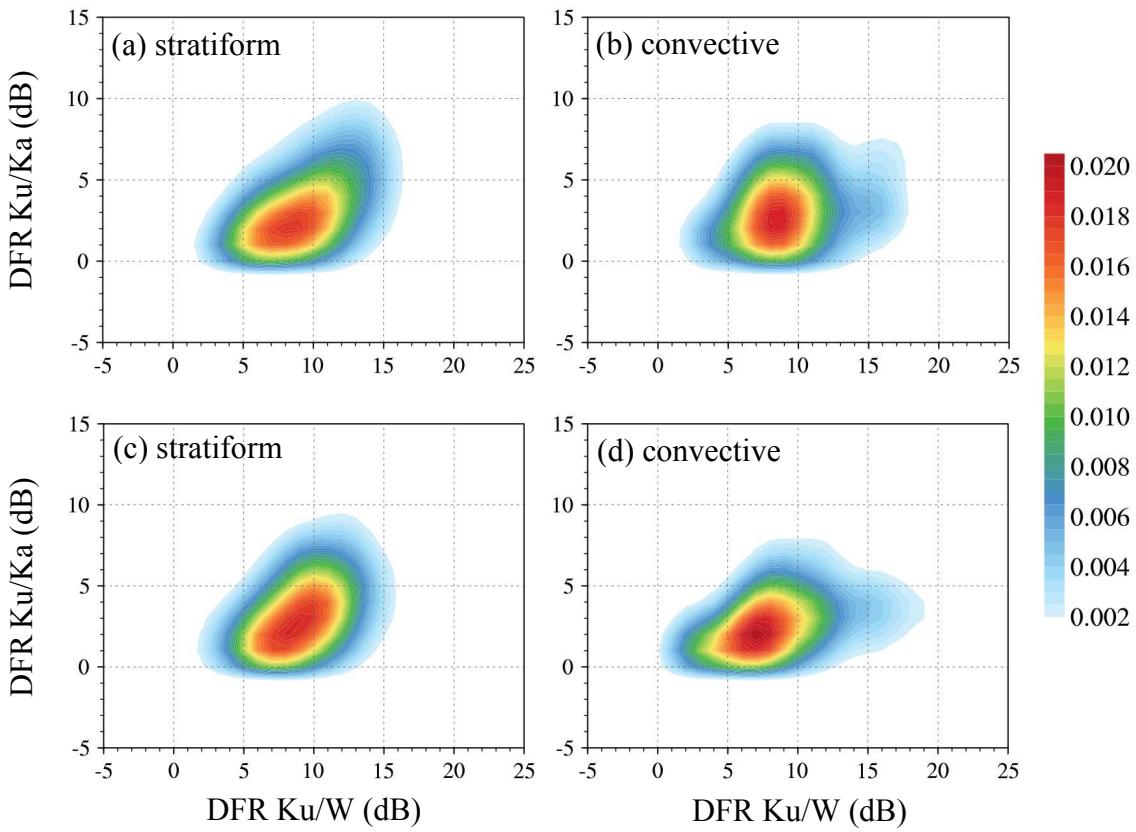

Fig. 4.2. Same as Fig. 4.1 except that x-axis is DFR Ku/W.

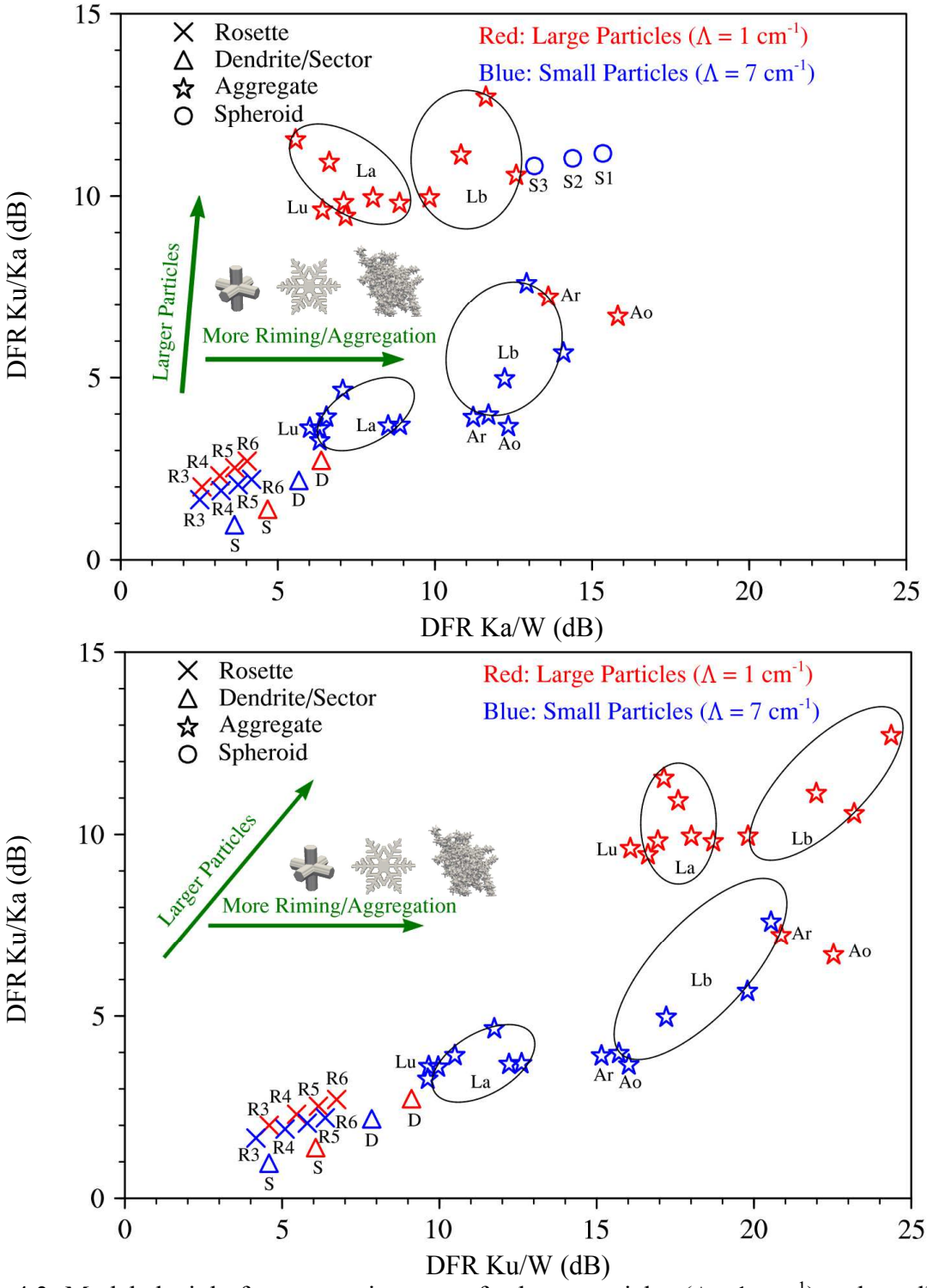

Fig. 4.3. Modeled triple-frequency signatures for large particles (Λ= 1 cm^{-1}) and small particles (Λ = 7 cm^{-1}).

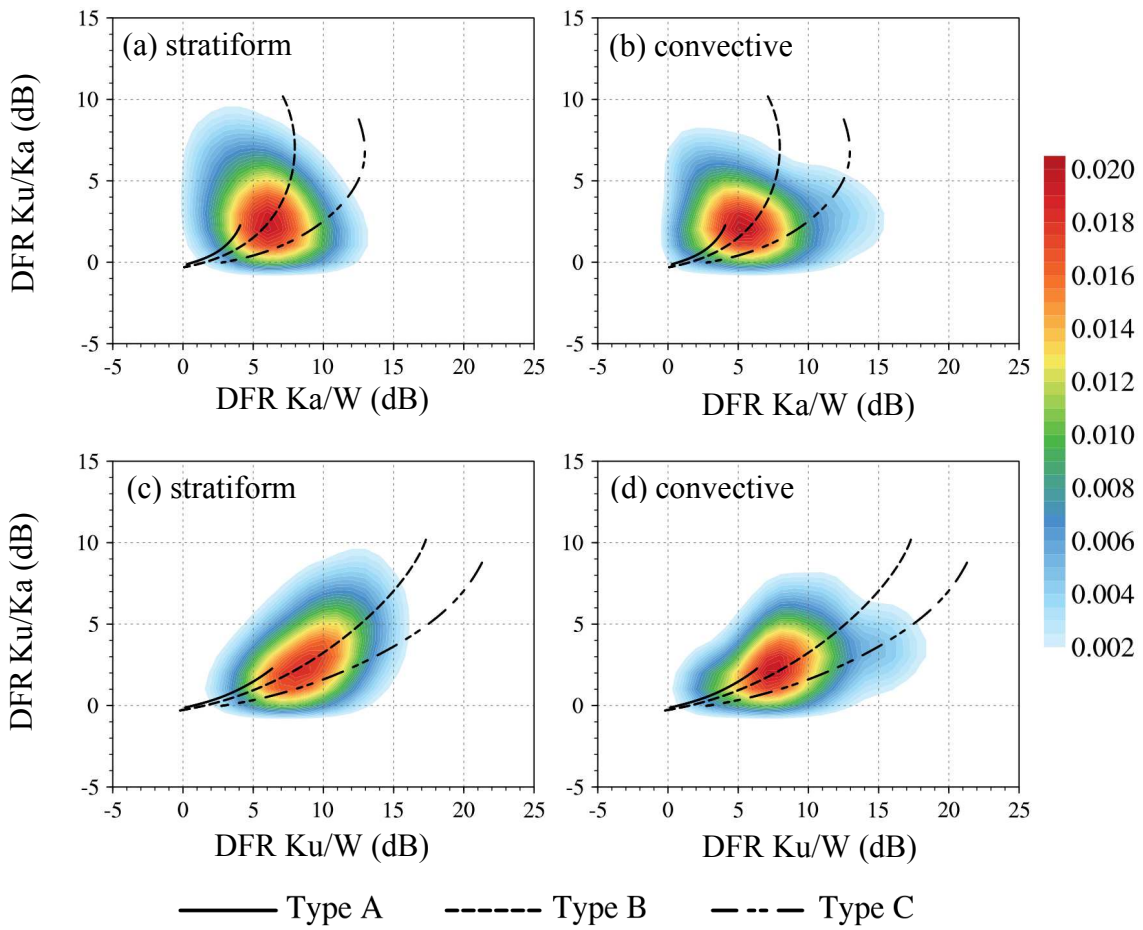

Fig. 4.4. Model triple-frequency signatures (black lines) and normalized occurrence frequencies of observed triple-frequency signatures (shading) in 1 dB × 1 dB boxes for stratiform and convective cases.

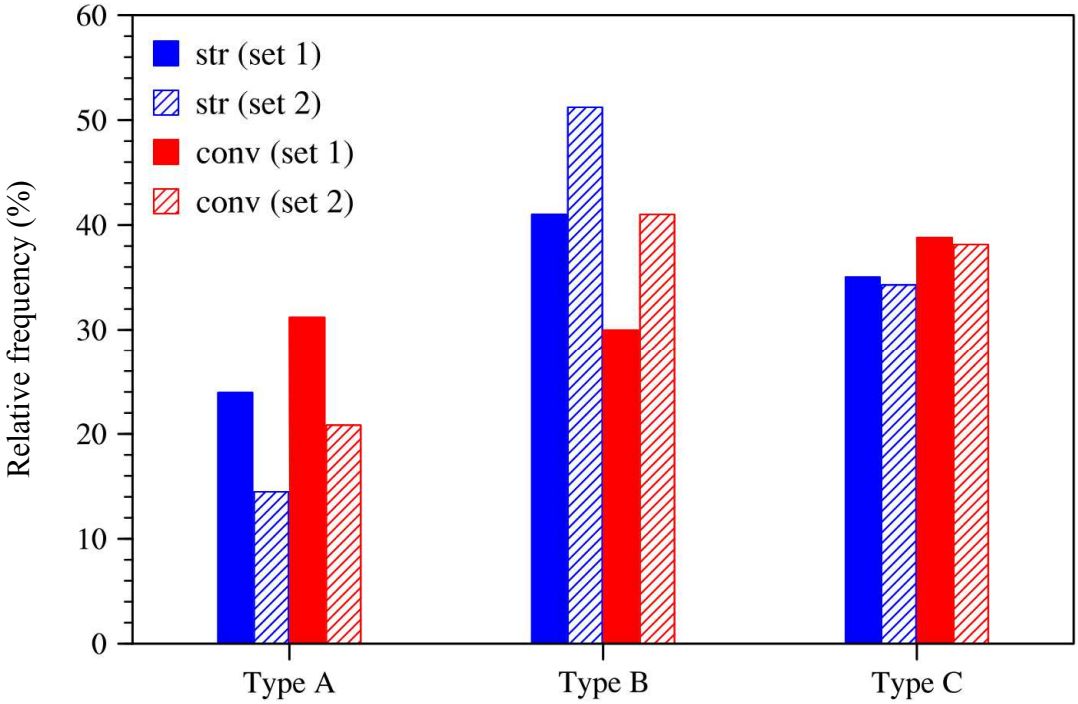

Fig. 4.5. Relative frequencies of classified snowflake types for stratiform and convective cases using set 1 (DFR Ku/Ka and Ka/W) and set 2(DFR Ku/Ka and Ku/W).

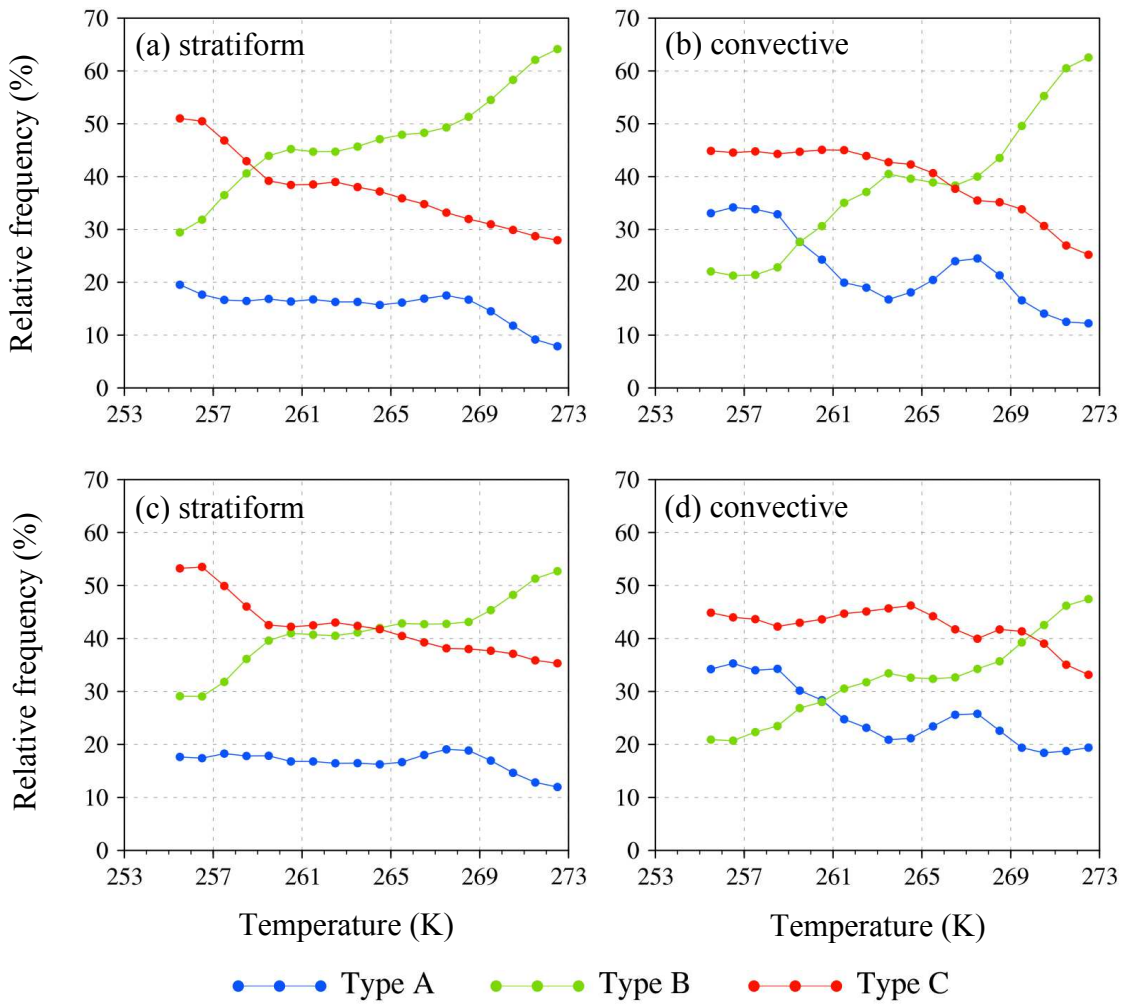

Fig. 4.6. Relative frequency distributions of classified snowflake types over temperature intervals for stratiform and convective cases using set 1 (top panels) and set 2 (bottom panels).

CHAPTER 5

ASSESSMENT OF GPM HIGH FREQUENCY MICROWAVE MEASUREMENTS

Before applying GMI high frequency measurements to snowfall predictions and retrievals, it is important to assess them with model simulations. This chapter is organized as follows. Section 5.1 introduces the background of bias characterization of microwave high frequency measurements. Section 5.2 provides the data sources and experiment setups. Section 5.3 presents the bias characteristics of the observed minus simulated brightness temperatures. Section 5.4 analyzes the remaining biases under snowfall conditions. Section 5.5 gives the conclusion for this chapter.

5.1. Introduction

Passive microwave measurements play an important role in retrieving atmospheric parameters and predicting the evolution of weather systems. The use of passive microwave observations in retrieval algorithms and data assimilation systems has been extended from clear–sky condition to cloudy and precipitating conditions in the last decades [*Geer et al.*, 2018]. For example, *Viltard et al.* [2006] retrieved rain rates from the TRMM TMI brightness temperature measurements using a database based on the TRMM PR. *Bauer et al.* [2010] and *Geer et al.* [2010] directly assimilated the radiance measurements from the Special Sensor Microwave Imager (SSM/I) and the Advanced Microwave Scanning Radiometer for Earth Observing System (AMSR–E) into the ECMWF operational data assimilation system. *Kummerow et al.* [2015] developed a precipitation algorithm for GPM GMI using a database built on combined radiometer and radar observations. Recently, *Seo et al.* [2016] developed a cloud–radiation database optimized by a one–dimensional variational approach for retrieving hydrometeor

profiles from the TMI brightness temperature measurements over ocean. Nevertheless, the applications of passive microwave observations to snowfall retrievals and predictions are still under development [*Noh et al.*, 2006; *Liu and Seo*, 2013]. Only a few spaceborne microwave sensors have suitable channels for detecting snow signatures.

In 2014, the GPM core satellite [*Hou et al.*, 2014] was launched. Its microwave radiometer, GMI, provides the global microwave radiance measurements of high spatial resolution. Compared to its predecessor TMI, GMI has nine similar channels ranging from 10 to 89 GHz and four additional channels at 166 and 183 GHz. As shown by *Bennartz and Bauer* [2003], a channel around 150 GHz is essential for detecting snow scattering signatures. The sensitivity of water vapor channel at 183 GHz to snow particle scattering is weaker but still significant for the dry atmosphere. Compared to its predecessor TMI, the addition of the 166 and 183 GHz channels allows GMI to measure precipitation across a wide intensity range from heavy rainfall in the tropics to snowfall at high latitudes. A preliminary sensitivity test indicated that the 166 and 183 GHz channels contain the primary information on snow scattering among all the GMI channels. Inclusion of radiance measurements at these channels is necessary for snowfall retrievals and predictions.

To effectively use the 166 and 183 GHz measurements under all weather conditions for numerical weather applications, it is important to characterize the biases[1] for those channels by comparing measurements with radiative transfer simulations [*Auligné et al.*, 2007; *Lu et al.*, 2011; *Islam et al.*, 2016]. Moreover, the causes of the biases need to be understood, as they can originate from diverse sources including observations, radiative transfer model and input atmospheric fields. So far, bias characterization for microwave instruments has been rarely made

[1] Throughout this chapter, biases are defined as the mean difference between observed and simulated brightness temperatures, rather than instrument inaccuracy.

for snowfall conditions. The first reason is that the scattering properties of snow particles are complicated. *Kulie et al.* [2010] has demonstrated that the spherical particle models produce unrealistic simulations compared to microwave observations at 89 GHz and higher frequencies. As shown by *Geer and Baordo* [2014], the Mie theory that simply assumes snow particles being spheres as adopted in many radiative transfer models produces too little scattering at high frequencies (150–183 GHz). A method such as the DDA [*Draine and Flatau*, 1994] that can calculate the scattering properties of realistic nonspherical snow particles is required in simulating the microwave brightness temperatures in snow–containing clouds [*Liu*, 2004; *Kulie, et al.*, 2010; *Geer and Baordo*, 2014]. Second, the radiative model input of precipitation profiles from numerical weather models are heavily dependent on the employed microphysical schemes and therefore not always reliable [*Panegrossi et al.*, 1998; *Kim et al.*, 2013]. To alleviate this issue, combining passive and active microwave measurements is considered to be a good choice, since the radar measurements are directly related to the snow particle scattering and have been widely used to infer the snow particle properties [*Liu*, 2008a; *Hiley et al.*, 2011; *Heymsfield et al.*, 2016]. *Seo et al.* [2016] and *Yin and Liu* [2017] both utilized radar observations to constrain precipitation profiles as input to radiative transfer models. Their results suggested that radar observations generally lead to the radiative transfer simulations close to the observed brightness temperatures.

The purpose of this study is to assess the biases of observed minus simulated brightness temperatures for GMI channels at 166 and 183 GHz over ocean under snowfall conditions and understand the causes of these biases. A radiative transfer model that includes the scattering properties of nonspherical snow particles [*Liu*, 2004] is used to simulate the brightness temperatures at the high microwave frequencies. The input snow water content profiles are

derived from the CloudSat CPR measurements [*Stephens et al.*, 2002] rather than the GPM DPR. Since the minimum detectable reflectivity of DPR is about 12 dBZ over ocean [*Hamada and Takayabu*, 2015], the DPR tends to miss light and moderate snowfall events substantially [*Casella et al.*, 2017]. The biases under clear–sky conditions are also evaluated for comparison.

5.2 Data and Methods

The atmospheric hydrometeors that actively interact with upwelling microwave radiation under snowfall conditions are snow particles and cloud liquid drops. The former reduces upwelling radiation by scattering, while the latter enhances it by emission. To input snow water content into the radiative transfer model, we introduce the collocated CloudSat CPR measurements. For cloud liquid water, the GMI retrievals are used. In this section, the data sources are firstly introduced, followed by discussions on data processing such as pixel averaging and selecting data points under snowfall conditions. The derivation of hydrometeor profiles as input to the radiative transfer model is given in section 4.2.3. The radiative transfer model employed for simulating brightness temperature is finally described.

5.2.1 Data Sources

The primary datasets used in this study are brightness temperature and radar reflectivity measurements from the GPM GMI and CloudSat CPR. ECMWF analysis data are also used as the input atmospheric fields to the radiative transfer model.

The GMI has a total of 13 channels with central frequencies between 10 and 183 GHz. Its horizontal spatial resolution becomes finer at higher frequencies. The channels at 166 and 183 GHz have a spatial resolution of about 6 km. The nominal earth incidence angle for channels at 166 and 183 GHz is 49.2°, while the channels between 10 and 89 GHz have a nominal earth incidence angle of 52.8°. In the following, the channels at 166 and 183 GHz are referred to as

166V, 166H, 183±3V, and 183±7V channels, where the V/H represents the vertical/horizontal polarization.

The Jacobians of GMI channels at 166 and 183 GHz with respect to snow water content are presented in Fig. 5.1, in which the snow water content is assumed to be a constant of 0.2 g m^{-3} in the lowest 5 km layer. The Jacobians (gradients) of brightness temperatures with respect to snow water content are derived explicitly by adding a small perturbation to each layer of snow water content. It is seen that the 166V channel is sensitive to the column scattering, while the 183±7V channel mainly detects the scattering signatures at higher altitudes. The 183±3V channel is less sensitive to ice scattering than the other channels in the lower and middle troposphere.

The CPR is a nadir–looking radar that measures the backscattered power from cloud and precipitation at 94 GHz. Its minimum detectable reflectivity is about –30 dBZ. The horizontal spatial resolution is about 1.4 km across the track and 2.3 km along the track. A single CPR radar reflectivity profile contains a total of 150 bins with a vertical bin size of about 240 m.

A coincident dataset, 2B–CSATGPM [*Turk*, 2017], is employed in this study, which provides the collocated GMI brightness temperatures and CPR radar reflectivities, as well as ECMWF ancillary atmospheric fields interpolated to the CPR bin locations. In this dataset, a CPR radar reflectivity profile is matched to a nearest GMI pixel when two satellite tracks coincide within 15 minutes. Several other parameters distributed from the CloudSat and GPM products are also used, such as the CPR cloud masks and snow water contents as well as the retrieved GMI cloud ice and liquid water paths. The spatial coverage of datasets is from 65°S to 65°N. The period covers from March 2014 to December 2016.

5.2.2 Data Processing

Since the horizontal spatial resolution of CPR measurements (~2 km) is smaller than that of GMI measurements at 166 and 183 GHz (~6 km), all the CPR pixels within a searching radius of 4 km around the center of GMI pixel are averaged to match a GMI pixel. Since CPR pixels cannot fill a whole GMI pixel due to its nadir looking design, it is assumed that cloud properties are generally homogenous in the CPR cross track direction within a GMI pixel. The averaged CPR radar reflectivity ($Z_{e,avg}$) at each bin matched to a single GMI pixel is expressed as

$$Z_{e,avg} = \frac{1}{n}\sum_{i=1}^{n} w_i Z_{e,i} , \tag{5.1}$$

and

$$w_i = \frac{r_i^{-2}}{\sum_{i=1}^{m} r_i^{-2}} , \tag{5.2}$$

where $Z_{e,i}$ represents the radar reflectivity in linear scale at each bin for the ith CPR pixel in a GMI pixel, r_i is the distance between the center of the GMI pixel and the ith CPR pixel, and n is the total number of CPR pixels within the searching radius. w_i is the inverse distance weighting factor for the ith CPR pixel and is proportional to the square of r_i. Similarly, a clear fraction (F_{avg}) for a GMI pixel is determined using the CloudSat cloud mask. A clear flag (F_i) for a CPR pixel is firstly defined as

$$F_i = \begin{cases} 1, & \text{CPR cloud mask = 0 above surface clutter layer} \\ 0, & \text{otherwise} \end{cases} . \tag{5.3}$$

The clear flag for area covering the GMI pixel is then expressed as

$$F_{avg} = \frac{1}{n}\sum_{i=1}^{n} w_i F_i . \tag{5.4}$$

A GMI pixel is considered as clear–sky when its clear fraction is larger than 90% with the GMI cloud liquid and ice water paths less than 50 g m^{-2}. Otherwise, this GMI pixel is considered cloudy. A cloudy pixel with the matched CPR radar profile failing to pass the precipitation threshold (–15 dBZ) is considered as cloudy without precipitation conditions.

To select those GMI pixels associated with the snowfall near the surface, a parameterization of snowfall probability [*Sims and Liu*, 2015] is employed. Different from previous studies on snow–rain separation [*Liu*, 2008a; *Kienzle*, 2008], this parametrization accounts for the low–level temperature lapse rate, because the temperature inversion strongly affects a precipitation phase and is commonly observed near the polar regions [*Curry et al.*, 1996; *Connolley*, 1996]. Surface air wet–bulb temperature and temperature lapse rate in the lowest 0.5 km calculated from ECMWF ancillary atmospheric fields for CloudSat are utilized to calculate the snowfall probability. A cloudy GMI pixel with the calculated snowfall probability larger than 50% and the matched CPR radar profile passing the precipitation threshold (–15 dBZ) is considered as snowfall conditions even there is no frozen precipitation near the ground.

After the above data processing, we finally have about 80000 clear–sky, 110000 cloudy without precipitation and 24000 snowfall data points, and their geolocations are displayed in Fig. 5.2. The longitudinal distributions of clear–sky, cloudy without precipitation and snowfall data points are more homogeneous in the southern hemisphere. Most of snowfall data points are distributed poleward of 50° latitude. Additionally, about 86000 data points do not fall into the above three conditions and belong to rainfall conditions.

5.2.3 Input Hydrometeor Profiles

The cloud liquid water profiles are based on the retrieved GMI cloud liquid water paths provided by the GMI level 2 product (Passive Microwave Algorithm Team Facility, 2017).

The cloud liquid water in the vertical atmospheric column is evenly distributed in a 1 km layer. The layer location is determined by the highest relative humidity between 0.5 and 3 km. Using the vertical distribution of cloud liquid water from the collocated ECMWF analysis yields the similar simulation results.

The snow water content profiles are generated from the CPR radar reflectivity profiles. The radar reflectivities in the surface clutter layer (0 to ~1 km) are assumed to be the same as the first bin above the clutter layer. Since the CPR operates at W band, its radar reflectivity may experience measurable attenuation due to atmospheric gas, cloud liquid water and snow [*Matrosov*, 2007; *Kneifel et al.*, 2011]. Attenuation correction has been performed for atmospheric gases and cloud liquid water. The gaseous attenuation is given by the CloudSat 2B–GEOPROF product. The attenuation due to cloud liquid water is corrected using the derived cloud liquid water profiles [*Salonen and Uppala*, 1991]. The attenuation due to snow is not accounted for, because we lack the reference radar at Ku band [*Kulie et al.*, 2014]. Under heavy snowfall conditions, this type of attenuation may have been partially compensated by the multiple scattering [*Matrosov and Battaglia*, 2009].

The Z_e–SWC relation is developed to covert radar reflectivity to snow water content. Three snow particle types are chosen in deriving this relation: sectors, dendrites [*Liu*, 2008b] and oblate aggregates [*Honeyager et al.*, 2016]. The backscatter cross sections of the three snow particle types are calculated using the DDA method [*Draine and Flatau*, 1994]. Specifically, the radar reflectivity factor (Z_e) is expressed in (2.5), and the snow water content can be expressed as

$$\mathrm{SWC} = \int_{D_{min}}^{D_{max}} N(D)m(D)dD\,, \tag{5.5}$$

where D_{min} and D_{max} are lower and upper limits of the snowflake size, N(D) is the particle size distribution, m(D) is the mass of the particle with maximum dimension D. Based on previous

experimental and modeling studies focusing on snowfall events at high latitudes [*Braham*, 1990; *Senn and Barthazy*, 2004], the exponential particle size distribution in (4.1) is assumed. The values of N_0 and Λ are taken from the field experiments conducted by *Braham* [1990]. The Z_e–SWC relation is derived using least squares fitting of all data points for three snow particle types and can be expressed as

$$SWC=0.024Z_e^{0.75}. \tag{5.6}$$

Our comparison results indicate that the bias characteristics shown in later sections using this Z_e–SWC relation are very similar to those using snow water content profiles from CloudSat 2C–SNOW–PROFILE product [*Wood et al.*, 2014] that utilizes a variational method to retrieve snow–related quantities from CPR radar reflectivities, which suggests that the uncertainty in Z_e–SWC relation only has a secondary impact on bias characteristics.

The distance–height cross section of CPR derived snow water content and the GMI brightness temperature depressions at 166 and 183 GHz are presented in Fig. 5.3 for a case on April 11, 2015. The brightness temperature depression is calculated as the brightness temperature difference between a snowfall GMI pixel and a nearest clear–sky GMI pixel. There are five individual snow cells with snow water content values larger than 0.2 g m^{-3}. For the snow cell near 57.5°S, the brightness temperature depressions can even reach about –40 K at 166V and 166H channels, while the brightness temperature depression at 183±3V channel is only about –10 K. It is also seen that the brightness temperature depression at 166H channel is positive for the snow cell near 60.5°S possibly due to the existence of cloud liquid water. From this case, the GMI brightness temperature depressions at 166 and 183 GHz correspond to those snow cells well, indicating their capability of detecting snow scattering signatures.

5.2.4 Radiative Transfer Model

The radiative transfer model for calculating the GMI brightness temperatures was developed by *Liu* [1998]. It used a 4–stream discrete ordinate method to solve the radiative transfer equation. One of the radiative transfer model's unique features is that the single scattering properties of nonspherical snow particles are based on the results of DDA modeling [*Liu*, 2004]. The available snow particle types in the model have been extended from simple crystals (i.e., rosette, sector and dendrite) [*Liu*, 2008b] to complex aggregates [*Nowell et al.*, 2013]. In this study, the results using dendrite snow particles are mainly presented, since this snow particle type leads to the smallest departures between observed and simulated brightness temperatures. The exponential particle size distribution in (4.1) is employed in the radiative transfer model.

5.3. GMI Bias Characteristics at 166 and 183 GHz

In this section, the bias characteristics of observed minus simulated brightness temperatures for GMI channels at 166 and 183 GHz under clear–sky and snowfall conditions are presented. Hereafter, O and B denote observed and simulated brightness temperatures, respectively. The biases and standard deviations of O–B for GMI channels at 166 and 183 GHz under clear–sky and snowfall conditions using all collocated CloudSat and GMI pixels are shown in Table 1. Under clear–sky conditions, the biases at all channels are smaller than 1 K. The 183±3V channel has the largest bias of about 0.9 K, while the biases at other three channels are smaller than 0.3 K. Since the 183±3V channel is highly sensitive to water vapor, its larger bias is possibly caused by the biases in the model water vapor profiles. Under snowfall conditions, the 166H channel has the largest bias of about 2.9 K, while other channels have biases smaller than 1 K. The largest standard deviation is observed at 166H channel under clear–

sky and snowfall conditions due to its larger dynamic range; it can be as large as 6.5 K under snowfall conditions. Comparing results between clear–sky and snowfall conditions, it is found that the biases and standard deviations for 166V/H and 183±7V channels are larger under snowfall conditions than under clear-sky conditions. The differences in bias and standard deviation for 183±3V channel between clear–sky and snowfall conditions are minimal, since this channel is less sensitive to ice scattering.

The biases and standard deviations of O–B for GMI channels at 166 and 183 GHz are also calculated under cloudy without precipitation conditions (Fig. 5.4), in which only data points with latitudes above 40° are included. It is found that the biases for 166V, 183±3V and 183±7V channels are of similar values under clear–sky and cloudy conditions, while the bias for 166H channel under cloudy conditions is much larger than that under clear–sky conditions. From cloudy to snowfall conditions, the increments in biases for 166V and 166H channels and the decrements in biases for 183±3V and 183±7V channels are smaller than 1 K. Assuming a constant liquid water content value of 0.1 g m^{-3} in the lowest 2.5 km layer, the Jacobian near the surface for 166V channel with respect to liquid water content is about 5 K g^{-1} m^3, while it for 166H channel can reach about 15 K g^{-1} m^3 near the surface. In other words, the 166H channel is more sensitive to liquid water emission than the 166V channel. On the other hand, the 166V channel is more sensitive to ice scattering than the 166H channel as seen in Fig. 5.1. Therefore, the large bias for 166H channel under cloudy and snowfall conditions is likely attributed to the biases in cloud liquid water profiles. The biases in snow water profiles and model scattering calculations only contribute a small portion to the total bias of O–B for that channel. Otherwise a large bias should have been observed for 166V channel as well. The standard deviations under

the nonprecipitating condition (clear–sky and cloudy) are relatively stable, while the standard deviations for 166V/H and 183±7V channels are much larger under snowfall conditions.

Fig. 5.5 shows the relation between O–B and B under clear–sky and snowfall conditions. It is seen that the observed brightness temperatures are generally consistent with the simulated ones under clear–sky conditions. On the other hand, it is found that the spread of O–B becomes larger as the simulated brightness temperatures get lower (more intense snowfall) under snowfall conditions, i.e., increasing the inconsistency between observed and simulated brightness temperatures. It is also noticed that the distribution of O–B for 166H channel migrates upward along y axis as simulated brightness temperature decreases under the snowfall condition, corresponding to the largest bias for this channel as seen in Fig. 5.4. As mentioned above, this migration of O–B for 166H channel is likely caused by errors in cloud liquid water profiles. The root cause of these remaining biases under snowfall conditions will be investigated later.

Sensitivity test is conducted by changing snow particle types in the radiative transfer model. In Fig. 5.6, we show the biases of O–B for 166 and 183 GHz channels under snowfall conditions assuming snow particle types as rosette, sector, dendrite and aggregate in the radiative transfer model. The scattering properties of aggregate were calculated by *Nowell et al.* [2013], while those for other snow particle types are developed by *Liu* [2008b]. Data points are divided into three groups according to their snow water paths (SWPs) calculated from CPR derived snow water contents. In group 1 (SWP < 50 g m^{-2}), the biases are of similar values when using different snow particle types. In group 2 ($50 \leq$ SWP < 200 g m^{-2}), the biases are the largest when using rosette and the smallest when using dendrites. In the group 3 (SWP ≥ 200 g m^{-2}), it is seen that the biases are much larger when using rosette than those using other snow particle types, implying that using rosette significantly overestimates ice scattering. The GMI 166V, 183±3V

and 183±7V channels have the smallest biases when using dendrites, while the GMI 166H channel has the smallest bias when using aggregate. It is worth mentioning that in group 3, the biases for GMI 166V/H and 183±7V channels are negative when using dendrites and positive when using other snow particle types. Fig. 5.7 is the same as Fig. 5.6 except for standard deviations. It is seen that the standard deviations are similar when using different snow particle types in the group 1, while they are much larger when using rosette than using other snow particle types in the group 3. From this sensitivity test, it seems that dendrites work reasonably well overall, especially when snow water path is moderately low. On the other hand, rosette type only works comparably well at very low values of snow water path. At high snow water paths, aggregates outperform for the 166H channel.

5.4. Analysis of GMI Remaining Biases at 166 and 183 GHz

From previous results, it is seen that the large biases of O–B occur for the GMI 166V/H and 183±7V channels under snowfall conditions when brightness temperatures are relatively low. For instance, some data points are associated with biases of magnitudes larger than 10 K when the brightness temperatures at 166V channel are around 240 K (see Fig. 5.5). In this section, we analyze the possible causes of the remaining biases for the GMI channels at 166 and 183 GHz under snowfall conditions.

The dependence of O–B on ice water path for these GMI channels under snowfall conditions is shown in Fig. 5.8. The ice water path comes from the 2A–GPROF–GMI product [*Passive Microwave Algorithm Team Facility*, 2017]. It is noted that the GMI retrieved ice water path is not independent of brightness temperatures at GMI high frequency channels. Here this variable is only used as an indicator of the presence of ice in the GMI observations. It is seen that the values of O–B are more concentrated along the line of zero value with the increase of ice

water path. Some values of O–B are large and positive for 166V/H and 183±7V channels when ice water path is smaller than 20 g m^{-2}. In addition, it is observed that there are some data points associated with large negative values of O–B for 166H channel when ice water path is larger than 80 g m^{-2}. Fig. 5.9 is the same as Fig. 5.8 except for O–B dependence on CPR derived snow water path. It is found that the values of O–B spread broadly when snow water path is large. Some values of O–B are large and negative for the 166V/H and 183±7V channels when snow water path is larger than 600 g m^{-2}. The large positive values of O–B are only observed for the 166H channel when snow water path is smaller than 100 g m^{-2}. Since the GMI ice water path and the CPR snow water path are both intended to represent the amount of ice, it is expected that the dependence of O–B on the two variables should be similar, which is not seen in Figs. 5.9 and 5.10. One obvious reason is that the two variables are derived from two different instruments, which leads to the discrepancy.

The biases of O–B in two–dimensional space of the aforementioned ice and snow water paths under snowfall conditions are shown in Fig. 5.10. Large negative biases are found at 166V/H and 183±7V channels on the upper right corner where the ice and snow water paths are both large. In this region it is likely that snowfall is intense and the CPR radar reflectivity experiences significant attenuation. Since the snow water content profiles used in the simulations are derived from CPR radar reflectivity, the attenuation in CPR radar reflectivity leads to positive biases in simulated brightness temperatures and therefore large negative biases in O–B. Some positive biases are found for 166V/H and 183±7V channels on the bottom right corner where snow water path is large, but the ice water path is small. In this region, the CPR measures obvious ice scattering signatures, while the GMI only detects weak ice scattering. This discrepancy is likely caused by spatial and/or temporal mismatches between two instruments. It

is worth mentioning that since we selected data points based on the CPR precipitation threshold in this study, it is likely that some matched GMI pixels contain more or less precipitating ice particles due to this sampling method, which can partly contribute to the large biases observed under high snow water paths. This sampling bias has been explored by *Geer and Bauer* [2011] in the context of numerical weather forecast simulations. It is also noticed that large positive biases are found for the 166H channel when snow water path is smaller than 100 g m^{-2}. This region may be divided into two parts: one is associated with light precipitation where ice and snow water paths are both small, and the other is with large ice water path but small snow water path. In the second part, the GMI measures strong ice scattering, while the CPR misses much of ice scattering signature. As discussed later in this section, it appears that this part is associated with shallow snow cells where the CPR is not able to fully observe them due to surface clutter. The positive biases in the two parts are both likely caused by the negative biases in cloud liquid water profiles.

The relation between the biases of O–B and snow cloud geometric properties is also investigated. The dependence of biases of O–B on snow top height and snow layer depth is shown in Figs. 5.11 and 5.12, respectively. Snow top height is defined as the height of the highest level with CPR radar reflectivity lager than –15 dBZ. The snow layer depth is defined as the distance between bottom and top snow levels. Larger positive biases are observed for the 166H channel when snow top height is lower than 3 km. Similarly, positive biases for the 166H channel are found when the snow layer depth is smaller than 3 km. As mentioned earlier, the positive biases for this channel are likely caused by the negative biases in GMI cloud liquid water profiles, since the emission from liquid water in shallow snow clouds can contribute significantly to the observed brightness temperature. It is seen that negative biases for 166V/H

and 183±7V channels occur when snow top height is higher than 8 km. Similarly, large negative biases for those channels are observed when snow layer depth is larger than 8 km. In other words, negative biases for 166V/H and 183±7V channels are associated with deep snow clouds where the strong attenuation in CPR radar reflectivities and the possible sampling bias cause negative biases of O–B. Additionally, snow cloud properties in two regions in Fig. 5.10 are examined. Region 1 is for ice water path > 120 g m^{-2} and snow water path > 700 g m^{-2}, and region 2 is for ice water path > 80 g m^{-2} and snow water path < 60 g m^{-2}. In region 1, mean snow top height and layer depth are about 8.2 km, while in region 2, mean snow top height and layer depth are about 4.1 km, consistent with the discussions given above.

Finally, a case for shallow snow cells and a case for deeply convective clouds are presented in Fig. 5.13. In the first case, the individual shallow snow cells near 51°S and 53°S are associated with positive biases of O–B for 166H channel (> 5 K) due to negative biases in cloud liquid water profiles. In the second case, the deep convective clouds near 52°N and 53°N are associated with negative biases of O–B for 166V/H channels (< –14 K) due to the attenuation in radar reflectivities and the possible sampling bias.

5.5. Conclusions for Assessment of Microwave High Frequency Measurements

The GMI provides nearly global measurements of high spatial resolution microwave radiances at 166 and 183 GHz. It is valuable to apply data at these channels to snowfall retrievals and predictions. To do so, it is useful to firstly understand the bias characteristics of observed minus simulated brightness temperatures at these channels under snowfall conditions. For this purpose, a radiative transfer model that includes single scattering properties of nonspherical snow particles based on DDA calculations is used to simulate brightness temperatures at 166 and

183 GHz. The input snow water content profiles are derived from CloudSat CPR measurements rather than outputs of numerical weather prediction models.

Results show that the biases of O–B averaged over more than 2 years of coincident CloudSat and GMI pixels under snowfall conditions are smaller than 1 K except for the 166H channel that has the largest bias of about 3 K. At the 166H channel, it also has the largest standard deviation of about 6.5 K, while at other GMI channels, the standard deviations are smaller than 4 K.

By analyzing the results, we have identified two major possible causes for the discrepancy between simulated and observed brightness temperatures. All of them are related to the inputs for radiative transfer simulations, and each of them occurs under specific cloud conditions and affects individual channels differently. One is due to errors in cloud liquid water profiles for which we chose to use GMI retrievals as radiative transfer model input. This problem impacts the most on the 166 H channel and occurs for shallow snow cells with or without substantial snowfall. Based on the study of *Kulie et al.* [2016], there are abundant shallow snow cloud cells globally and they can be associated with strong convection and heavy snowfall. In shallow snow cells, cloud liquid water may be rich and contributes substantially to the observed brightness temperatures. *Wang et al.* [2013] has shown that the warming by liquid water emission has a similar magnitude to the cooling by ice scattering on microwave brightness temperatures with frequencies higher than 80 GHz. The biases in cloud liquid water profiles lead to the large biases in simulated microwave brightness temperatures for those channels sensitive to surface emission. Therefore, it is important to improve the cloud liquid water retrieval algorithms in the future. The second cause for the large biases of O–B occurs when the clouds are deep and with heavy snowfall. Under this condition, CloudSat CPR experiences substantial

attenuation and GMI observations may contain some negative biases due to the sampling method, which leads to higher simulated brightness temperatures and negative biases of O–B. This problem impacts the 166 channels the most, followed by the 183±7V channel.

In addition, a sensitivity test is conducted by varying snow particle types in the radiative transfer model. The results indicate that dendrites work well for low and moderate snow water paths. On the other hand, rosettes only work comparably well at very low values of snow water path. When snow water path is high, aggregates outperform for the 166V channel. In this study, it is not our intention to claim that dendrites are prevalent in studied snow clouds, since they grow in a narrow temperature range. Instead, our finding indicates that snow aggregates [*Petty and Huang*, 2010; *Leinonen and Szyrmer*, 2015] with similar scattering properties to dendrites developed by *Liu* [2008b] work well in simulating microwave high frequency brightness temperatures. Snow aggregates have been shown to grow in a broad temperature range from 273 to 213 K [*Pruppacher and Klett*, 1997; *Nowell et al.*, 2013]. As mentioned by *Kulie et al.* [2010], the uncertainty in snow particle types is still quite large, it is important to further examine the realism of various snow particle types under different cloud conditions.

While other uncertainties may still exist, this study provides useful configurations for simulating GMI brightness temperatures at 166 and 183 GHz and the physical understandings for the remaining biases of O–B for these channels under snowfall conditions.

Table. 5.1. Biases and standard deviations of O–B for GMI channels at 166 and 183 GHz under clear–sky and snowfall conditions.

	bias (K)		std (K)	
	clear–sky	snowfall	clear–sky	snowfall
166V	-0.28	0.85	1.42	3.58
166H	0.23	2.86	2.80	6.49
183±3V	0.86	0.82	1.34	1.52
183±7V	-0.03	-0.32	1.08	2.40

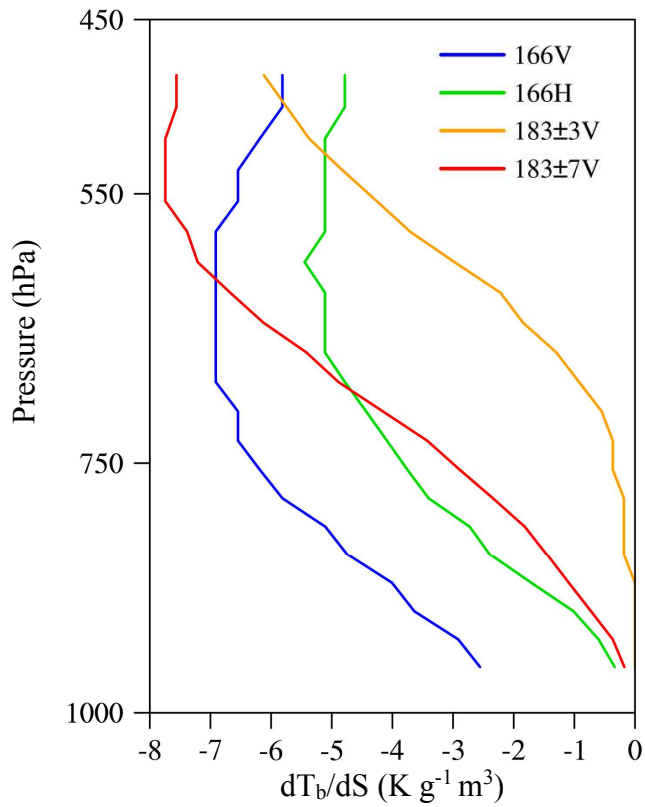

Fig. 5.1. Jacobians of GMI channels at 166V/H, 183.31±3V, and 183.31±7V GHz with respect to snow water content.

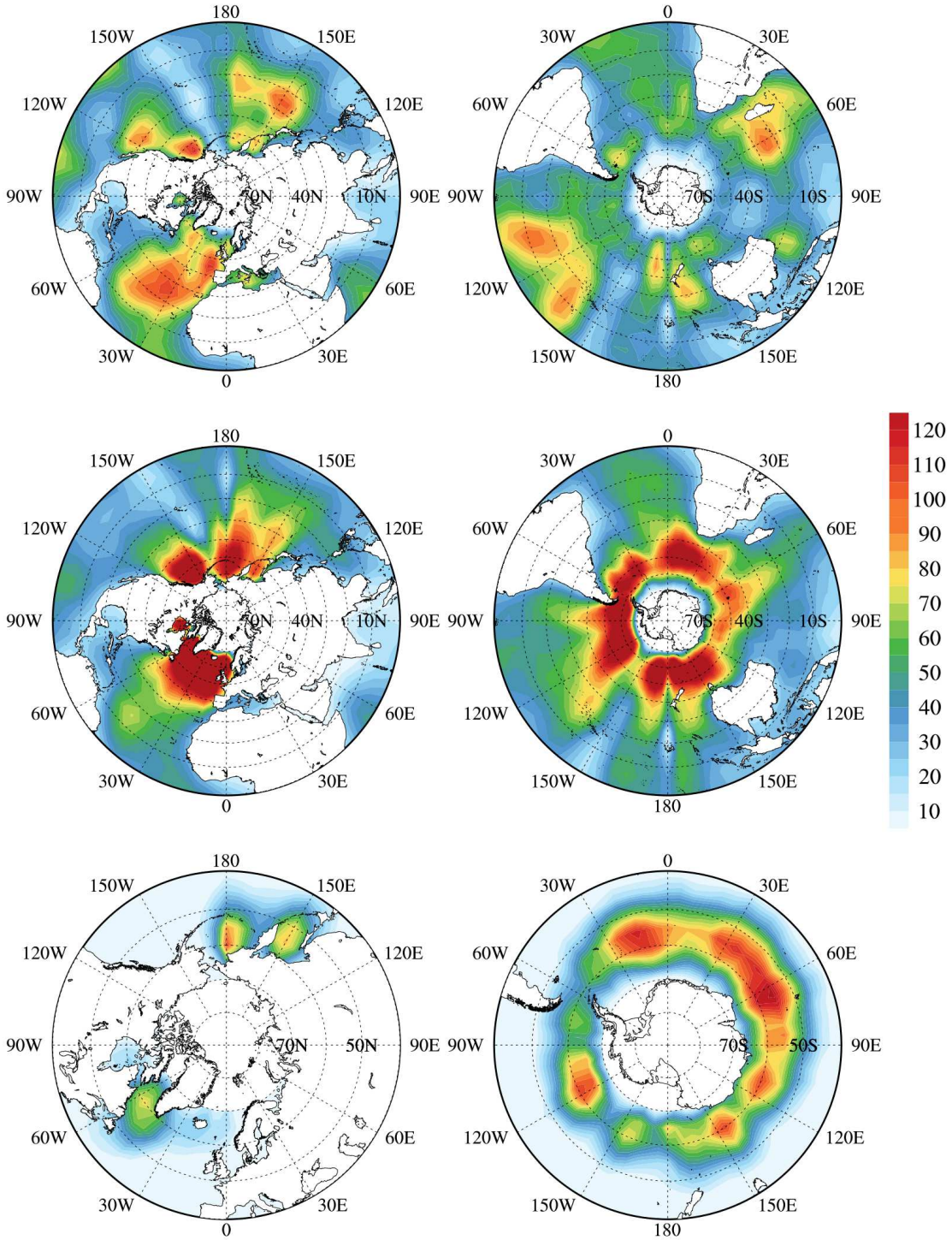

Fig. 5.2. Number of clear–sky (top panels), cloudy without precipitation (middle panels) and snowfall (bottom panels) data points within 5°×5° boxes.

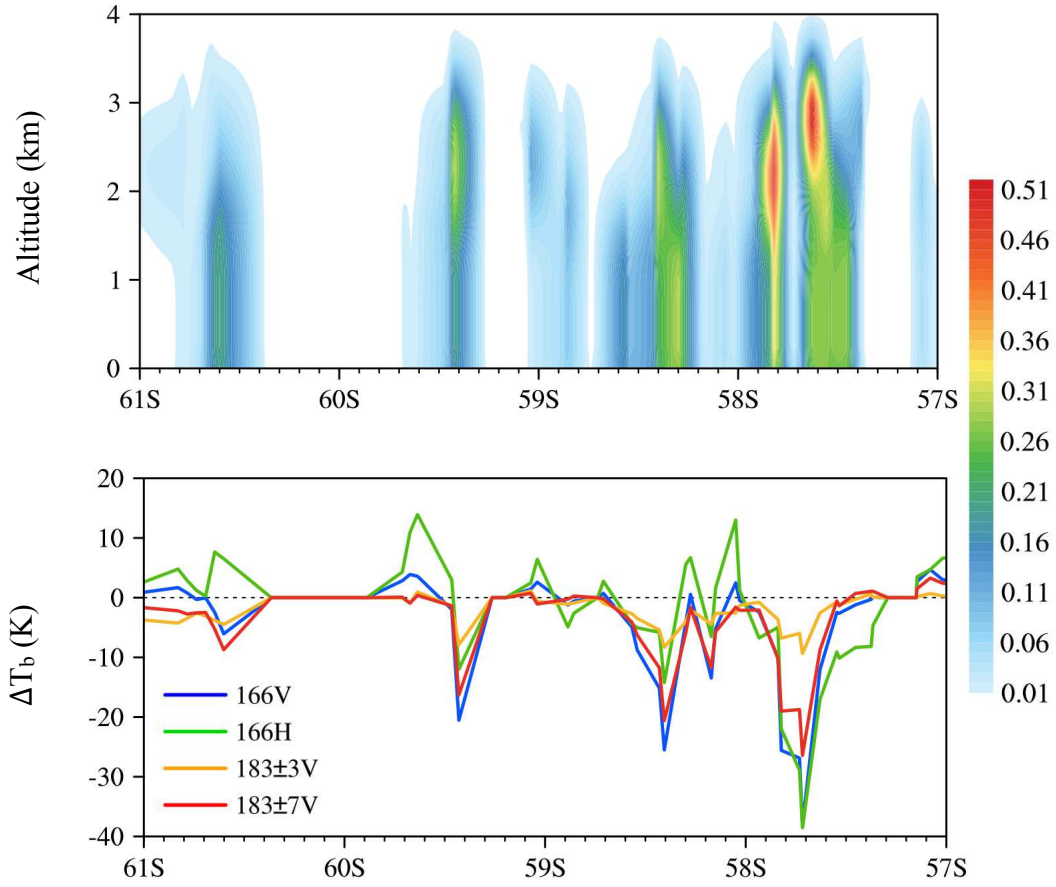

Fig. 5.3. Vertical cross section of CPR derived snow water content (unit: g m^{-3}) for a single case on April 11, 2015 (top panel) and GMI brightness temperature depressions at 166 and 183 GHz (bottom panel).

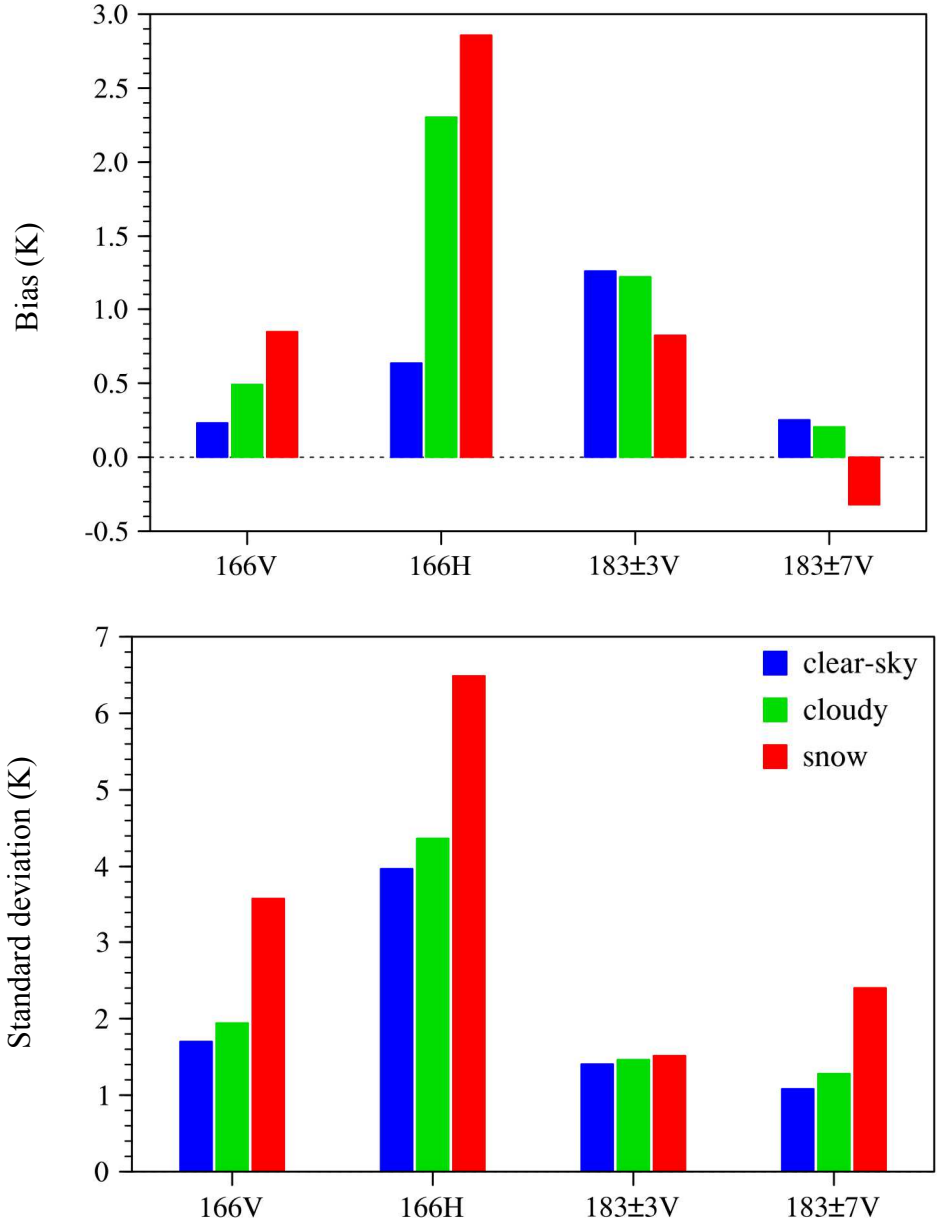

Fig. 5.4. Biases (top panel) and standard deviations (bottom panel) of observed minus simulated brightness temperature (O–B) for GMI channels at 166 and 183 GHz under clear–sky, cloudy without precipitation and snowfall conditions. Only data points with latitudes poleward of 40° are included.

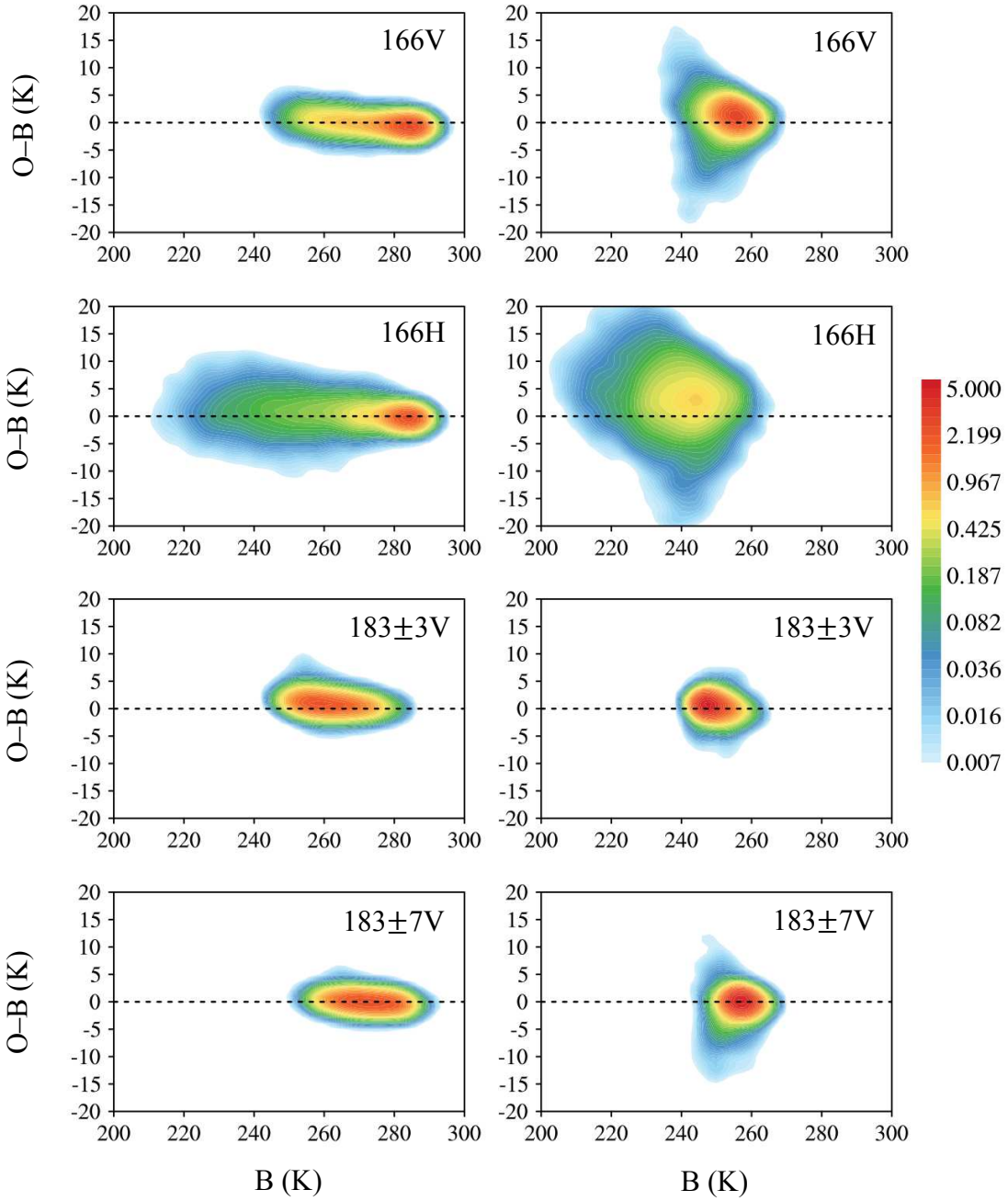

Fig. 5.5. Relation between observed minus simulated brightness temperature (O–B) and simulated brightness temperatures (B) for GMI channels at 166 and 183 GHz under clear–sky (left panels) and snowfall (right panels) conditions. Shading represents the occurrence frequency (unit: %).

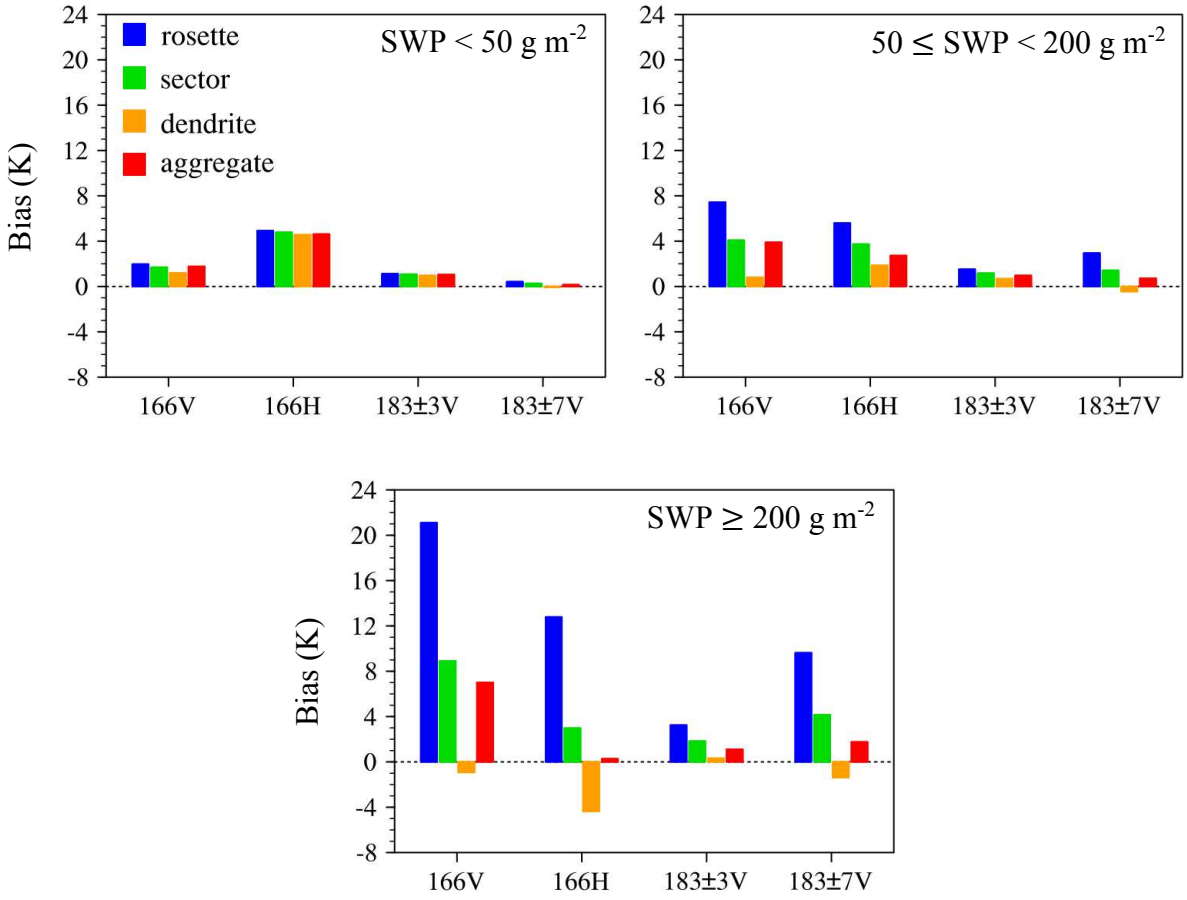

Fig. 5.6. Biases of observed minus simulated brightness temperature (O–B) for GMI channels at 166 and 183 GHz under the snowfall condition assuming different snow particle types in the radiative transfer model .

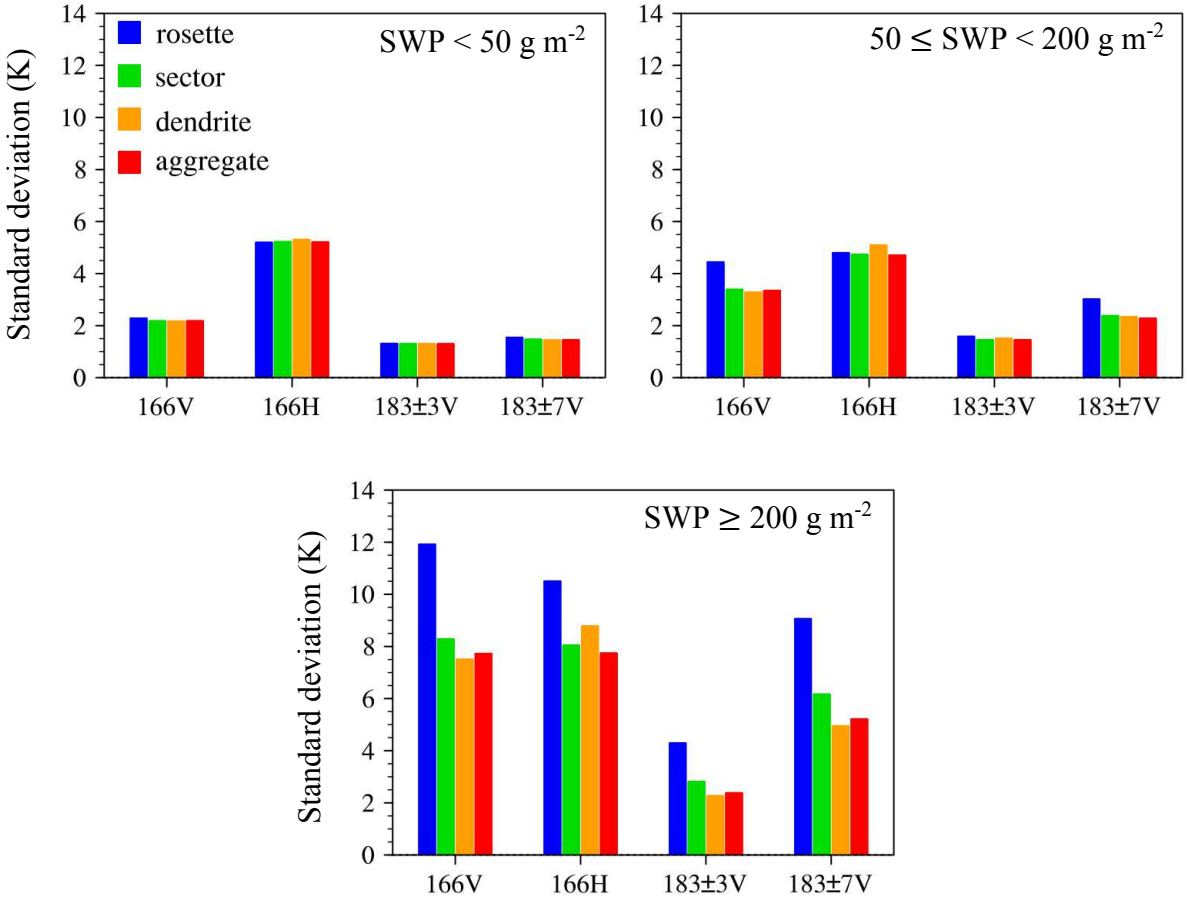

Fig. 5.7. Same as Fig. 5.6 except for standard deviations.

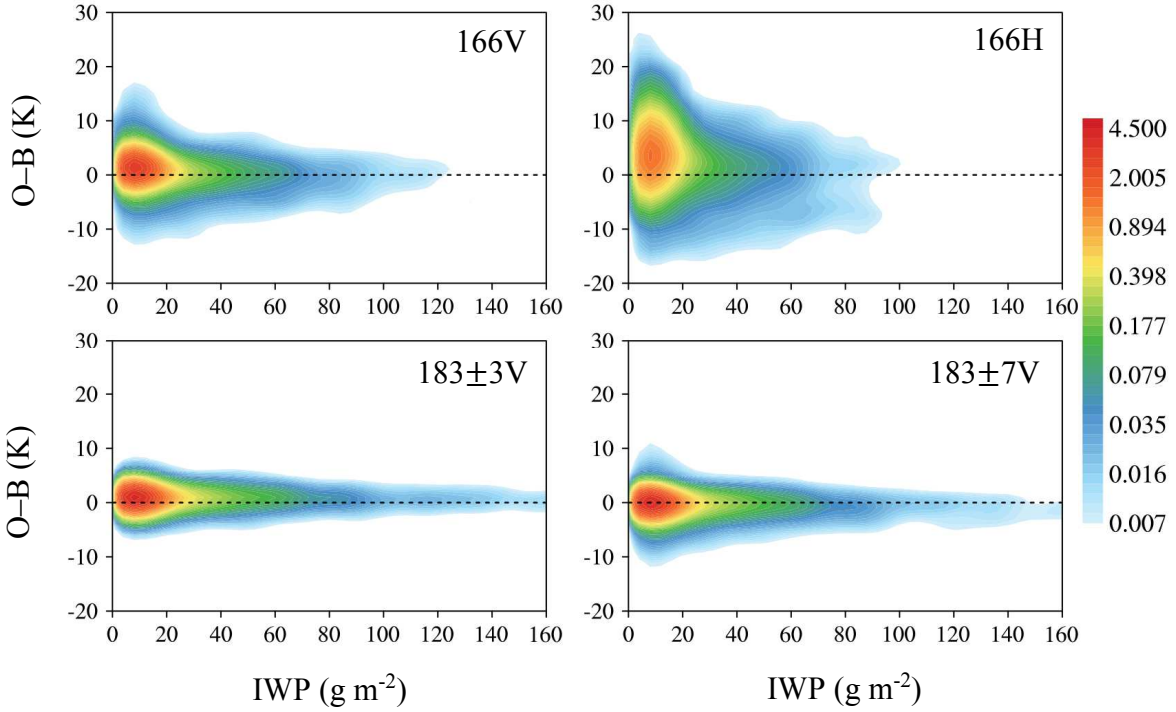

Fig. 5.8. Dependence of observed minus simulated brightness temperature (O–B) on ice water path (IWP) for GMI channels at 166 and 183 GHz under snowfall conditions. Shading represents the occurrence frequency (unit: %).

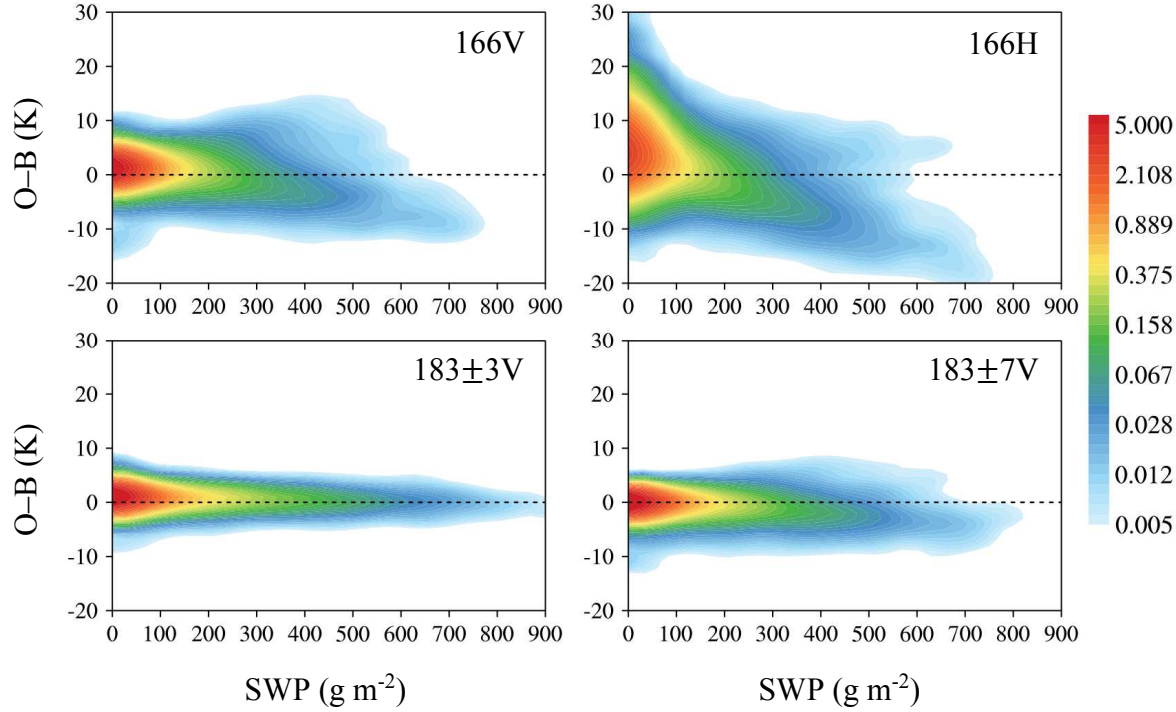

Fig. 5.9. Same as Fig. 5.8 except for dependence on snow water path (SWP).

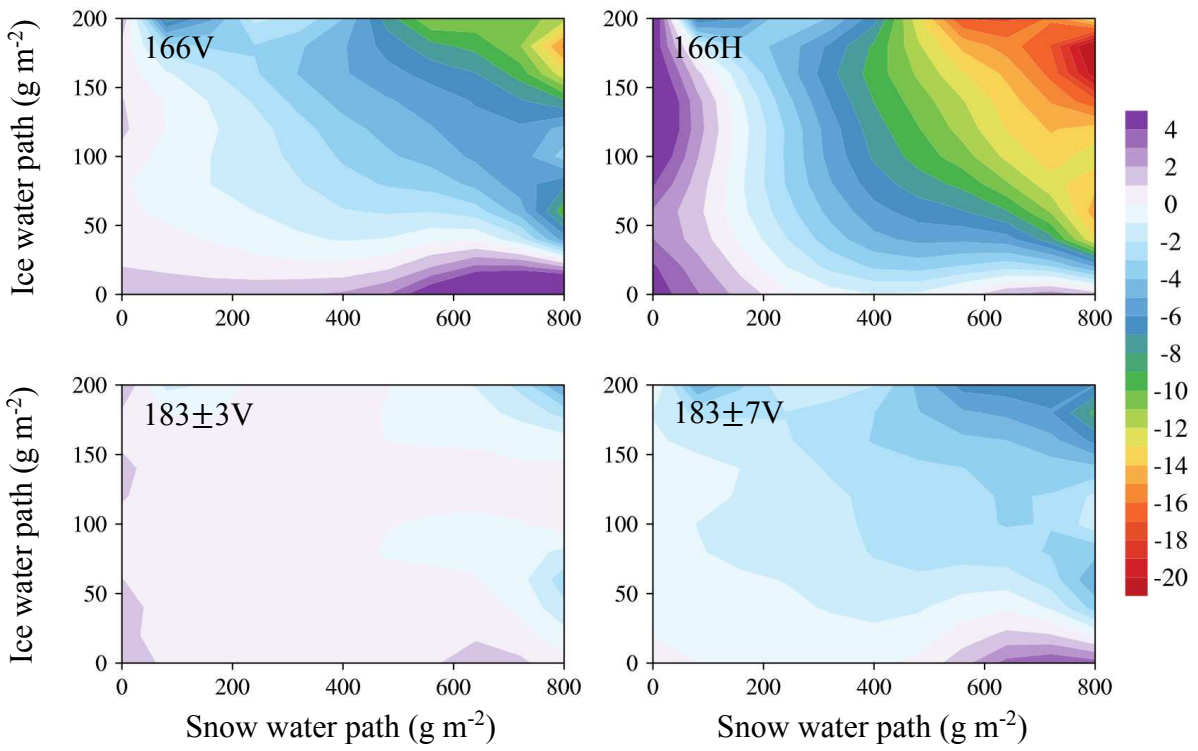

Fig. 5.10. Biases of observed minus simulated brightness temperature (O–B, unit: K) in two–dimensional space of ice and snow water paths for GMI channels at 166 and 183 GHz under snowfall conditions

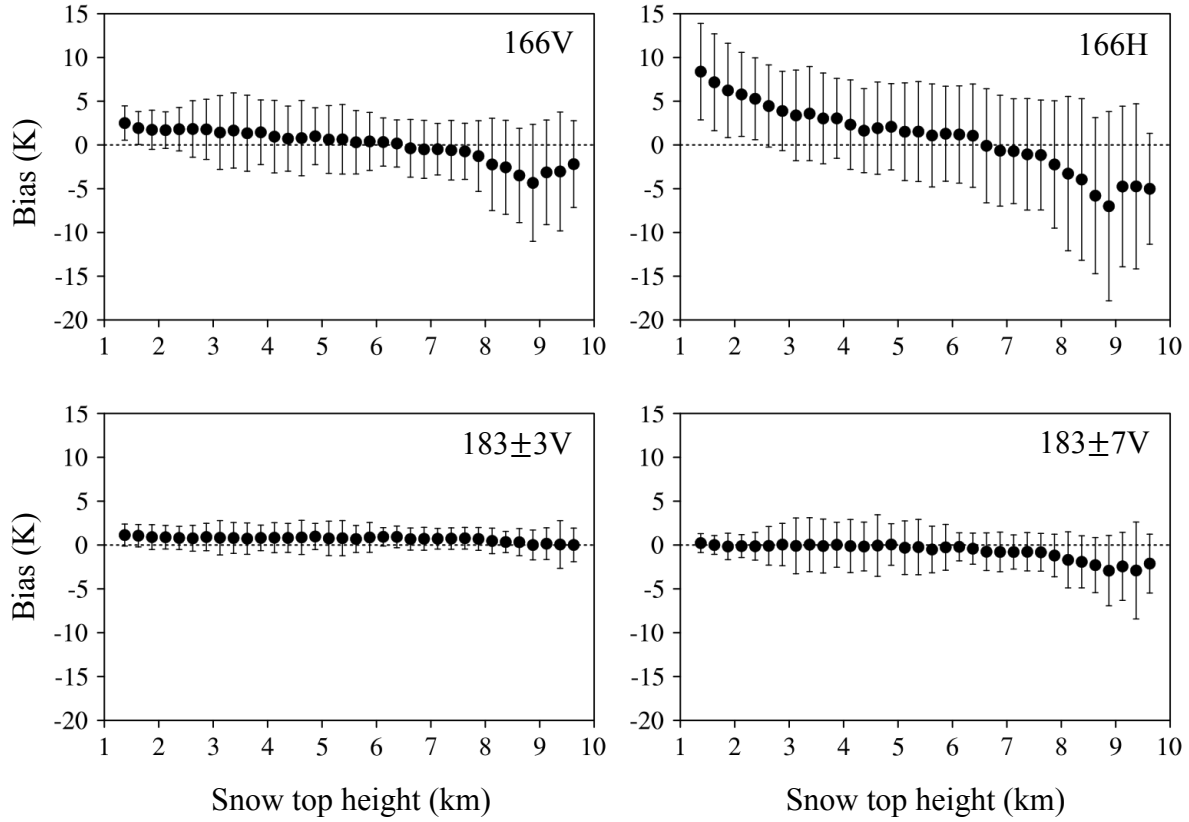

Fig. 5.11. Dependence of biases of observed minus simulated brightness temperature (O–B) on snow top height for GMI channels at 166 and 183 GHz under snowfall conditions. The length of the bar represents the twofold of standard deviations of observed minus simulated brightness temperature (O–B).

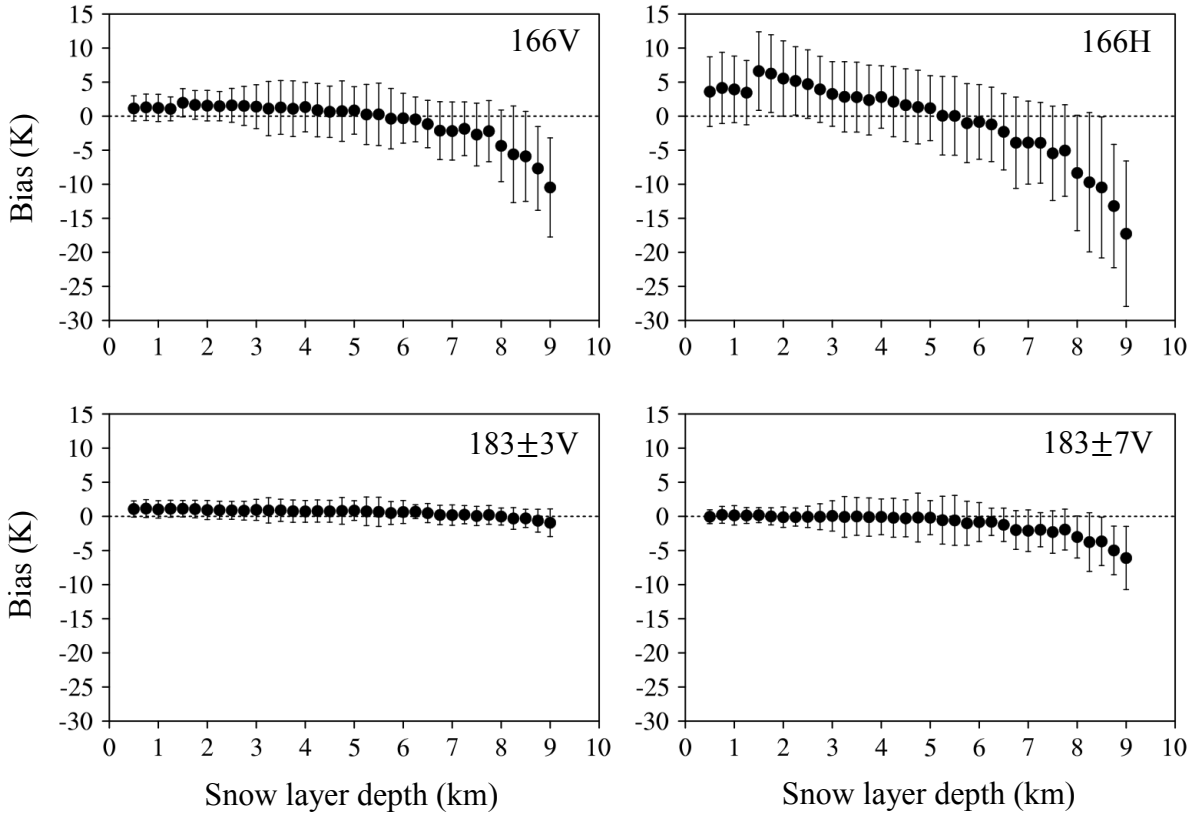

Fig. 5.12. Dependence of biases of observed minus simulated brightness temperature (O–B) on snow layer depth for GMI channels at 166 and 183 GHz under snowfall conditions. The length of the bar represents the twofold of standard deviations of observed minus simulated brightness temperature (O–B).

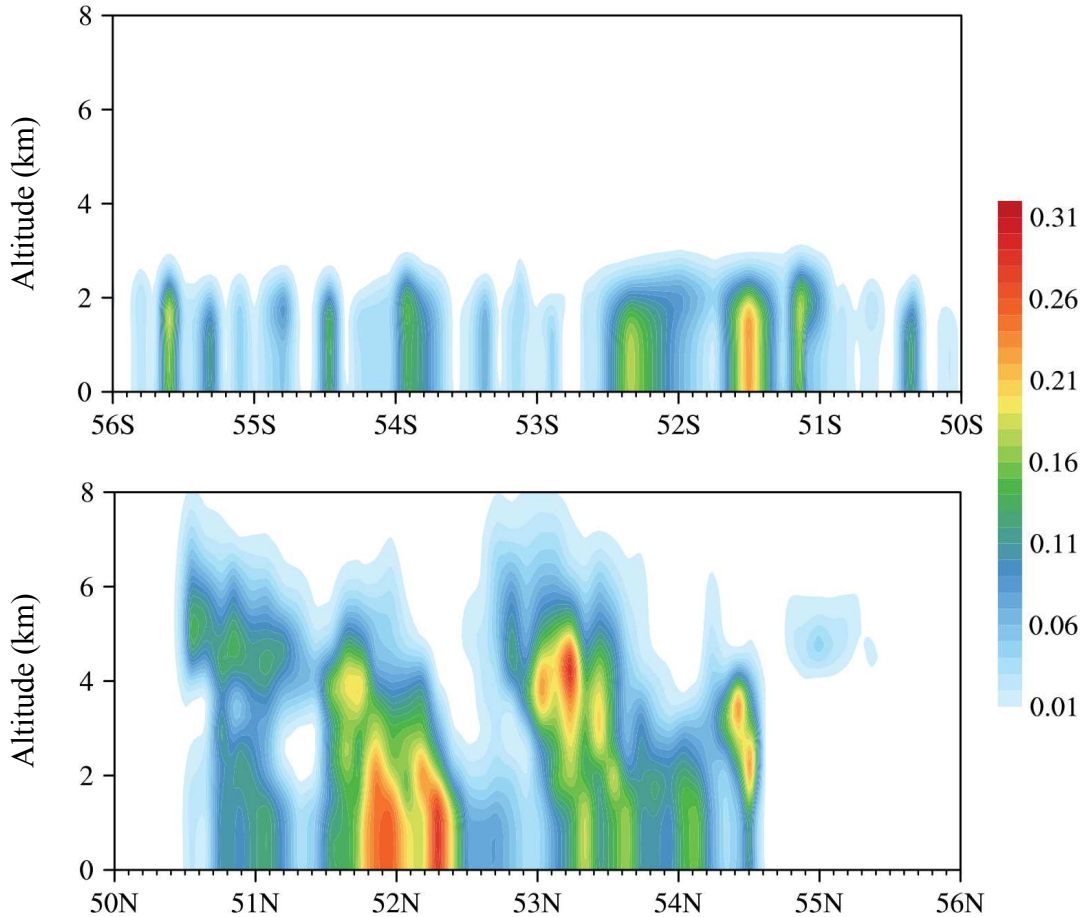

Fig. 5.13. A case for shallow snow clouds on June 12, 2015 (top panel) and a case for deep convective snow clouds on March 11, 2015 (bottom panel). The shading represents snow water content (unit: g m^{-3}).

CHAPTER 6

SNOWFALL RETRIEVAL ALGORITHM FOR GPM MICROWAVE IMAGER

After exploring the bias characteristics for GMI high frequency channels, it is practical to develop a snowfall retrieval algorithm for GMI. This chapter is organized as follows. The introduction to passive microwave snowfall retrieval is provided in section 6.1. Section 6.2 describes the data sources and methods used. Section 6.3 presents the results from 1D–Var optimization, including the statistics of the constructed *a priori* database. Section 6.4 applies this *a priori* database to retrieve snow water content profiles and evaluates its performance. Conclusions are given in section 6.5.

6.1 Introduction

In the past decades, global precipitation retrievals have been greatly advanced due to observations from passive microwave instruments onboard satellites. Early studies [*Ebert et al.*, 1996; *Ebert and Manton*, 1998] have demonstrated that microwave signatures are more sensitive to the amount of raindrops or ice particles in the atmosphere than their infrared counterparts. The success of TRMM [*Kummerow et al.*, 2000] further advanced the precipitation retrievals from passive microwave observations. Nevertheless, very few passive microwave retrieval methods focused on snowfall, although it is a major form of precipitation at high latitudes and has a distinct impact on global climate [*Liu*, 2008a]. Several reasons impede the development of passive microwave snowfall retrievals. First, the scattering properties of nonspherical snowflakes are not well understood, but clearly different from those of spherical particles [*Liu*, 2004; *Matrosov et al.*, 2005]. The scattering properties of snowflakes are very sensitive to their shapes and sizes [*Liu*, 2008b; *Kneifel et al.*, 2011]. Second, the snow signatures in passive microwave

observations are weak and only evident at high microwave frequencies. A sensitivity study conducted by *Bennartz and Bauer* [2003] showed that the scattering signatures in passive microwave radiances due to precipitating ice particles are not strong even at 85 GHz. Only at a frequency higher than 150 GHz do they become strong enough to retrieve snow–related quantities at middle and high latitudes. Consequently, only a few satellite sensors have been so far suitable for the purpose of snowfall retrievals. Finally, the emission by cloud liquid water can increase microwave brightness temperatures, which has a masking effect on the snow scattering signatures [*Liu and Seo*, 2013], thus further increases the difficulty of snowfall retrievals.

Toward developing a snowfall retrieval algorithm, progresses have been made in understanding the scattering properties of nonspherical ice particles and analyzing passive microwave measurements. For example, *Liu* [2004] presented two approximations for single scattering properties of various nonspherical snowflakes based on results of DDA [*Draine and Flatau*, 1994] calculations. Several databases of microwave scattering properties for nonspherical snowflakes have been developed, covering from simple pristine crystals [*Liu*, 2008b] to complex snow aggregates [*Petty and Huang*, 2010; *Honeyager et al.*, 2016]. Those studies provided the basis for simulating microwave brightness temperatures in radiative transfer models under snowfall conditions. In addition, *Liu and Curry* [1999] developed an over–ocean ice water path algorithm using the Special Sensor Microwave Water Vapor Sounder data. *Noh and Liu* [2006] presented a method to retrieve snow precipitation in the Wakasa Bay and surrounding areas by utilizing high microwave frequency channels from the Advanced Microwave Sounding Unit (AMSU). *Liu and Seo* [2013] proposed a statistical method to detect snowfall over land using passive microwave measurements from the Microwave Humidity Sounder (MHS). The encouraging results from these studies have demonstrated the values of

passive microwave measurements on global snowfall retrievals. With the recent launch of the GPM core satellite [*Hou et al.*, 2014], the onboard GMI provides the measurements with unprecedented high spatial resolution at high microwave frequencies ranging from 89 to 183 GHz and is a powerful tool for studying snow precipitation. Applying GMI measurements to snowfall retrievals is of great benefit to cloud and precipitation process studies.

The Bayesian technique [*Olson et al.*, 1996; *Evans et al.*, 2002] is an inversion method that has been widely used in the precipitation retrievals. It requires an *a priori* database that contains a large set of hydrometeor profiles and their corresponding brightness temperatures for a specific sensor. The construction of such *a priori* databases can be accomplished by utilizing results of cloud–resolving models [*Mugnai et al.*, 1993; *Marzano et al.* 1999; *Kummerow et al.*, 2001] or radar observations [*Seo and Liu*, 2005; *Noh et al.*, 2006; *Aonashi et al.*, 2009; *Kummerow et al.*, 2011]. One key step in developing a realistic *a priori* database is to ensure the physical consistency between geophysical parameters and observed sensor brightness temperatures. For this purpose, a one–dimensional variational (1D–Var) method is introduced here.

The 1D–Var approach iteratively finds a solution of geophysical parameters to best fit the observed sensor brightness temperatures, balancing with the prior information of geophysical parameters. It employs a radiative transfer model to translate the information of geophysical parameters to brightness temperatures. *Moreau et al.* [2003] applied this variational method to retrieve rain profiles from TMI over ocean, in which they utilized model–generated rain profiles as first guess and solved the analyzed rain profiles through iterations to find the best match between initial rain profiles and TMI observations. *Seo et al.* [2016] developed an optimized *a priori* database that connects hydrometeor profiles and TMI brightness temperatures over ocean

using 1D–Var approach. In their method, radar observations from TRMM precipitation radar (PR) were also included in the minimization of the cost function to further constrain the hydrometeor profiles generated from a cloud–resolving model. Recently, *Meng et al.* [2017] developed an overland snowfall rate retrieval algorithm for AMSU/MHS and ATMS sensors, in which a 1D–Var approach is used to derive ice water path first, and then the ice water path is converted to snowfall rate using an observation–based ice particle terminal velocity relation. It is worth mentioning that the three studies assumed some parameters as knowns. For *Moreau et al.* [2003] and *Seo et al.* [2016], all parameters except hydrometeor profiles are assumed to be known, while for *Meng et al.* [2017], land emissivity and surface temperature are also optimized, since the uncertainty in these two parameters is relatively large over land. Their positive results have demonstrated the benefits of utilizing 1D–Var approach to develop the *a priori* database for passive microwave precipitation retrievals.

This study aims to develop a physically optimized *a priori* database for GMI global snow water retrievals over ocean. The 1D–Var approach is employed to seek the optimal match between background snow water content profiles and GMI observations at high microwave frequencies. The first–guess snow water content profiles are based on CPR observations [*Stephens et al.,* 2002]. The flowchart for developing the *a priori* database is shown in Fig. 6.1. The first step includes selecting GMI pixels associated with solid precipitations and converting CPR radar reflectivities to initial snow water content profiles. Then, the 1D–Var optimization is performed on all snow water content profiles using collocated GMI measurements. A final step shows the application of the database for Bayesian snow water retrievals.

6.2 Data Sources and Method

In this section, the data sources and processing methods are mainly adopted from

chapter 5 with some modifications. The primary data sources are the collocated CPR radar reflectivities and GMI brightness temperatures. The atmospheric fields provides by ECMWF analysis are used as input to radiative transfer model. The time period of datasets covers from March 2014 to June 2016.

6.2.1 Data Sources and Processing

The creation of the *a priori* database starts with a coincident dataset, 2B–CSATGPM [*Turk*, 2017], which includes, among other variables, GMI brightness temperatures, CPR radar reflectivities, and ECMWF ancillary geophysical parameters collocated with CloudSat observations. Other parameters, such as CPR cloud mask, GMI retrieved cloud liquid and ice water paths, and GMI surface type index distributed from the CloudSat radar and GPM precipitation products, are also used in the study.

In this study, only the six GMI channels at 89 GHz and higher frequencies are employed to detect snow water signatures. Hereafter, these channels are referred to as 89V, 89H, 166V, 166H, 183±3V, and 183±7V channels, where the numbers denote the frequency in GHz, and the tailing letters indicate the polarization (H for horizontal and V for vertical polarizations).

Due to the discrepancy in spatial resolution between CPR and GMI pixels, we average all CPR pixels within a single GMI pixel. Additionally, we classify GMI pixels into clear–sky and cloudy conditions. A snow–rain separation scheme from *Sims and Liu* [2015] is also used to calculate the snowfall probability. Only GMI cloudy pixels with more than 50% snowfall probability as determined by the *Sims and Liu* [2015] scheme and passing the CPR precipitation threshold (–15 dBZ) are selected for creating the *a priori* database. The above processing methods are exactly adopted from the study of assessing GMI high frequency microwave channels in chapter 5.

6.2.2 Initial Hydrometeor Profiles

The initial snow water content profiles are derived from CPR radar reflectivities. The snow water content in the clutter layer (the lowest 1 km) is assumed to be the same as that in the first bin above the clutter layer. In this study, no attenuation correction is applied to CPR radar reflectivities. Instead, we will include this type of uncertainty in the background error covariance matrix for 1D–Var optimization.

The Z_e–SWC relation developed in chapter 5 is employed to convert radar reflectivity at 94 GHz to snow water content. In Fig. 6.2, we show this Z_e–SWC relation in blue line. The blue line is obtained by least-square fitting of all data points and can be expressed by

$$SWC=0.024Z_e^{0.75}, \tag{6.1}$$

where SWC is in g m^{-3}, and Z_e is in mm^6 m^{-3}. Other two Z_e–SWC relations are also shown in Fig. 6.2. The green line is computed for rosettes, sectors, and dendrites ($SWC=0.021Z_e^{0.76}$, (6.2)). The red line is computed for sectors and oblate aggregates ($SWC=0.015Z_e^{0.98}$, (6.3)). *Liu* [2008a] developed one Z_e–S relation (S: snowfall rate in mm h^{-1}) at 94 GHz using the same snowflake types and assumptions for green line and derived long–term snow cloud characteristics from CPR measurements using this relation. The results indicated that this Z_e–S relation generally gives similar ranges of the snowfall rates to those derived from in situ measurements [*Heymsfield et al*., 2016, 2017]. It is seen that two Z_e–SWC relations as shown by blue and green lines are very similar, which suggests that the Z_e–SWC relation in (6.1) is reasonable. As stated in *Meng et al.* [2017], larger snow rates will be produced when using dendrites than the other snowflake types. By comparing the two Z_e–SWC relations as shown by blue and red lines, it is seen that the assumption made for snowflake types will contribute some uncertainty in Z_e–SWC relation.

Cloud liquid water content profiles used in this study are derived from GMI retrieved

cloud liquid water path. The column total cloud liquid water is distributed evenly over a 1 km layer that has the highest relative humidity from 0.5 to 3 km. Different layer depths (0.5 to 1.5 km) have been tested. The impact of layer depths on the simulated brightness temperatures and the analyzed snow water content profiles is small.

6.2.3 Radiative Transfer Model

Brightness temperatures at GMI channel frequencies are calculated by the same radiative transfer model in chapter 5. In this model, the scattering cross sections of nonspherical snow particles are based on a look–up table of DDA modeling results [*Liu*, 2004]. This feature is critical in accurately simulating microwave brightness temperatures and their gradients with respect to frozen hydrometeors. The particle size distribution as shown in (4.1) is used in the radiative transfer model, in which the slope parameter (Λ) is calculated from snow water content (SWC) by the following two relations. The first relation is based on *Rutledge and Hobbs* [1983] and is expressed as

$$\Lambda = (\pi \times 1.6 \times 10^{12} / \mathrm{SWC})^{0.25} . \tag{6.4}$$

The second relation is derived using measurements of *Braham* [1990] as

$$\Lambda = 1122.242 \times \mathrm{SWC}^{-0.1282} . \tag{6.5}$$

For both relations, Λ is in m^{-1}, and SWC is in g m^{-3}. Hereafter, (6.4) and (6.5) will be referred to as Rutledge and Hobbs relation and Braham relation, respectively. N_0 is derived from Λ and SWC.

6.3. Developing Database Using 1D-Var Optimization

6.3.1 1D–Var Optimization Method

The core components of 1D–Var method include a radiative transfer model that

computes brightness temperatures and their gradients with respect to background geophysical parameters and a minimization module that solves a best estimate of state variables to optimally match background state variables and observed brightness temperatures. Assuming that background and observation errors are Gaussian, unbiased and uncorrelated, the departure between background state vector ($\mathbf{x}_0$) and observed brightness temperature vector ($\mathbf{y}_0$) is represented by a cost function:

$$J(\mathbf{x}) = (\mathbf{x} - \mathbf{x}_0)^T \mathbf{B}^{-1} (\mathbf{x} - \mathbf{x}_0) + (\mathbf{y}_0 - H(\mathbf{x}))^T \mathbf{R}^{-1} (\mathbf{y}_0 - H(\mathbf{x})), \tag{6.6}$$

where $\mathbf{x}$ is the control vector of state variables, $H(\mathbf{x})$ is the simulated brightness temperature vector based on state variables $\mathbf{x}$, $\mathbf{B}$ is the error covariance associated with $\mathbf{x}_0$, $\mathbf{R}$ is the error covariance associated with $\mathbf{y}_0$, and H represents the radiative transfer model. Besides the vertical profile of snow water content, $\mathbf{x}$ also includes the vertical profile of cloud liquid water, as radiation at GMI channels is partly affected by the emission and absorption of cloud liquid water. In our study, $\mathbf{y}_0$ contains observed brightness temperatures from six GMI channels at 89 GHz and higher frequencies. It is noted that $\mathbf{x}$ only includes the lowest 12.5 km (50 layers) of hydrometer profiles to reduce the dimension of $\mathbf{x}$, since neither snow nor liquid water exists above 12.5 km in our collected hydrometer profiles. All zero values in hydrometer profiles are replaced with a value of 10^{-5} g m^{-3} to avoid the zero derivatives of brightness temperatures as mentioned by *Moreau et al.* [2003]. The base ten logarithms of snow and liquid water contents are employed instead of themselves to avoid negative values during the minimization.

The solution $\mathbf{x}_{n+1}$ to the minimization of (6.6) at n+1th iteration is given by *Rogers* [1976]

$$\mathbf{x}_{n+1} = \mathbf{x}_0 + \mathbf{B}\mathbf{H}_n^T (\mathbf{H}_n \mathbf{B} \mathbf{H}_n^T + \mathbf{R})^{-1} [\mathbf{y}_0 - H(\mathbf{x}_n) - \mathbf{H}_n (\mathbf{x}_0 - \mathbf{x}_n)] \tag{6.7}$$

where $\mathbf{H}_n$ is the Jacobian matrix of observation vector. This form of solution is efficient when the

dimension of **B** is larger than that of **R** and therefore suitable for this study. The convergence criterion is adopted from the Satellite Application Facility for Numerical Weather Prediction (NWP SAF) 1D–Var package, i.e., the convergence is realized when the change in the cost function between two successive iterations is less than 1%. Detailed information about NWP SAF 1D–Var package can be found at: https://nwpsaf.eu/site/software/1d-var/documentation/.

The determination of background error covariance matrix **B** is described as follows. For snow water content, the uncertainty mainly comes from Z_e–SWC relation and CPR radar reflectivity. The uncertainty in Z_e–SWC relation is computed in this study as the standard deviation of $\log_{10}SWC_{avg}$ minus $\log_{10}SWC_{model}$ when varying particle shapes, yielding an uncertainty of about 0.2 in $\log_{10}SWC$. $\log_{10}SWC_{avg}$ is the logarithmic snow water content calculated by (6.1), and $\log_{10}SWC_{model}$ is the logarithmic snow water content calculated by (5.6). It is noticed that the radar reflectivity at 94 GHz may experience both the attenuation due to hydrometers and the multiple scattering in snow clouds [*Matrosov and Battaglia*, 2009]. The representativeness of CPR derived snow water content profile also yields an uncertainty (i.e., mismatch and discrepancy between two instruments). The uncertainty in CPR radar reflectivity from these sources is therefore assumed to be large and set to 1.5 dBZ for this study, which corresponds to an uncertainty of about 0.1 in $\log_{10}SWC$. For cloud liquid water content, the uncertainty is mainly associated with the vertical placement of liquid water, assuming that the GMI–retrieved cloud liquid water path is relatively accurate. Due to the lack of reliable dataset for quantifying the uncertainty in cloud liquid water content [*Duncan and Kummerow*, 2016], a constant uncertainty of 0.2 is assigned to the logarithmic cloud liquid water content, allowing less flexibility in the 1D–Var optimization. Only diagonal terms in the background error covariance matrix are used, assuming no correlation between different layers of hydrometeors

[*Liu*, 2005].

The observation error covariance matrix **R** is defined as a diagonal matrix, assuming no correlation between channels. The observation uncertainty is the sum of forward modeling error and instrument noise. The values of diagonal terms are mainly based on the standard deviations of observed minus simulated brightness temperatures at GMI channels under a snowfall condition. The standard deviations of brightness temperature departures represent an upper bound of observation uncertainty, since they also include the contribution from uncertainty in geophysical parameters, particularly hydrometeor profiles. A sensitivity test on brightness temperatures at GMI 89 GHz and higher frequencies to hydrometeor profiles is conducted. The 89 GHz channel shows the highest sensitivity among GMI channels to the variation in liquid water at low altitudes. On the other hand, GMI channels at 166 GHz are more sensitive to the variation in snow water than other channels. GMI channel at 183$\pm$3V GHz is weakly sensitive to the variation either in liquid or in snow water. GMI channel at 183$\pm$7V is sensitive to the variation in snow water at high altitudes, but merely detects the variation in liquid water at low altitudes. According to sensitivity test, the standard deviation of brightness temperature departures at each GMI channel under a snowfall condition is tuned to a smaller value to eliminate the contribution from uncertainty in geophysical parameters as done by *Boukabara et al.* [2011]. The uncertainty for GMI 89V, 89H, 166V, 166H, 183$\pm$3V and 183$\pm$7V channels represented by the tuned standard deviation of brightness temperature departures is 2.8 K, 7.4 K, 3.9 K, 5.0 K, 1.5 K and 2.6 K, respectively. In the future, the error correlations should be included to better represent the observation error covariance matrix, since the errors at 166 and 183$\pm$7 GHz are highly correlated. Assuming no correlation between channels will give too much weight to any solution that matches these channels at 166 and 183$\pm$7 GHz.

6.3.2 Case Studies

The 1D–Var method is first applied to four cases with distinctively different vertical distributions of snow water content. Fig. 6.3 illustrates how Z_e–SWC relations will affect the analyzed snow water content profiles. It is seen that the difference in snow water content between the two Z_e–SWC relations (6.1) and (6.3) is decreased, but still exists after 1D–Var optimization, implying that the uncertainty in Z_e–SWC relation will lead to some biases in the analyzed snow water content profiles. In the following, only (6.1) is used to convert Z_e to SWC. In Fig. 6.4, we show the four snow water content profiles from CPR initial estimate and analyses (1D–Var optimized estimates) using Λ–SWC relations of Braham and Rutledge and Hobbs. In order to assess the impact of 166 GHz channels on 1D–Var optimization, a channel subset excluding 166 GHz is also used. For the two cases shown in top panels, the values of snow water content in the lower and middle troposphere are decreased after the 1D–Var optimization. The optimized snow water content profiles are similar using the two different Λ–SWC relations. The decrements in snow water content through 1D–Var optimization are only slightly smaller using the subset of channels. For the two cases shown in bottom panels, the values of snow water content throughout the troposphere below 6 km are increased after the 1D–Var optimization. The increments in snow water content using the Braham relation is somewhat more pronounced than that using the Rutledge and Hobbs relation. Without 166 GHz channels, the increments in snow water content are much smaller in the middle troposphere. It is seen that the adjustments on snow water content through the 1D–Var optimization are quite substantial, especially for the cases shown in bottom panels. For the case in the bottom left panel, the snow water content near 4 km is only about 0.2 g m^{-3} before the 1D–Var optimization, but it reaches above 0.3 g m^{-3} after the 1D–Var optimization, representing an increase of more than 50 % from the original value.

Next, we show a snow precipitation case on March 11, 2015. The vertical cross sections of snow water content from CPR initial estimate and analyses using Braham and Rutledge and Hobbs relations are displayed in Fig. 6.5. Similarly, the results using a channel subset excluding 166 GHz are also presented. From the CPR estimate, two adjacent cells near 52°N are found in the lower troposphere, extending from the ground to an altitude of about 3 km. Some small cells are also found in the middle troposphere at about 4 km, i.e., a cell near 53°N. The values of snow water content reach about 0.2 g m^{-3} inside the two snow cells near 52°N and about 0.25 g m^{-3} for the cell near 53°N. After applying the 1D–Var optimization, the values of snow water content for two adjacent cells near the ground are increased to about 0.35 g m^{-3} using Braham relation and 0.3 g m^{-3} using Rutledge and Hobbs relation. The values of snow water content inside the cell in the middle troposphere near 53°N are increased substantially and can be as large as 0.45 g m^{-3} using either Λ–SWC relation. Another noticeable feature is that the intensities for the two small snow cells at about 4 km near 51.5°N and 54.5°N are largely reduced, while the intensity of a snow cell at 5 km near 50.5°N is enhanced with snow water content values reaching larger than 0.25 g m^{-3}. Comparing (b) and (d) in Fig. 6.5, it is seen that the snow water content adjustments near 52°N and 53°N are less pronounced without 166 GHz channels, implying that 166 GHz channels provide further information on columnar snow water.

Brightness temperatures at different GMI frequencies are sensitive to snow signals coming from different atmospheric volumes. Brightness temperatures at 166 GHz are the most sensitive to snow water in the atmospheric column. Large differences between observed and simulated GMI brightness temperatures at 166 GHz are found when the adjustments are substantial on snow water content in the vertical column through the 1D–Var optimization as occurred for two snow cells near 52°N. Greater adjustments on snow water content at altitudes

higher than 3 km are usually associated with the larger differences between observed and simulated GMI brightness temperatures at 183±7 GHz, since this channel is sensitive to snow particle scattering at high altitudes. The GMI brightness temperature difference at 183±3 GHz is usually smaller than that at 183±7 GHz, as this channel is more sensitive to water vapor, but less sensitive to snow water. Brightness temperatures at 89 GHz contain less snow signatures and are more sensitive to surface emission compared to those at higher frequencies. Nevertheless, the 89 GHz GMI channels provide necessary physical constraints on liquid water and surface emission.

6.3.3 Statistics of the Constructed *a priori* Database

To create the *a priori* database, the 1D–Var method is applied to all qualified GMI pixels and their associated hydrometeor profiles as described in Section 2. Since two Λ–SWC relations produce similar results, only Braham relation is discussed hereafter. After the 1D–Var optimization, the simulated brightness temperatures are expected to be more consistent with those observed ones. In Fig. 6.6, we compare the observed and simulated brightness temperatures for GMI channels at 89 GHz and higher frequencies with snow water content profiles of CPR initial estimate and analysis as input to radiative transfer model. It is seen that the observed brightness temperatures are generally consistent with the simulated ones even before the 1D–Var optimization. A cold bias (observations minus simulations) is found for 89V channel before the 1D–Var optimization. This cold bias is partly reduced after the 1D–Var optimization, mainly for those observed brightness temperatures lower than 220 K. The adjustment to 89H GHz channel through the 1D–Var optimization is small, because this channel is less sensitive to the variation in snow water and easily affected by the variation in surface emissivity. A warm bias for the observed brightness temperatures below 260 K is found at 166V channel before the 1D–Var optimization. This warm bias is effectively removed after the 1D–

Var optimization, indicating a good agreement between observed and simulated brightness temperatures. The scatter of 166H brightness temperatures is also decreased by adjusting the biased brightness temperatures through the 1D–Var optimization. A similar warm bias appears at 183±3V and 183±7V channels before the 1D–Var optimization, which is removed by the 1D–Var optimization. The large adjustment on 183±7V channel indicates its high sensitivity to the variation in snow water compared to 183±3V channel. It is worth mentioning that GMI brightness temperatures are expected to adjust those CPR snow water content profiles originally generated by attenuated radar reflectivities in the 1D–Var optimization. Some simulated brightness temperatures are associated with a cold bias at 166V and 183±7V channels before the 1D–Var optimization. Those simulated brightness temperatures are likely calculated from snow water content profiles with attenuated radar reflectivities. A cold bias for those simulated brightness temperatures at 166V and 183±7V channels is then removed by the 1D–Var optimization, implying that the optimization using the GMI brightness temperatures partly offsets the impact of attenuation to the CPR radar reflectivities. Conversely, a warm bias observed at 166 or 183 GHz manifests physical mismatch between brightness temperatures and hydrometeor profiles due to reasons other than attenuation. As explained in chapter 4, this warm bias is associated with shallow cells where the cloud liquid water may contribute significantly to the observed brightness temperatures. The errors in cloud liquid water profiles lead to the large biases in simulated brightness temperatures for those channels sensitive to surface emission. The optimization procedure acts to bring a physical consistency between the hydrometeor profiles and the observed brightness temperatures in the GMI pixel–covered volume.

The standard deviations of the difference between the observed and simulated brightness temperatures can be employed to examine the convergence of the 1D–Var

optimization. In Fig. 6.7, we show the standard deviations of observed minus simulated brightness temperatures for GMI channels at 89 GHz and higher frequencies, grouped for data with $\Delta T_b^{166V} > 1$ K and $\Delta T_b^{166V} < 1$ K, with snow water content profiles of CPR initial estimate and analysis as input to radiative transfer model. ΔT_b^{166V} is the brightness temperature difference with and without including snow water in the radiative transfer model. This quantity reflects the effect of column snow water, i.e., a greater ΔT_b^{166V} responding to a larger column snow water amount. It is found that the decrease of the standard deviations at 166 and 183 GHz after 1D–Var optimization are significant for the group with $\Delta T_b^{166V} > 1$ K and negligible for the group with $\Delta T_b^{166V} < 1$ K, implying that the large adjustments on snow water through 1D–Var optimization occur for those profiles with large column snow water. For both groups, it is seen that the standard deviations of the brightness temperature difference are decreased to a similar magnitude of the observation uncertainty defined in the observation error covariance matrix **R**, indicating that the variational optimization is effective.

This constructed database includes snow water content profiles and corresponding simulated brightness temperatures at GMI channels, together with several other geophysical parameters (cloud liquid water profiles, total precipitable water, and 2–m air temperature). The number of converged snow water content profiles is 18340. Less than 0.5 % of the collected snow water content profiles failed to pass the convergence test. These profiles are mostly for very light snowfall conditions.

Since two parameters, total precipitable water and 2–m air temperature, are closely related to snow formation, we present the frequency distributions of these profiles in terms of total precipitable water and 2–m air temperature in Fig. 6.8. More than 50 % the profiles are

associated with total precipitable water in the range from 4 to 8 kg m^{-2}. More than 70 % of the profiles are associated with 2–m air temperature in the range from 271 to 275 K.

The geolocations of snow water content profiles in this database are shown in Fig. 6.9, in which the number of analyzed snow water content profiles within 5°×5° boxes is displayed. The majority of the snow water content profiles are distributed above 50° latitude. In the northern hemisphere, snow water content profiles are concentrated within longitude ranges from 30°W to 60°W and 150°E to 180°E. In the southern hemisphere, the longitudinal distribution of snow water content profiles is relatively homogenous compared to the northern hemisphere. The distribution pattern of profiles in this figure is consistent with the global map of snowfall frequency shown by *Liu* [2008a], suggesting that this optimized database has a good representativeness of snowfall occurrence. Additionally, the contoured frequency by altitude diagrams for the analyzed snow water content profiles is shown in Fig. 6.10. It is found that snow water is generally located below 10 km. Most snow water content values are smaller than 0.1 g m^{-3} and generally decrease with altitudes.

6.4. Applying Database to Bayesian Retrieval

After creating this *a priori* database, it is necessary to assess the benefits of this optimized database on snow water retrievals. The retrieval results from this database are compared to those from another *a priori* database that consists of initial snow water content profiles and simulated GMI brightness temperatures without 1D–Var optimization.

6.4.1 Bayesian Retrieval Method

This retrieval method based on Bayes' theorem has been described in detail by *Olson et al.* [1996] and *Evans et al.* [2002]. It uses a database that consists of precalculated brightness temperatures and associated geophysical parameters. Given a vector of observed brightness

temperature $\mathbf{y}_0$, the retrieved state vector $\mathbf{x}_{\mathrm{rt}}$ can be expressed as:

$$\mathbf{x}_{\mathrm{rt}} = \sum_i \mathbf{x}_i \exp[-0.5\chi_i^2] / \sum_i \exp[-0.5\chi_i^2] \tag{6.8}$$

$$\chi_i^2 = (\mathbf{y}_0 - H(\mathbf{x}_i))^T \mathbf{R}^{-1} (\mathbf{y}_0 - H(\mathbf{x}_i)) \tag{6.9}$$

where $\mathbf{x}_i$ is the ith state vector in an *a priori* database, and χ_i^2 measures the difference between observed and simulated brightness temperature vectors. The weighting factor for $\mathbf{x}_i$ increases with the decrease of χ_i^2. It is seen that χ_i^2 is equivalent to the second term on the right-hand side of cost function $J(\mathbf{x})$ in (6.6). The observation error covariance matrix $\mathbf{R}$ here is defined in the same way as in $J(\mathbf{x})$, assuming no correlation between channels. After constructing the *a priori* database for GMI snow water retrievals over ocean, the Bayesian retrieval method is utilized to test the performance of this constructed database on retrieving snow water content profiles from GMI brightness temperatures.

One issue in using this *a priori* database is that it does not contain the correct information on the ratio of precipitating versus non–precipitating profiles, since this *a priori* database only contain snowfall cases. This issue has also been described by other studies employing Bayesian retrieval method [*Kummerow et al.*, 2011, 2015]. Without non–precipitating cases in the database, the Bayesian retrieval method always has a tendency to force the retrieved geophysical parameters towards a snowfall condition and thus introduces a positive retrieval bias. One solution is to distinguish precipitating scenes from non–precipitating scenes using an empirical screening algorithm and only perform retrievals to precipitating scenes. An alternative approach is employed in this study and described as follows. A GMI pixel is firstly determined whether it is a "cold" sample or not using a snowfall probability parameterization [*Sims and Liu*, 2015] described in section 2.2. A cold sample is defined as an atmospheric condition that has a

snowfall probability larger than 50% by the Sims and Liu algorithm. The Bayesian retrieval method is then applied to a cold sample using an extended *a priori* database. This extended *a priori* database includes all analyzed snowfall profiles and all "cold" non–precipitating profiles that failed to pass the CPR precipitation threshold. The non–precipitating profiles can further classified into clear–sky and cloudy profiles. The total number of snowfall and non–precipitating profiles is 38749.

The occurrence frequency distributions of analyzed surface snow water content, retrieved surface snow water content using all profiles, retrieved surface snow water content using clear–sky and snowfall profiles, and retrieved surface snow water content only using snowfall profiles are presented in Fig. 6.11. All analyzed snowfall profiles in the database are included for this figure. It is seen that the distribution of occurrence frequency is shifted towards larger snow water content values if the *a priori* database only includes snowfall profiles. After including clear–sky profiles in the database, this shift of occurrence frequency distribution is alleviated with a lower peak of occurrence frequency. When using the extended database that contains all snowfall and non–precipitating profiles, the occurrence frequency distribution of snow water content is similar to that of analyzed snow water content, indicating the success of this approach for solving the incompleteness issue in the *a priori* database.

6.4.2 Retrieval Results

The Bayesian retrieval method is first applied to two cases. Two parameters, total precipitable water and 2–m air temperature, are used to add physical constraints on selecting profiles in the database. The extended database is split into two subsets according to a threshold, which is 5.5 kg m^{-2} for total precipitable water and 273 K for 2–m air temperature. The thresholds are based on the relative frequency distributions of total precipitable water and 2–m

air temperature in Fig. 6.8 so that two subsets contain nearly equal number of snow water profiles. The retrieval method only employs one subset for a GMI pixel based on its associated values of total precipitable water or 2–m air temperature. Hereafter, we use "moisture constraint" to refer to total precipitable water constraint, and "temperature constraint" to refer to 2–m air temperature constraint. Fig. 6.12 shows the vertical cross sections of (a) analyzed snow water content, retrieved snow water content using (b) full database, (c) subsets of the database with moisture constraint, (d) subsets of the database with temperature constraint, (e) CPR initial snow water content, and (f) retrieved snow water content using CPR initial estimate as database for a case on March 11, 2015. It is seen that a snow cell at about 4 km near 53.2°N observed in the analyzed snow water content profiles is well captured by the retrieved snow water content profiles using the 1D–Var optimized database. The width of this cell from the GMI retrieved snow water content with moisture constraint seems to be closer to that from CPR analyzed snow water content profiles. Another observed snow cell at about 2 km near 53.5°N is also retrieved from the GMI measurements using the 1D–Var optimized database. In contrast, a snow cell with snow water content less than 0.25 g m^{-3} at about 4 km near 53.2°N is found in CPR initial snow water content profiles, while a snow cell with snow water content larger than 0.35 g m^{-3} at about 2 km for this same location is observed in the retrieved snow water content profiles using database without the 1D–Var optimization, suggesting an inconsistency between the initial and the retrieved snow water content profiles.

Fig. 6.13 shows another case on December 05, 2014. It is seen that a snow cell with snow water content larger than 0.3 g m^{-3} at about 3.5 km near 64.5°N is observed in the analyzed and the retrieved snow water content profiles using the 1D–Var optimized database. The GMI retrieved snow water content with moisture constraint gives the best cell structure with respect to

that from the CPR analyzed snow water content profiles. On the other hand, a surface snow cell near 64.2°N captured by the analyzed snow water content profiles is missed by the retrieved snow water content profiles regardless database used in the retrieval. The retrieved snow water content profiles using database without 1D–Var optimization missed the two snow cells near 64.2°N and 64.7°N, but produced a snow cell near 64.5°N at a lower altitude with much larger snow water content than those in the initial snow water content profiles. It is clear that without maximizing the physical consistency between the CPR snow water content profiles and the GMI observed brightness temperatures through 1D–Var optimization, the discrepancy between the initial and the retrieved snow water content profiles are much more severe than in the case with 1D–Var optimization. After adding the moisture constraint, the retrieved snow water content profiles using 1D–Var optimized database are closer to the analyzed snow water content profiles, indicating the benefits of physical constraints on snow water retrievals.

The next step is to investigate the suitability of this optimized *a priori* database in global snow water retrievals. The global mean surface snow water content distribution over ocean for the entire year of 2015 is retrieved from CPR radar reflectivities using Z_e–SWC relation of (8a) and from GMI brightness temperatures using the optimized *a priori* database, and shown in Figs. 6.14 and 6.15 for northern and southern hemispheres, respectively. In Fig. 6.14, we show the northern hemisphere mean distributions of surface (1 km above sea level) snow water content within 5°×5° boxes over ocean retrieved from (a) CPR radar reflectivities, and GMI brightness temperatures using (b) full database, (c) subsets of the database with moisture constraint, (d) subsets of the database with temperature constraint, and (e) CPR initial snow water content profiles as database. As shown in the CPR retrievals, there are two regions with large values of mean surface snow water content: one from 30°W to 60°W with values larger

than 8 mg m^{-3}, and another from 150°E to180°E with values larger than 4 mg m^{-3}. This feature is well captured by all the GMI retrieved surface snow water contents. In southern hemisphere (Fig. 6.15), the CPR retrieved surface snow water content is evenly distributed over east longitudes, leading to mean surface snow water content values larger than 10 mg m^{-3} south of 60°S. All the GMI retrievals catch this asymmetric distribution and have mean surface snow water content values larger than 7 mg m^{-3} over east longitudes south of 60°S. The correlation coefficients between the CPR and all the GMI retrieved mean surface snow water contents within 5°×5° boxes are about 0.93.

In order to quantify the accuracy of the GMI retrievals, in Figs. 6.16 and 6.17 we show the differences of mean surface snow water contents between those retrieved from CPR radar reflectivities and those retrieved from GMI brightness temperatures using (a) full database, (b) subsets of the database with moisture constraint, (c) subsets of the database with temperature constraint, and (d) CPR initial snow water content profiles as database. Differences seem to be large in the regions where snow water contents themselves are also large. For the northern hemisphere, a positive difference (CPR minus GMI retrievals) up to 4 mg m^{-3} are seen in the regions within 30°W to 60°W for all GMI retrievals. A smaller positive difference of about 2 mg m^{-3} can be seen in another region within 150°E to 180°E. For southern hemisphere, the region over east longitudes is mainly characterized by a positive difference, while the region from 0°W to 60°W is associated with a negative difference. The GMI retrievals with 1D–Var optimized full database resulted in a smaller positive difference over east longitudes and a slightly larger negative difference within 0°W to 60°W than those retrievals using the database without 1D–Var optimization. Additionally, the GMI retrievals using optimized database with the moisture constraint resulted in the smallest positive difference over east longitudes and the largest

negative difference within 0°W to 60°W. On the other hand, the GMI retrievals using optimized database with temperature constraint yields the largest positive differences over east longitudes and the smallest negative differences within 0°W to 60°W. In terms of global mean differences, the GMI retrieved surface snow water content is closer to the CPR retrievals when using the 1D–Var optimized database compared to those retrieved from the database without 1D–Var optimization (0.46 vs. 0.67 mg m^{-3}). The moisture constraint further improves the GMI retrievals (0.19 mg m^{-3}), but the temperature constraint seems to have little or even negative effect on the GMI retrievals (0.59 gm m^{-3}).

6.5 Conclusions for Passive Microwave Snowfall Retrieval Algorithm

A physically optimized *a priori* database is constructed which can be used in a Bayesian algorithm to retrieve snow water over ocean using passive microwave observations at 89 GHz and higher frequencies. The optimization is achieved by minimizing the inconsistency between hydrometeor profiles and observed brightness temperatures with prior information constraint through a 1D–Var scheme. The initial snow water content profiles are derived from CPR radar observations using a Z_e–SWC relation rather than results of cloud resolving models. The simulated brightness temperatures at GMI channels and their gradients with respect to hydrometeors are computed by a radiative transfer model, in which the single scattering properties of nonspherical snowflakes are calculated using DDA method. The 1D–Var optimization is firstly examined by applying to individual vertical profiles of snow water content and a snowfall case with several hundreds of kilometers in horizontal extent. It is shown that the adjustments to snow water content profiles through 1D–Var optimization are substantial.

Two relations between slope parameter in particle size distribution and snow water content are employed in the radiative transfer model. The results obtained from the two different

relations are quite similar. Therefore, there is no attempt made in this study to investigate how particle size distributions impact the outcome of the database. After proper data processing, all snow water content profiles with collocated GMI and CloudSat CPR parameters during March 2014 through June 2016 are optimized using the 1D–Var method. It is found that the large adjustments on snow water are associated with those profiles with large snow water content values. The standard deviations of the observed minus simulated brightness temperatures are decreased to a similar magnitude of observation uncertainty as defined in observation error covariance matrix after the 1D–Var optimization, indicating the effectiveness of this variational method. In the database, most snow water content profiles are associated with total precipitable water in the range of 4 to 8 kg m^{-2} and 2–m air temperature in the range of 271 to 275 K. Snow water content profiles are distributed more evenly along longitudes in the southern hemisphere than in the northern hemisphere where snowfall cases are closely associated with storm tracks. The majority of snow water content values are smaller than 0.1 g m^{-3} and tend to decrease gradually with increasing altitudes.

A Bayesian retrieval algorithm is applied to retrieve snow water content profiles from GMI measurements using the optimized *a priori* database. In order to solve the incompleteness issue (i.e., lack of non–precipitating profiles) in this *a priori* database, a simple approach of adding non–precipitating profiles in the database is used, and it proved to be successful. The impact of using precipitable water and 2-m air temperature to subset the database is also evaluated. From two case studies, it is shown that by improving the physical consistency between snow water content profiles and observed brightness temperatures through the 1D–Var optimization, the vertical distribution of the GMI retrieved snow water content profiles is closer to that of the CPR analyzed ones. Global mean distributions of surface snow water content over

ocean is retrieved for one year (2015) using CPR radar reflectivities and GMI brightness temperatures. By comparing the CPR and the GMI retrievals, it is found that the GMI retrieved surface snow water contents have a smaller bias with respect to the CPR retrievals when using the optimized database than when using the CPR initial estimate as database. Additionally, the use of precipitable water to subset the database has a positive impact on the GMI retrievals, while the use of 2–m air temperature to subset the database produces little or negative impact on the GMI retrievals.

This study demonstrated the plausibility for developing an *a priori* database for snow water retrievals using high frequency microwave observations by a variational method. The results also imply that using physical parameters to subset the database has a positive impact on snow water retrievals given that the number of datum points in the full database is sufficiently large. Additionally, the variational method used in this study is highly flexible and therefore can be applied to other precipitation retrieval algorithms. In particular, a large set of assumptions has been used in our variational method, such as particle size distributions and error characteristics. These assumptions, while requiring further examination, can be used in future variational retrieval algorithms. The future work includes the inter–comparison of long–term snow water retrievals over ocean using the optimized database and independent data sources (i.e., GPM combined radar–radiometer product).

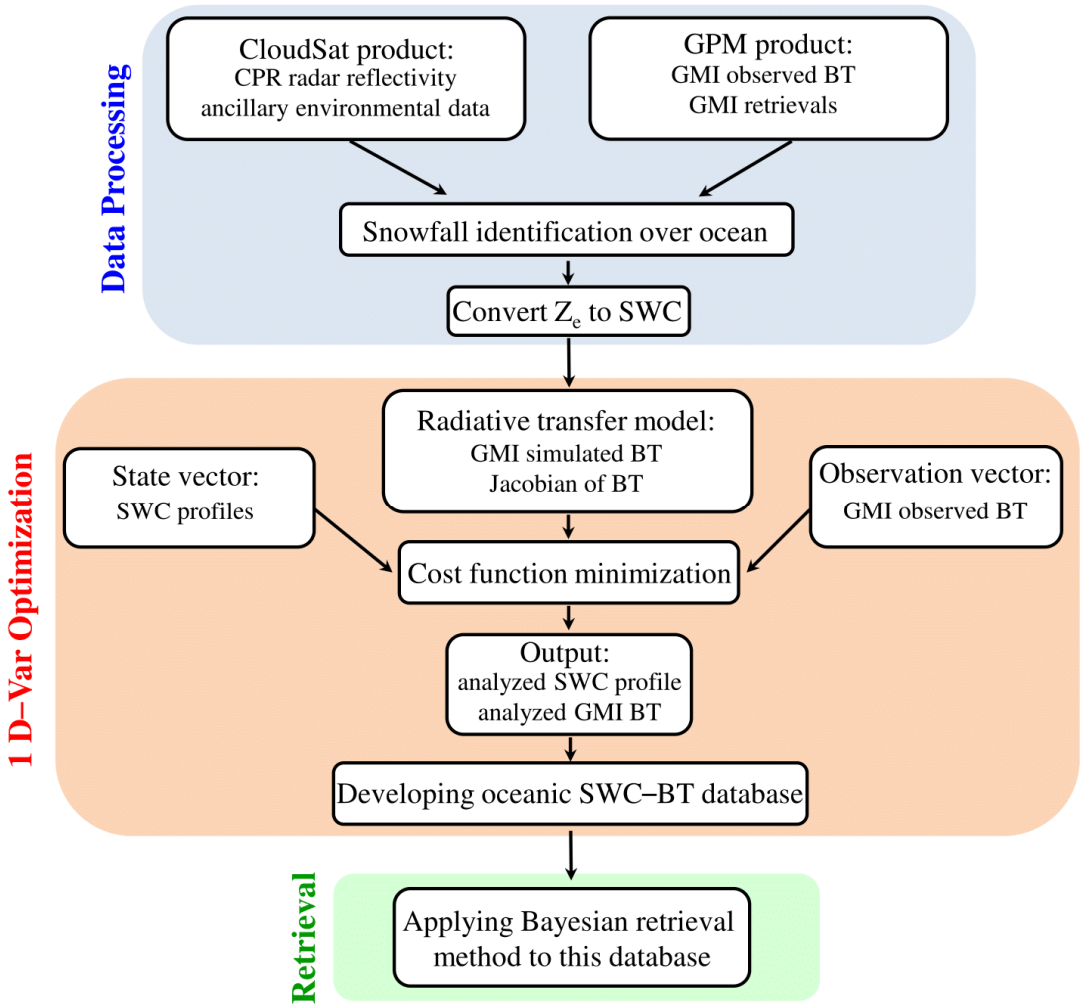

Fig. 6.1. Flowchart for developing an *a priori* database for passive microwave snowfall retrievals over ocean using 1D–Var optimization method. SWC: snow water content. BT: brightness temperature.

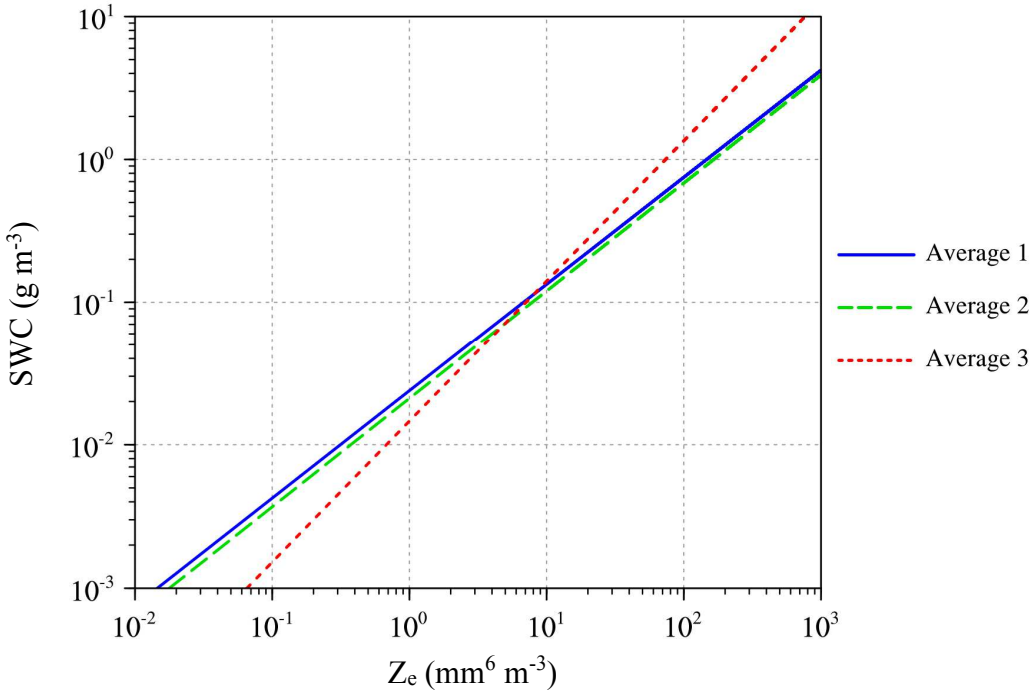

Fig. 6.2. Z_e–SWC relations for average 1 (sector, dendrite, and aggregate), average 2 (rosettes, sector, and dendrite), and average 3 (sector and aggregate).

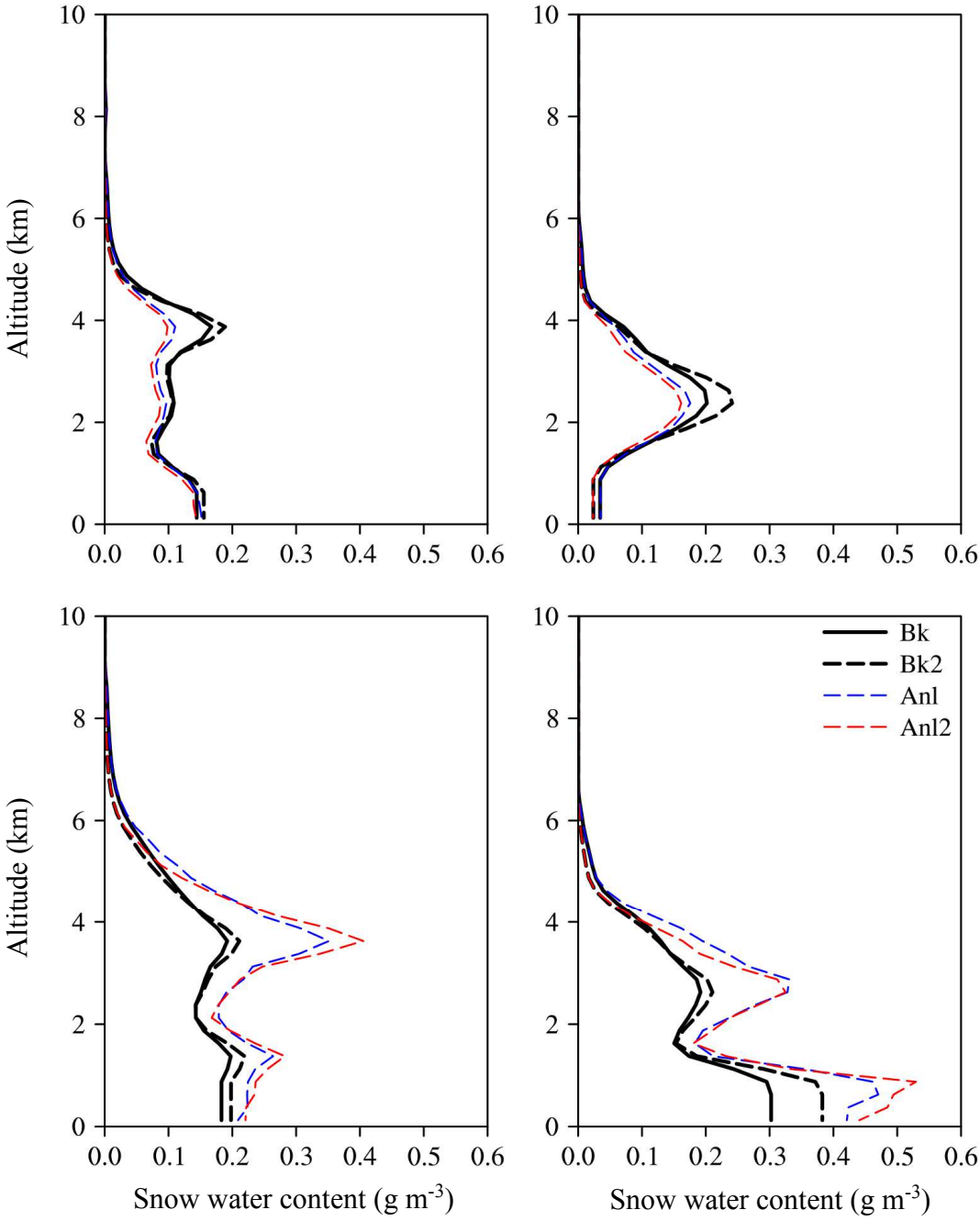

Fig. 6.3. Four vertical profiles of snow water content from CPR initial estimate using Z_e–SWC relation in (6.1) (black solid curve), CPR initial estimate using Z_e–SWC relation in (6.3) (black dash curve), analysis using Z_e–SWC relation in (6.1) (blue curve), and analysis using Z_e–SWC relation in (6.3) (red curve). Only Braham relation is employed.

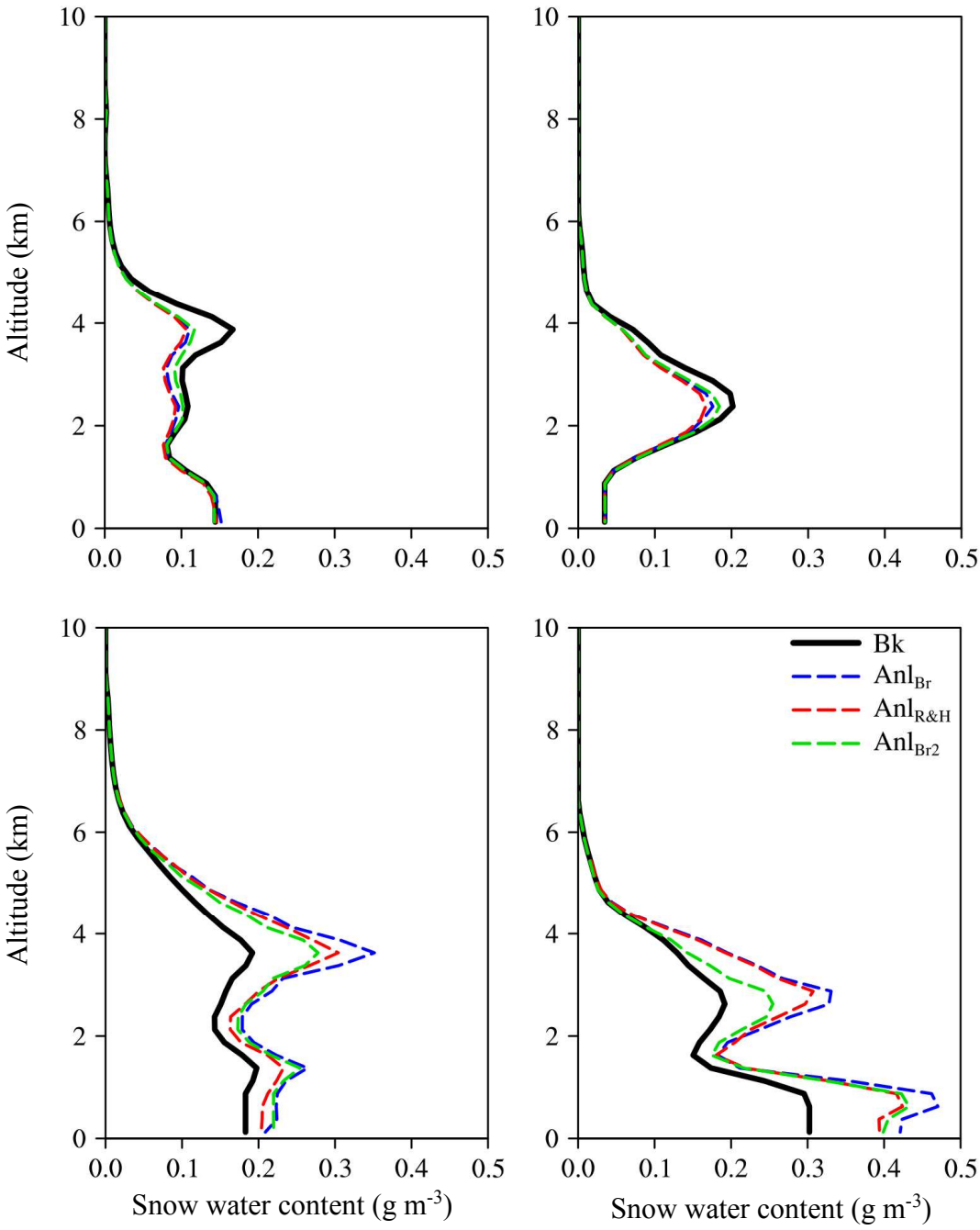

Fig. 6.4. Four vertical profiles of snow water content from CPR initial estimate (black curve), analysis using Braham relation (blue curve), analysis using Rutledge and Hobbs relation (red curve), and analysis using Braham relation with a channel subset excluding 166 GHz (green curve).

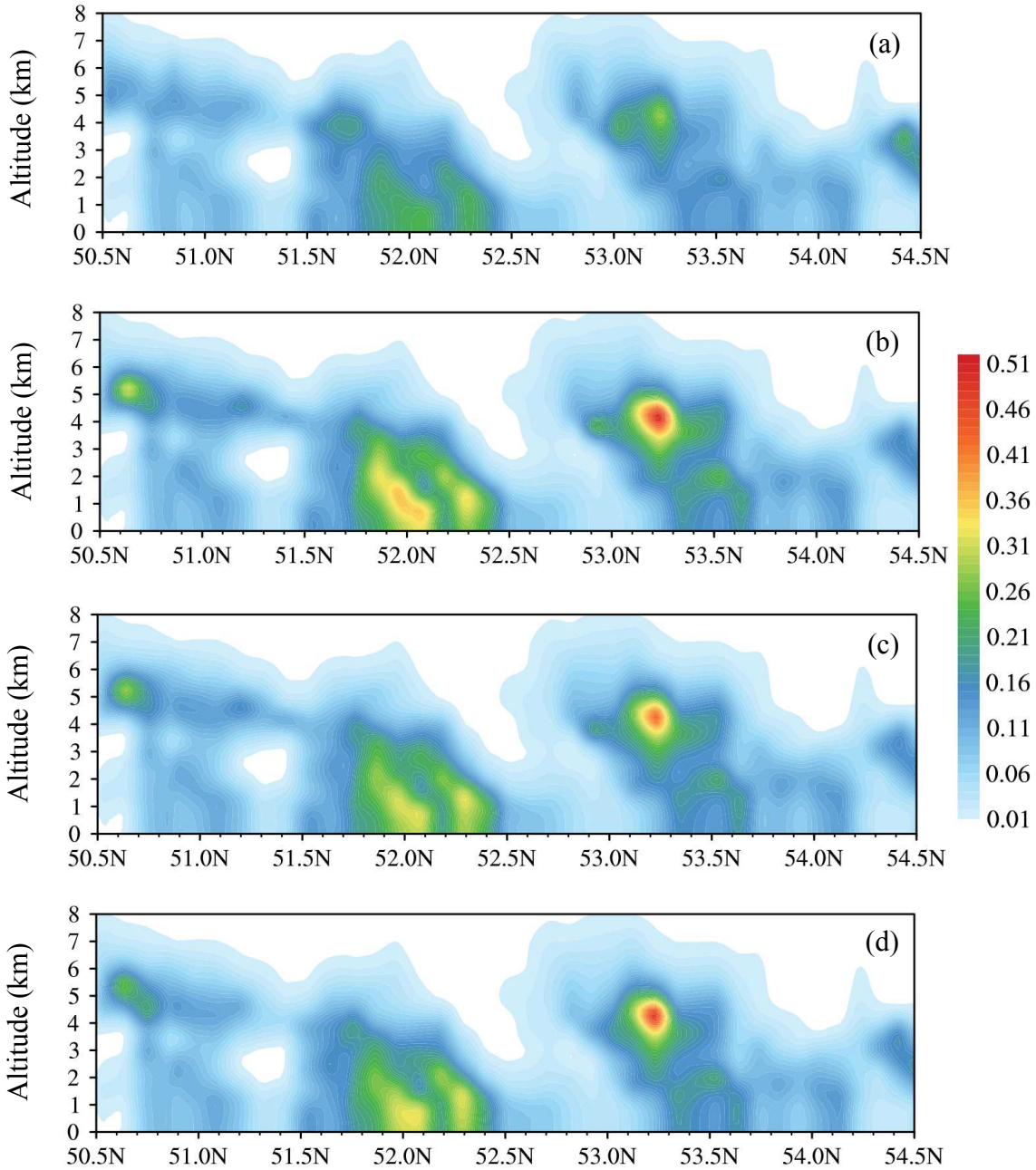

Fig. 6.5. Vertical cross sections of snow water content (unit: g m^{-3}) from (a) CPR initial estimate, (b) analysis using Braham relation, (c) analysis using Rutledge and Hobbs relation, and (d) analysis using Braham relation with a channel subset excluding 166 GHz for a case on March 11, 2015.

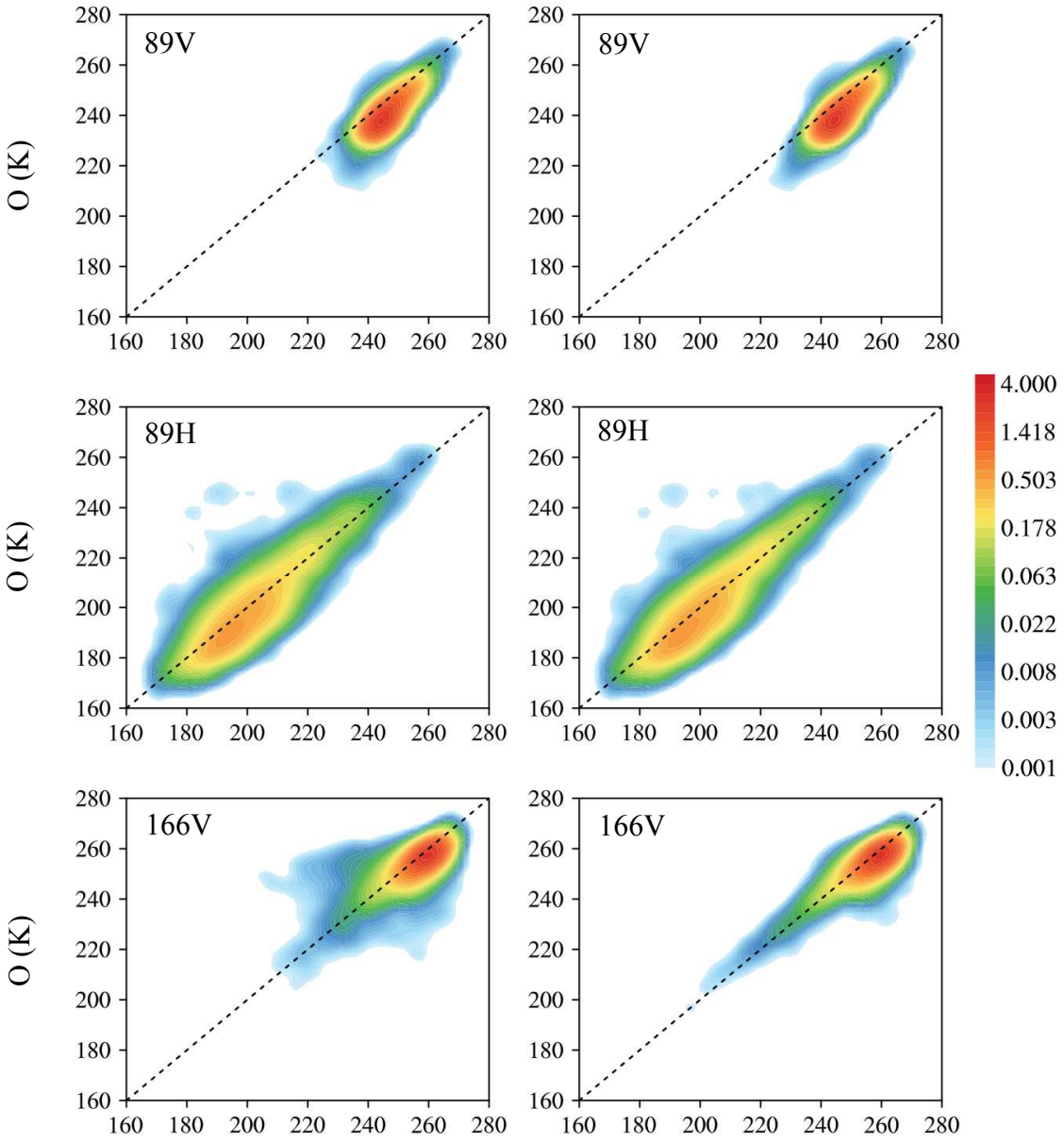

Fig. 6.6. Relations between observed (O) and simulated (B or A) brightness temperatures for GMI channels at 89 GHz and higher frequencies with snow water content profiles of CPR initial estimate (left column) and analysis (right column) as input to radiative transfer model. The shading represents the occurrence frequency (unit: %).

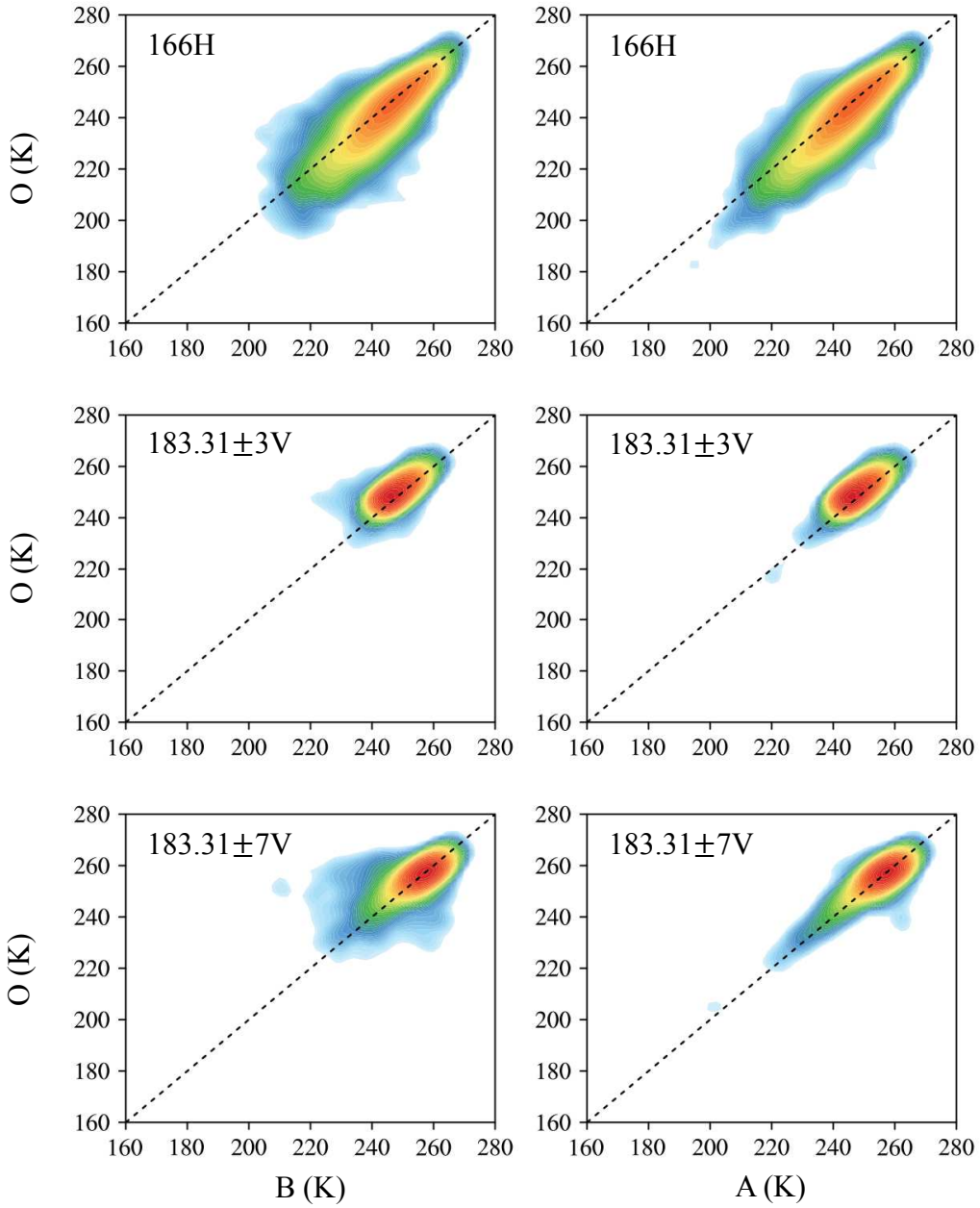

Fig. 6.6. Continued

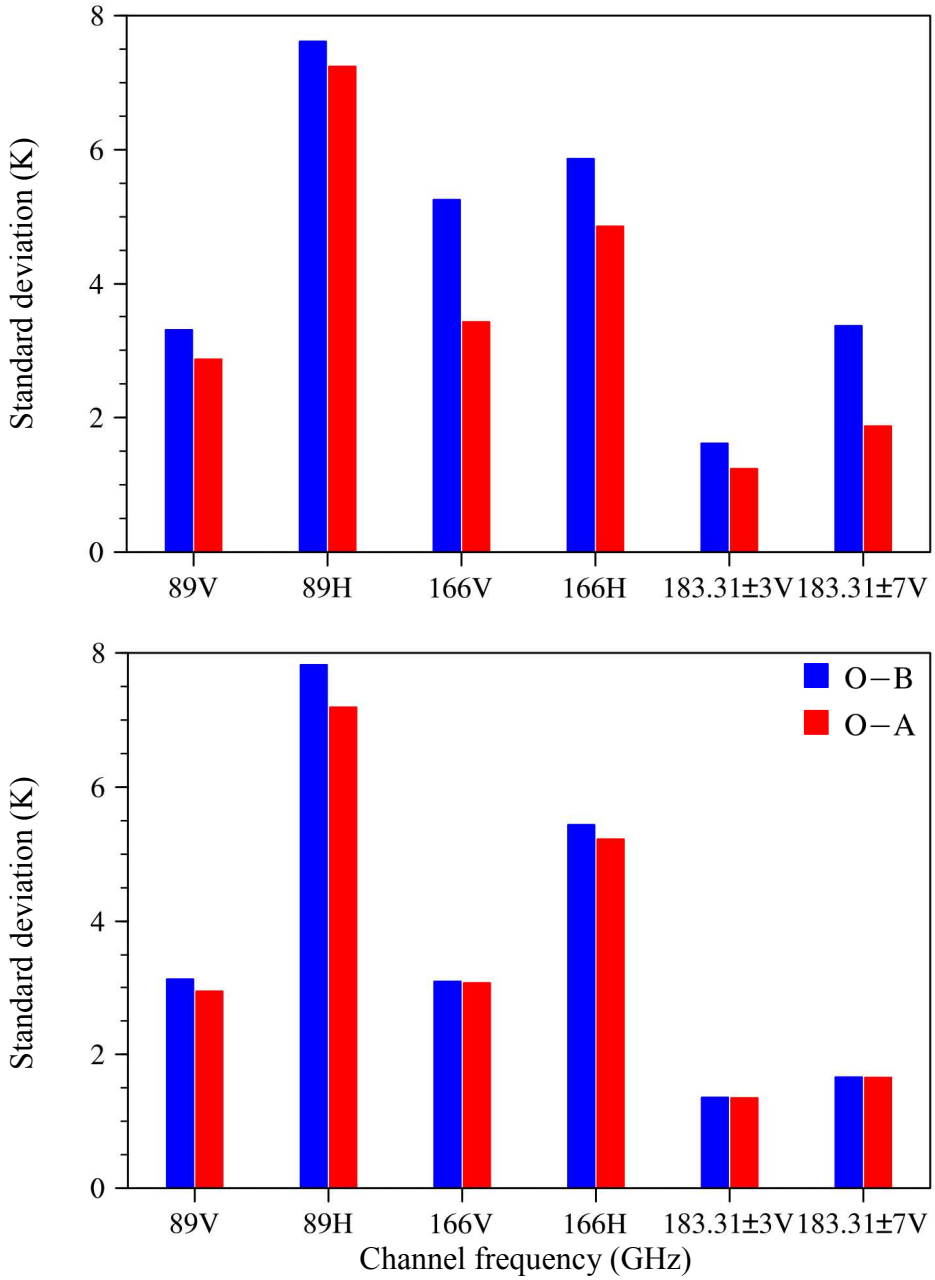

Fig. 6.7. Standard deviations of observed (O) minus simulated (B or A) brightness temperature for GMI channels at 89 GHz and higher frequencies, grouped for data with $\Delta T_b^{166V} > 1$ K (top panel) and $\Delta T_b^{166V} < 1$ K (bottom panel), with snow water content profiles of CPR initial estimate (blue) and analysis (red) as input to radiative transfer model.

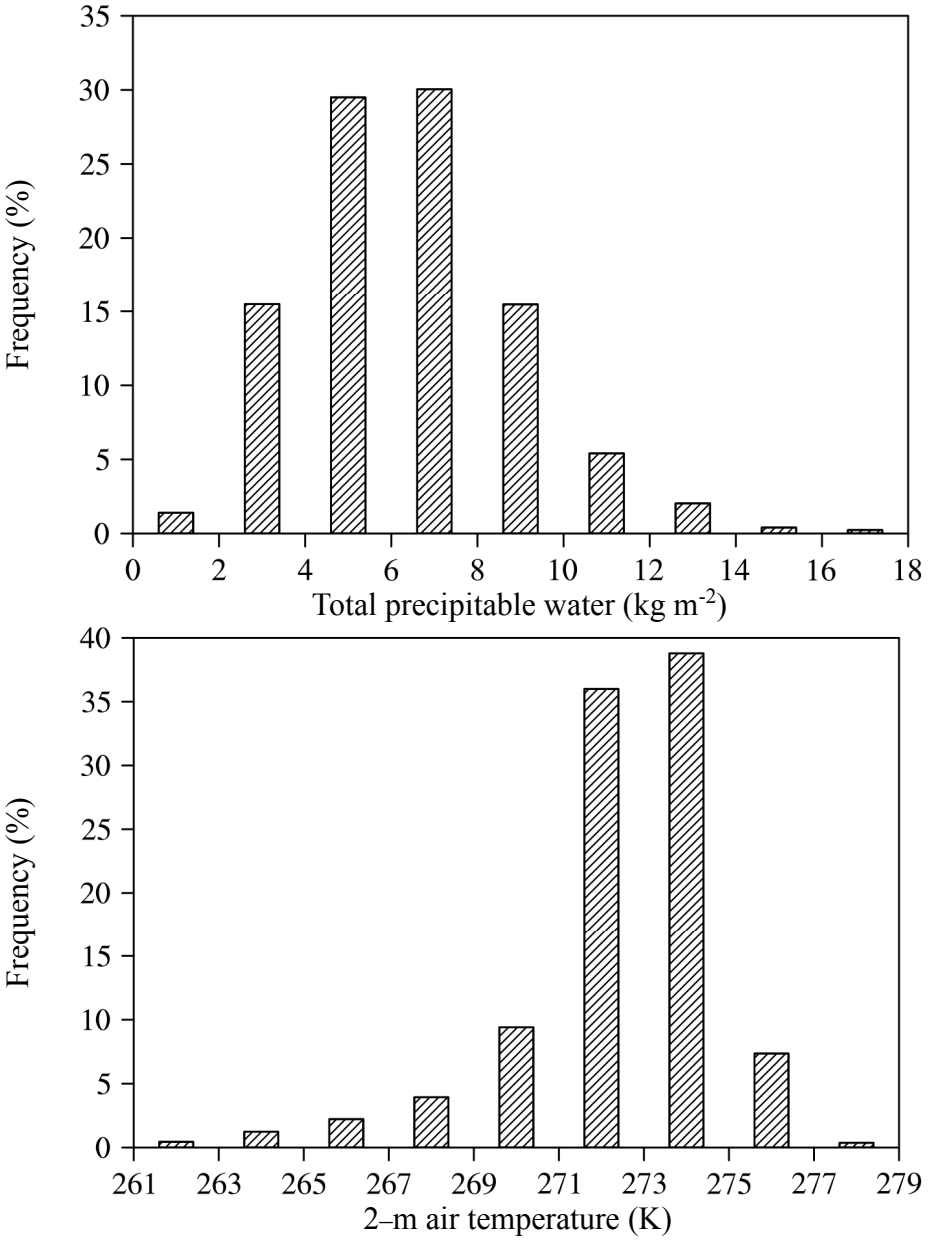

Fig. 6.8. Frequency distributions of analyzed snow water content profiles in terms of total precipitable water (top panel) and 2–m air temperature (bottom panel).

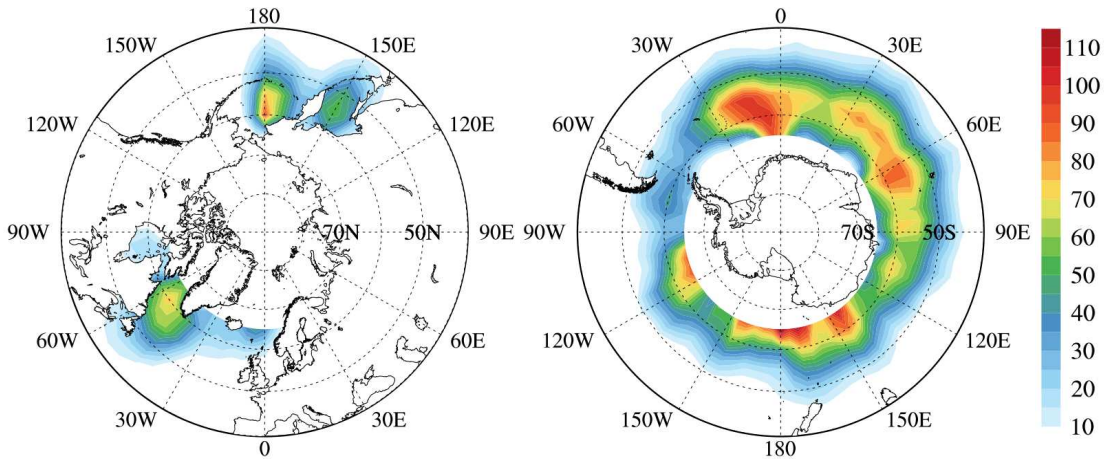

Fig. 6.9. Number of analyzed snow water content profiles within 5°×5° boxes.

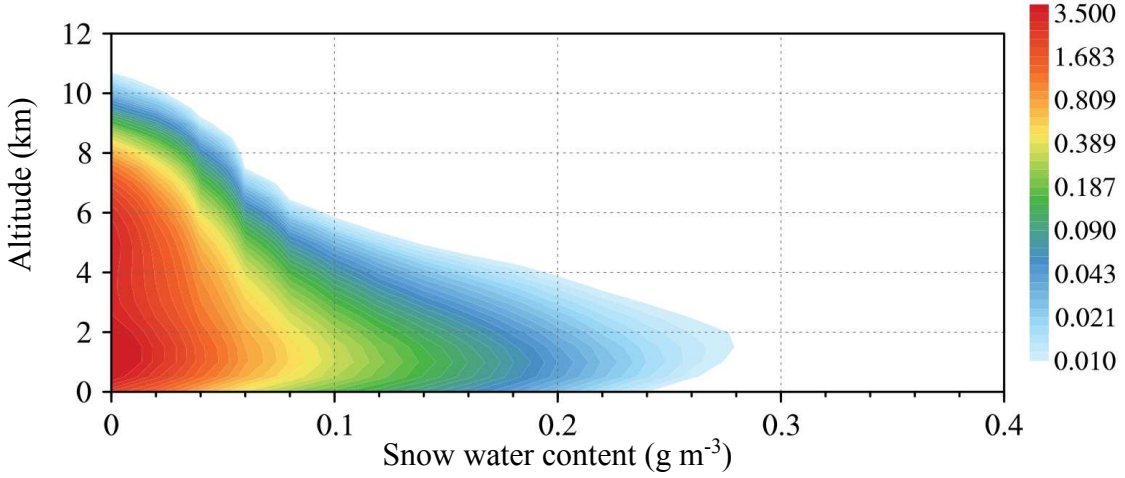

Fig. 6.10. Contoured frequency by altitude diagrams (unit: %) for analyzed snow water content profiles.

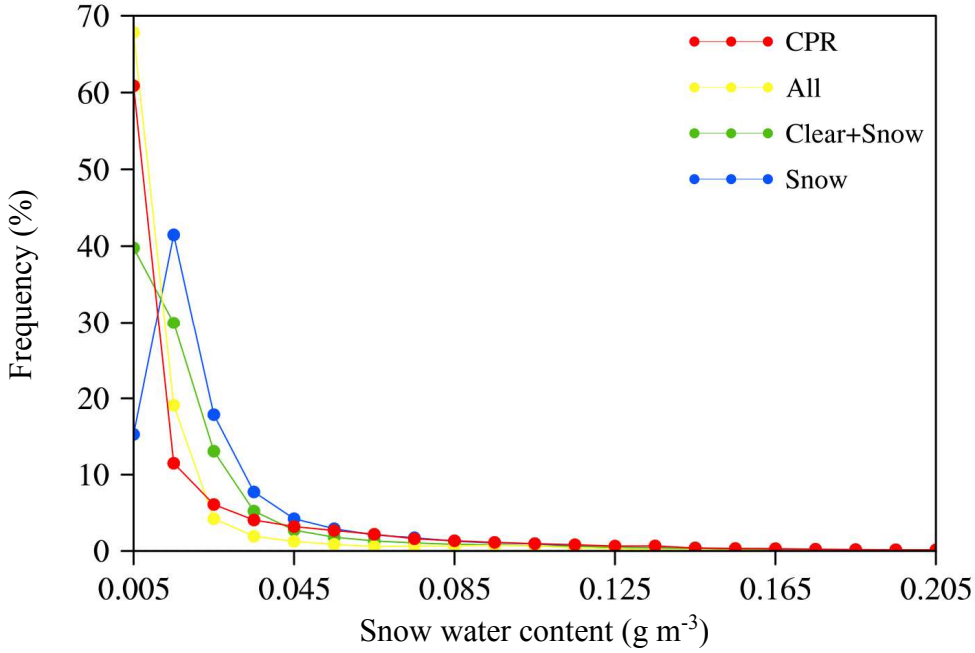

Fig. 6.11. Occurrence frequency distributions of analyzed surface snow water content (red), retrieved surface snow water content using all profiles (yellow), retrieved surface snow water content using clear–sky and snowfall profiles (green), and retrieved surface snow water content using snowfall profiles (blue).

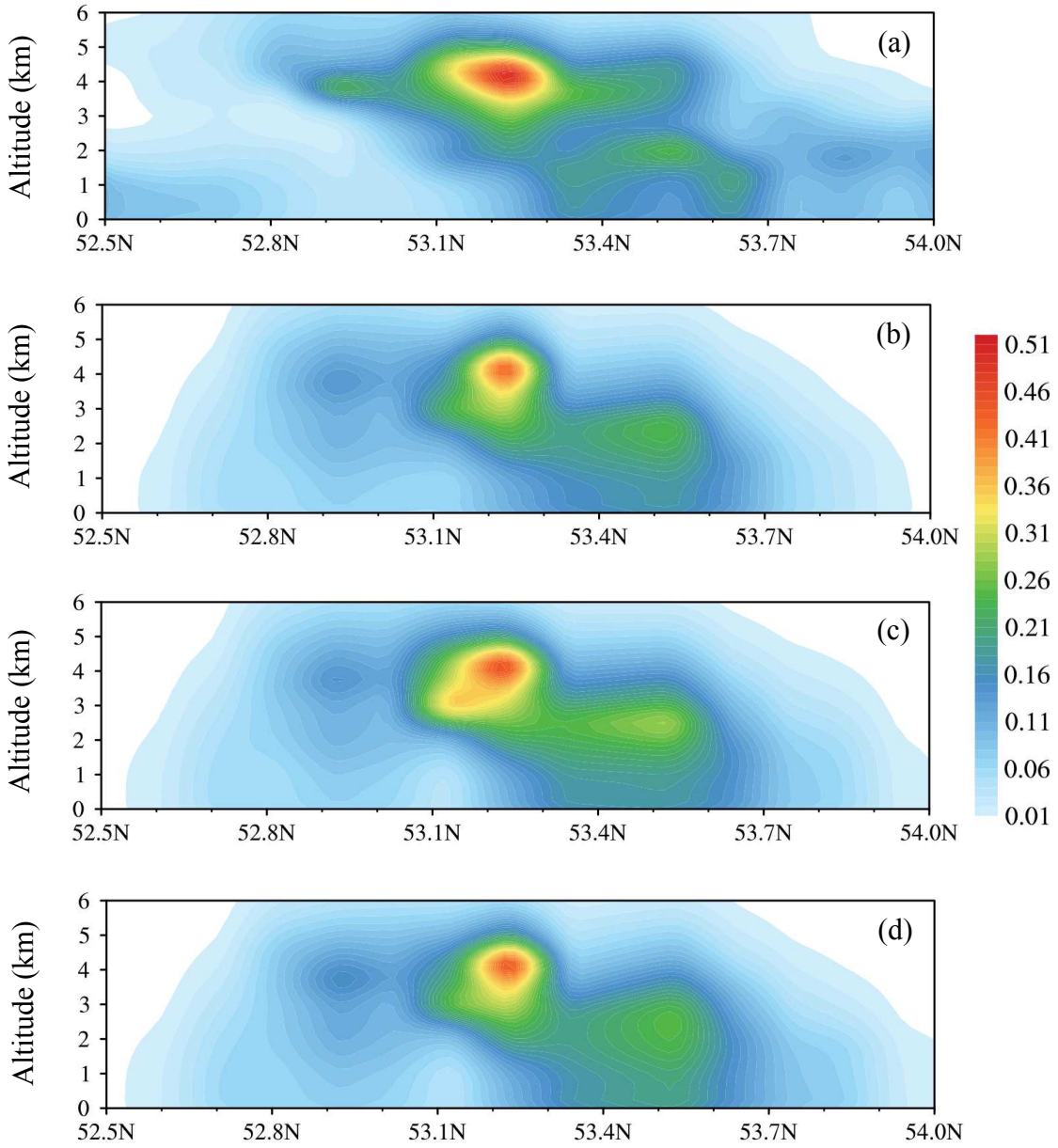

Fig. 6.12. Vertical cross sections of (a) analyzed snow water content, retrieved snow water content using (b) full database, (c) subsets of the database with moisture constraint, (d) subsets of the database with temperature constraint, (e) CPR initial snow water content, and (f) retrieved snow water content using CPR initial estimate as database for a case on March 11, 2015 (unit: g m^{-3}).

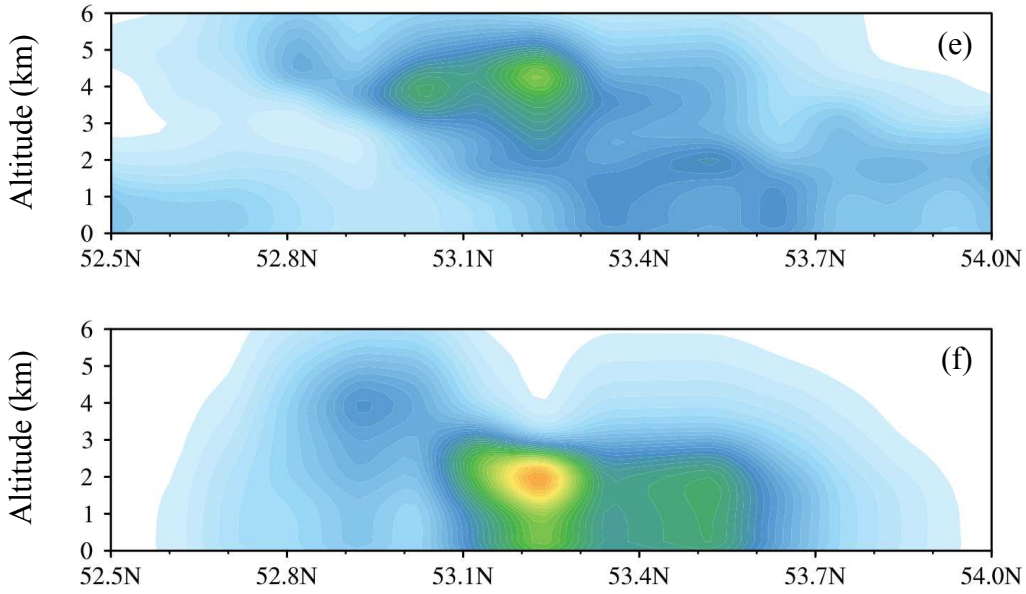

Fig. 6.12. Continued.

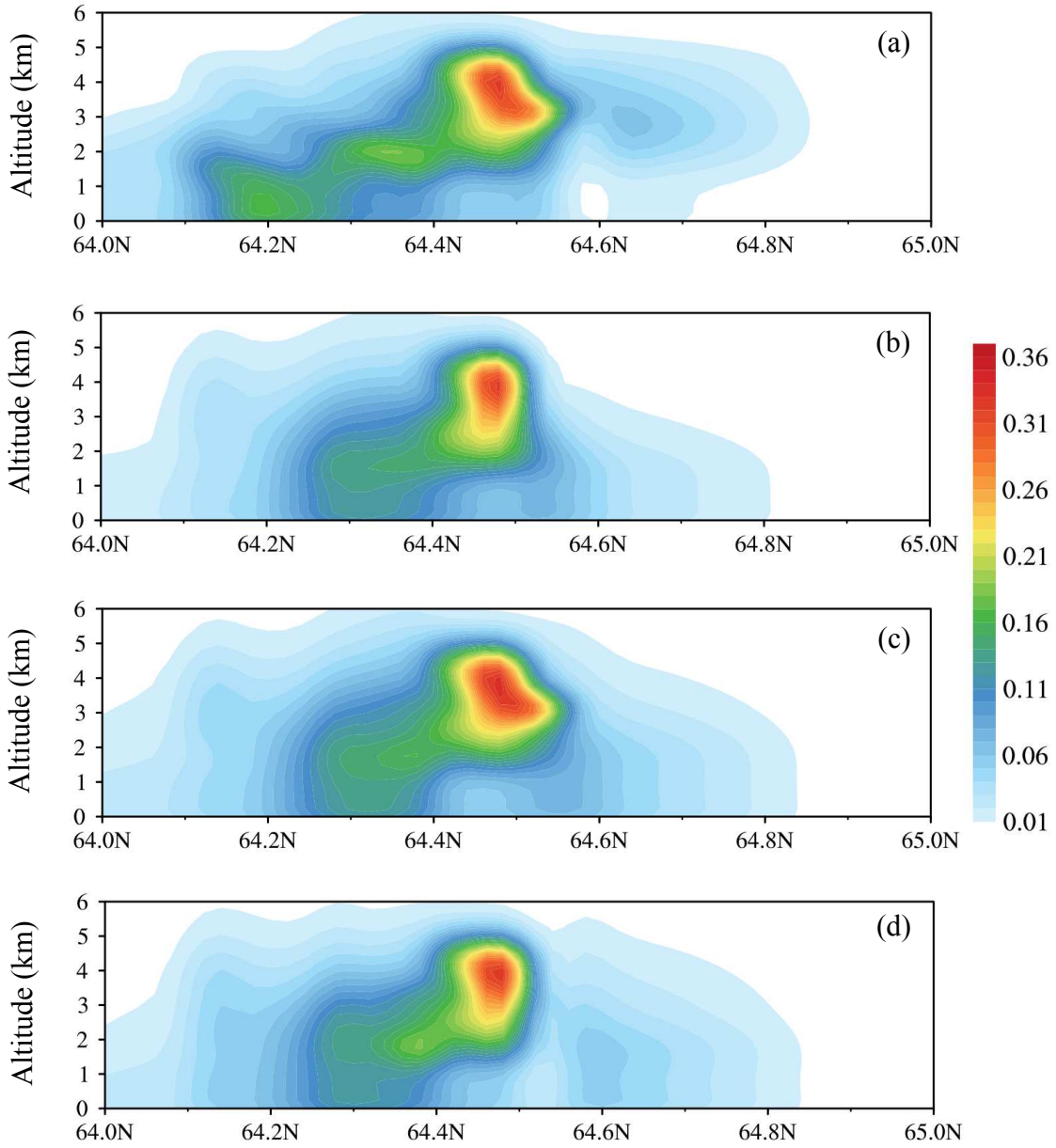

Fig. 6.13. Same as Fig. 6.12 except for a single case on December 5, 2014.

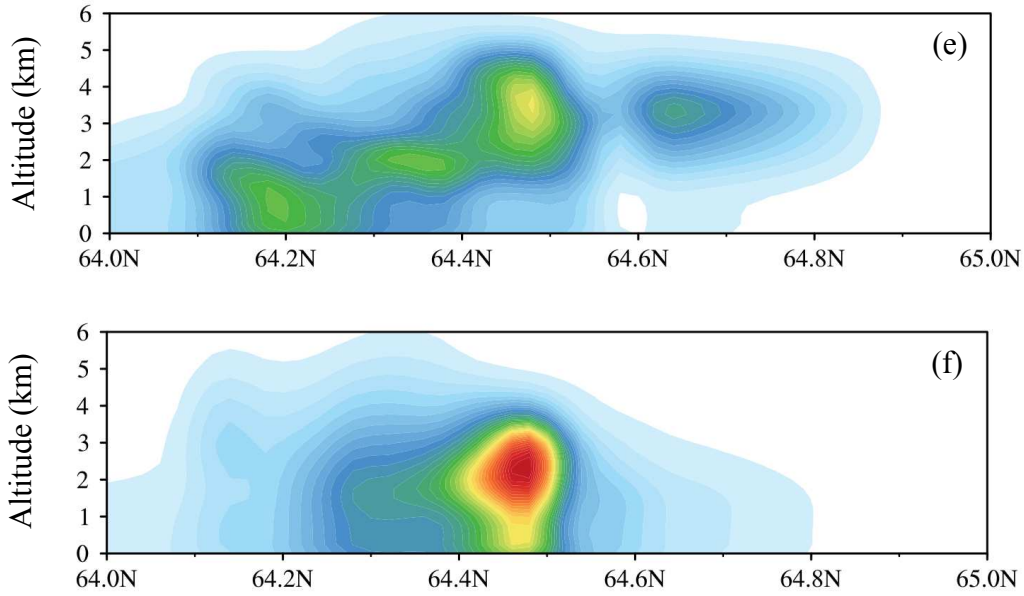

Fig. 6.13. Continued.

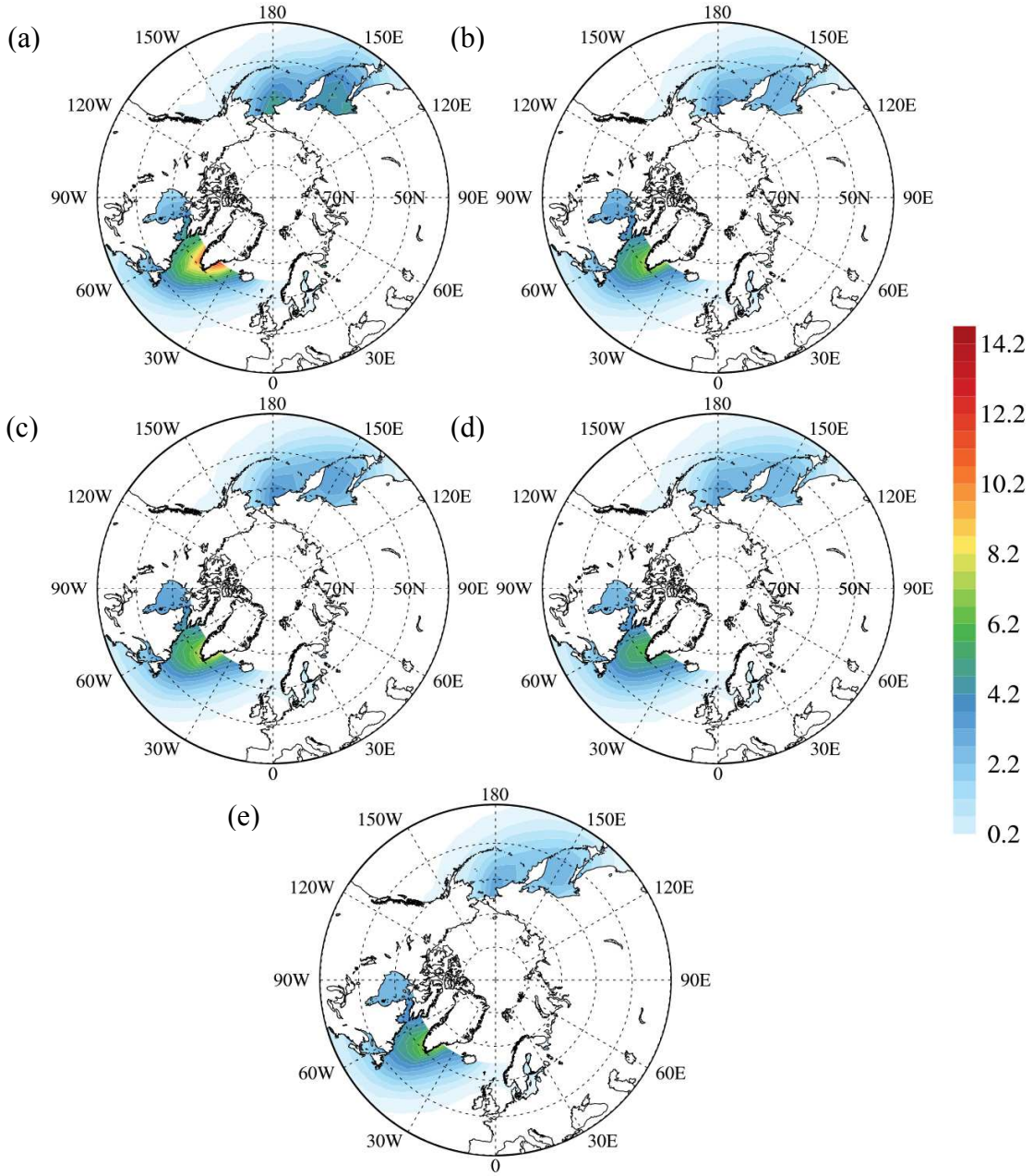

Fig. 6.14. Northern hemisphere mean distributions of surface snow water content (unit: mg m^{-3}) within $5° \times 5°$ boxes over ocean for year 2015 retrieved from (a) CPR radar reflectivities, and GMI brightness temperatures using (b) full database, (c) subsets of the database with moisture constraint, (d) subsets of the database with temperature constraint, and (e) CPR initial snow water content profiles as database.

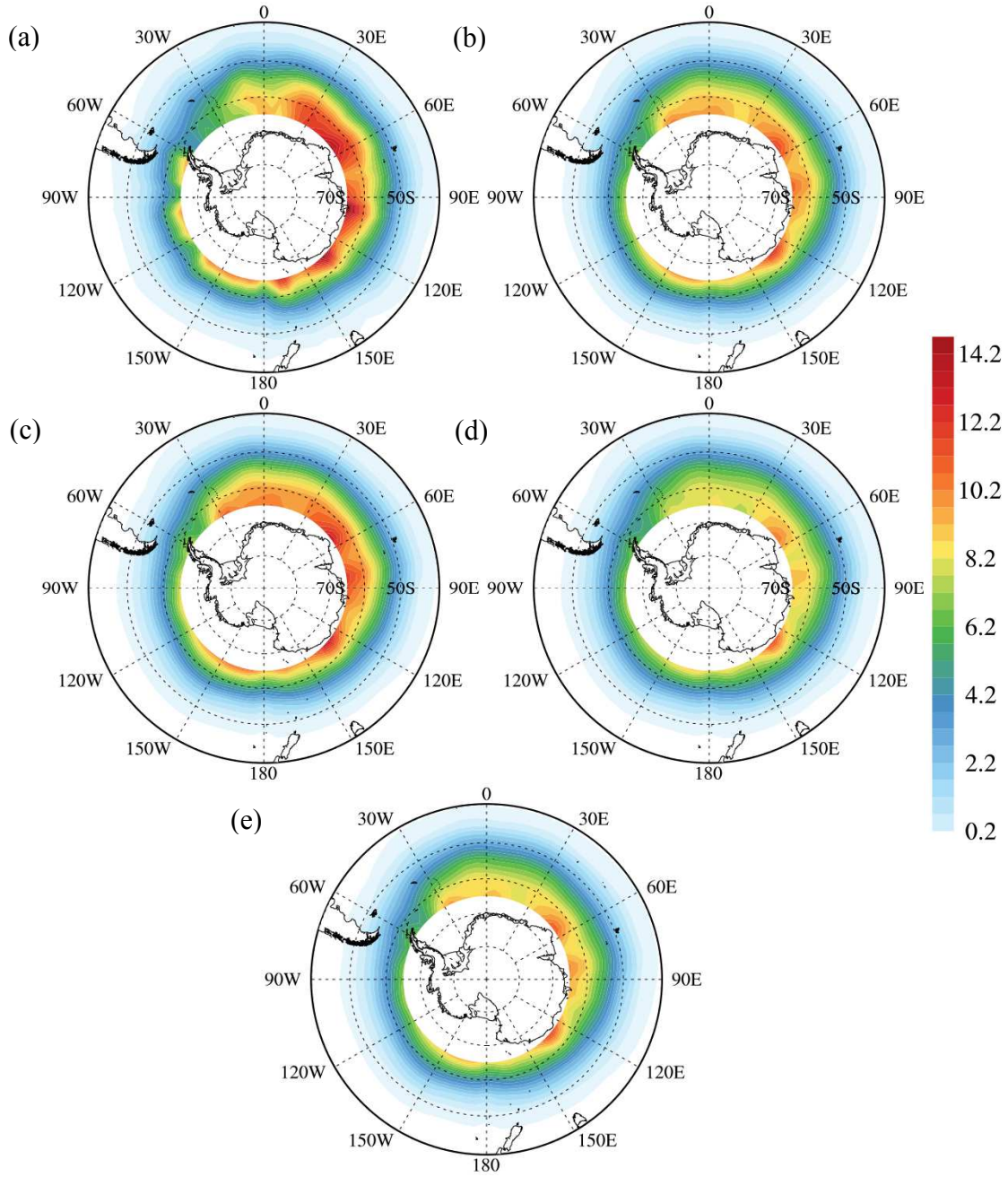

Fig. 6.15. Same as Fig. 6.14 except for southern hemisphere.

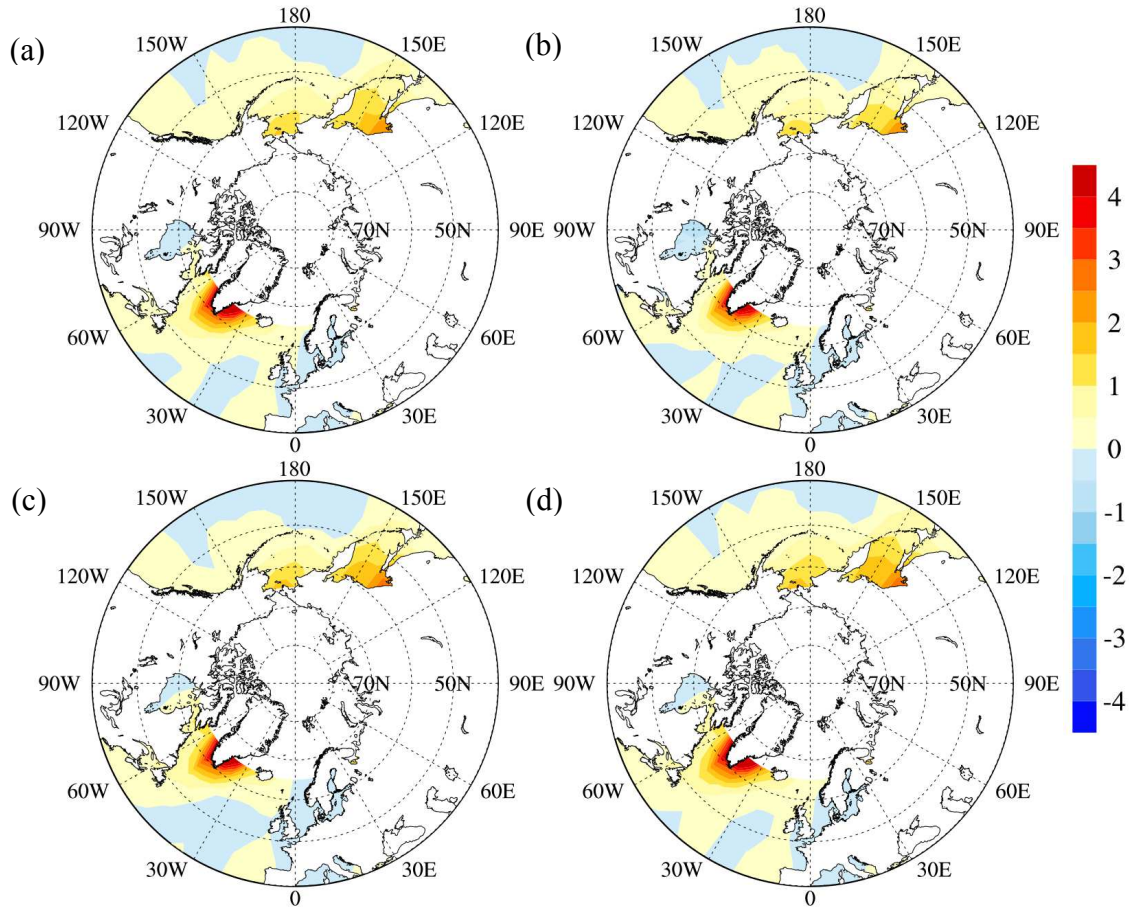

Fig. 6.16. Differences of northern hemisphere mean surface snow water contents (unit: mg m^{-3}) within 5°×5° boxes over ocean for year 2015 between those retrieved from CPR radar reflectivities and those retrieved from GMI brightness temperatures using (a) full database, (b) subsets of the database with moisture constraint, (c) subsets of the database with temperature constraint, and (d) CPR initial snow water content profiles as database.

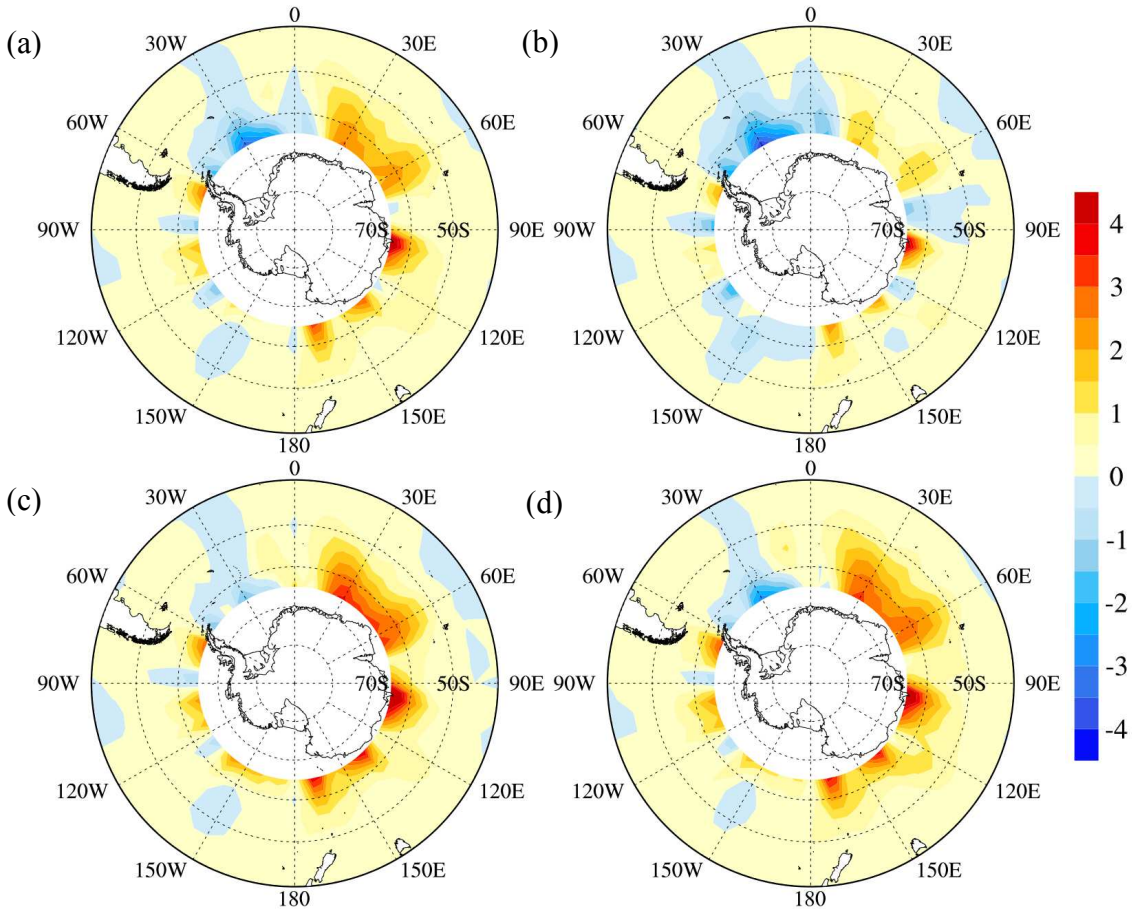

Fig. 6.17. Same as Fig. 6.16 except for southern hemisphere.

CHAPTER 7

SUMMARY AND DISCUSSIONS

While spaceborne microwave measurements have been widely used in rainfall studies, the application of spaceborne microwave instruments on snowfall detection is still in an early stage. Not many microwave sensors have suitable channels for capturing snow scattering signatures. With the launch of GPM core satellite, the carried DPR and GMI provide abundant observational data for global snowfall estimation. By combining them with the CloudSat CPR, it is able to study falling snow globally and its impact on climatological and hydrological cycles in depth. The aim of this study is to better understand the microphysics of snowflakes and the process of snow precipitation using spaceborne microwave measurements from active and passive sensors. To achieve this goal, we analyzed the triple-frequency radar signatures from the collocated CPR and DPR measurements in different types of snow clouds, assessed the skills to simulate observations at the GMI high frequency channels by radiative transfer models under snowfall conditions, and developed a snow water retrieval algorithm for measurements at GMI high frequency channels using the variational method.

We firstly examined the triple-frequency radar signatures by combining the DPR and CPR radar reflectivities. A clear difference in triple-frequency radar signatures is observed between stratiform and convective clouds. By analyzing the modeled backscattering properties of various snow particles from simple crystals to complicated aggregates, it is shown that the difference in triple-frequency radar signatures is likely resulted by the prevalent particle modes in stratiform and convection clouds. Namely, there are abundant large unrimed snow particles with low density in stratiform snow clouds, while convective snow clouds mainly contain dense small rimed snowflakes. The dependence of snowflake types on temperature is also investigated.

As indicated by our results, the large unrimed snow particles are dominant over warm temperatures, while the small rimed snow particles are popular over a wide range of temperature.

The assessment of observations at the GMI high frequency channels of 166 and 183 GHz with model simulations under snowfall conditions is then provided before we apply their data to snowfall studies. A radiative transfer model that includes the single scattering properties of nonspherical snowflakes based on DDA modeling results is used to simulate these channels. The input snow water content profiles are derived from the CPR measurements by developing a Z_e–SWC relation. As shown by our results, the total biases of observation minus simulation under snowfall conditions are smaller than 1 K except for the 166H channel with a bias of about 3 K. Further investigations show that the large biases for GMI channels at 166 and 183 GHz are mainly caused by the errors in radiative transfer model inputs. In shallow snow cells, cloud liquid water may be abundant and contribute significantly to the observed brightness temperatures. The biases in cloud liquid water profiles lead to the large biases in simulated brightness temperatures. This condition affects the 166H channel mostly, since this channel is more sensitive to surface emission. In deep convective snow clouds, the CPR radar reflectivities may experience strong attenuation and the GMI measurements are possibly prone to some negative sampling biases. Under this condition, the simulated brightness temperatures are positively biased. The 166 V/H channels are mostly affected by this problem.

We finally propose a snowfall retrieval algorithm for GMI by utilizing its channels at 89 GHz and higher frequencies. The experiment setups are mainly adopted from the study of the above assessment on the GMI high frequency channels. An optimized *a priori* database is developed for a Bayesian retrieval method. A 1D–Var optimization method is employed to maximize the physical consistency between snow water content profiles and observed brightness

temperatures. It is found that the adjustments on snow water content profiles can be substantial for deep convective clouds. All snow water content profiles collected from a two–year time period are optimized through 1D–Var method for creating the *a priori* database. It is seen that the large biases of observation minus simulation associated with shallow and deep convective snow clouds are effectively removed after the 1D–Var optimization. The standard deviations of observation minus simulation are decreased to a similar magnitude of defined observation errors after the 1D–Var optimization, indicating the success of this variational method.

After developing this optimized database, a Bayesian retrieval method is applied to retrieve snow water from brightness temperature at GMI channels at 89 GHz and higher frequencies. From two case studies, it is shown that the vertical structure of retrieved snow water content profile can be improved by the 1D–Var optimization method. The global mean distributions of surface snow water content over ocean is then retrieved for one year. The results show that the distributions of GMI retrieved surface snow water are closer to the CPR retrievals after applying the 1D–Var optimization method to *a priori* database. In addition, it is noticed that using total precipitable water to subset the database can improve the GMI retrievals, while using 2–m air temperature to subset the databases will slightly degrade the GMI retrievals.

We have presented the applications of spaceborne microwave sensors on snowfall studies. The results above can improve many aspects of snowfall studies. Specifically, the snowflake type is thought to be a major uncertainty source in snowfall retrievals [*Kulie et al.*, 2010], the results in Chapter 4 provide a possible approach to reduce this type of uncertainty by utilizing triple-frequency radar measurements. Chapter 5 provides an applicable method in simulating observations at microwave high frequency channels, which is potentially beneficial for numerical predictions. As shown by *Geer et al.* [2018], the data assimilation of microwave

measurements has been extended from clear–sky to all weather conditions in recent years. Accurate radiative model simulation is crucial to successful data assimilation under snowfall conditions. The passive snowfall retrieval algorithm developed in Chapter 6 can be used to retrieve the global three–dimensional distribution of snow water over ocean. It will certainly enrich the data sources of global snowfall events and increase our knowledge in snow precipitation processes. Future work may include a study in the relationship between snowflake structures and environmental parameters using triple-frequency radar measurements. We also plan to evaluate our GMI snowfall retrieval algorithm by comparing its estimates with the independent data sources.

BIBLIOGRAPHY

Adler, R. F., C. Kidd, G. Petty, M. Morrissey, and M. H. Goodman (2001), Intercomparison of global precipitation products: The third precipitation intercomparison project (PIP-3), *Bull. Am. Meteorol. Soc.*, **82**, 1377 –1396.

Aonashi, K., and Coauthors (2009), GSMaP passive microwave precipitation retrieval algorithm: Algorithm description and validation, *J. Meteor. Soc. Japan*, **87A**, 119–136.

Auligné, T., A. P. McNally, and D. P. Dee (2007), Adaptive bias correction for satellite data in a numerical weather prediction system, *Q. J. R. Meteorol. Soc.*, **133**, 631-642.

Barber, P., and C. Yeh (1975), Scattering of electromagnetic waves by arbitrarily shaped dielectric bodies, *Appl. Opt.*, **14**, 2864–2872.

Battaglia, A., C. D. Westbrook, S. Kneifel, P. Kollias, N. Humpage, Löhnert U, J. Tyynelä, and G. W. Petty (2014), G band atmospheric radars: New frontiers in cloud physics, *Atmos. Meas. Tech.*, **7(6)**. 1527–1546.

Bauer, P., A. J. Geer, P. Lopez, and D. Salmond (2010), Direct 4D-Var assimilation of all-sky radiances. Part I: Implementation, *Quart. J. Roy. Meteor. Soc.*, **136**, 1868–1885.

Bennartz, R., and P. Bauer (2003), Sensitivity of microwave radiances at 85-183 GHz to precipitation ice particles. *Radio Sci.*, **38**, D8075.

Boukabara, S.-A., and Coauthors (2011), MiRS: An all-weather 1DVAR satellite data assimilation and retrieval system, *IEEE Trans. Geosci. Remote Sens.*, **49**, 3249–3272.

Braham, R. R., Jr. (1990), Snow particle size spectra in lake effect snows, *J. Appl. Meteorol.*, **29**, 200– 207.

Cao, Q., and et al. (2014), Snowfall Detectability of NASA's CloudSat: the First Cross-Investigation of its 2c-SnowProfile Product and National Multi-Sensor Mosaic QPE (NMQ) Snowfall Data, *Prog. Electromagn. Res.*, **148**, 55-61.

Casella, D., G. Panegrossi, and et al. (2017), Evaluation of the GPM-DPR snowfall detection capability: Comparison with CloudSat-CPR, *Atmos. Res.*, **197**, 64–75.

Connolley, W. M. (1996), The Antarctic temperature inversion, *Int. J. Climatol.*, **16**, 1333–1342.

Curry, J. A., G. Liu, and P. J. Webster (1996), Evaluation of the surface fresh water flux in the North Atlantic Ocean and its impact on the ocean surface buoyancy flux, paper presented at Eighth Conference on Air-Sea Interaction and Conf. on the Global Ocean-Atmosphere-Land System (GOALS), *Am. Meteorol. Soc.*, Boston, Mass.

Curry, J. A., W. B. Rossow, D. Randall, and J. L. Schramm (1996), Overview of Arctic cloud and radiation characteristics, *J. Clim.*, **9**, 1731–1764.

Draine, B. T., and P. J. Flatau (1994), Discrete-dipole approximation for scattering calculations, *J. Opt. Soc. Am. A Opt. Image Sci.*, **11**, 1491– 1499.

Duncan, D. I., and C. D. Kummerow (2016), A 1DVAR retrieval applied to GMI: Algorithm description, validation, and sensitivities, *J. Geophys. Res. Atmos.*, **121**, 7415–7429.

Ebert, E. E., M. J. Manton, P. A. Arkin, R. J. Allam, C. E. Holpin, and A. Gruber (1996), Results from the GPCP algorithm intercomparison programme, *Bull. Amer. Meteor. Soc.*, **77**, 2875–2887.

Ebert, E. E., and M. J. Manton (1998), Performance of satellite rainfall estimation algorithms during TOGA COARE, *J. Atmos. Sci.*, **55**, 1537–1557.

Evans, K. F., S. J. Walter, A. J. Heymsfield, and G. M. McFarquhar (2002), Submillimeter-Wave Cloud Ice Radiometer: Simulations of retrieval algorithm performance, *J. Geophys. Res.*, **107(D3)**, 4028.

Geer, A., and P. Lopez (2010), Direct 4D-Var assimilation of all sky radiances. Part II: Assessment, *Quart. J. Roy. Meteor. Soc.*, **136**, 1886–1905.

Geer, A., and P. Bauer (2011), Observation errors in all-sky data assimilation, *Quart. J. Roy. Meteor. Soc.*, **137**, 2024–2037.

Geer, A., and F. Baordo (2014), Improved scattering radiative transfer for frozen hydrometeors at microwave frequencies, *Atmos. Meas. Tech.*, **7**, 1839–1860.

Geer, A., K. Lonitz, P. Weston, and et al. (2018), All□sky satellite data assimilation at operational weather forecasting centres, *Q. J. R. Meteorol. Soc.*, **2018**, 1–27.

Guillou, C., W. Ellison, L. Eymard, K. Lamkaouchi, C. Prigent, G. Delbos, G. Balana, and S. A. Boukabara (1998), Impact of new permittivity measurements on sea surface emissivity modeling in microwaves, *Radio Sci.*, **33**, 649–667.

Hale, G. M., and M. R. Querry (1973), Optical constants of water in the 200 nm to 200 μm wavelength range, *Appl. Opt.*, **13**, 555–563.

Hamada, A., and Y. N. Takayabu (2015), Improvements in detection of light precipitation with the Global Precipitation Measurement Dual-Frequency Precipitation Radar (GPM/ DPR), *J. Atmos. Ocean. Technol.*, **33**, 653–667.

Heymsfield, A. J., Matrosov, S. Y., & Wood, N. B. (2016), Toward improving ice water content and snow-rate retrievals from radars. Part. I: X and W bands, emphasizing CloudSat, *J. Appl. Meteor. Climatol.*, **55**, 2063–2090.

Heymsfield, A. J., M. Krämer, N. B. Wood, A. Gettelman, P. R. Field, and G. Liu (2017), Dependence of the ice water content and snowfall rate on temperature, globally: Comparison of in situ observations, satellite active remote sensing retrievals, and global climate model simulations, *J. Appl. Meteorol. Climatol.*, **56**, 189–215.

Hiley, M. J., M. S. Kulie, and R. Bennartz (2011), Uncertainty Analysis for CloudSat Snowfall Retrievals, *J. Appl. Meteor. Climatol.*, **50**, 399–418.

Honeyager, R., G. Liu, and H. Nowell (2016), Voronoi diagram-based spheroid model for microwave scattering of complex snow aggregates, *J. Quant. Spectrosc. Radiat. Transf.*, **170**, 28–44.

Hou, A. Y., R. K. Kakar, S. Neeck, A. A. Azarbarzin, C. D. Kummerow, M. Kojima, R. Oki, K. Nakamura, and T. Iguchi (2014), The global precipitation measurement mission, *Bull. Am. Meteorol. Soc.*, **95**, 701–722.

Iguchi, T., R. Oki, E. A. Smith, and Y. Furuhama (2002), Global precipitation measurement program and the development of dual-frequency precipitation radar (in Japanese), *J. Commun. Res. Lab.*, **49**, 37–45.

Islam, T., P. K. Srivastava, G. P. Petropoulos, and S. K. Singh (2015), Reduced major axis approach for correcting GPM/GMI radiometric biases to coincide with radiative transfer simulation, *J. Quantum Spectrosc. Radiative. Transf.*, **168**, 40–45.

Kazumori, M., and S. J. English (2015), Use of the ocean surface wind direction signal in microwave radiance assimilation, *Q. J. R. Meteorol. Soc.*, **141**, 1354–1375.

Kidd, C., and V. Levizzani (2011), Status of satellite precipitation retrievals. *Hydrol. Earth Syst. Sci.,* **7**, 8157–8177.

Kim, J-H, D-B Shin, and C. D. Kummerow (2013), Impacts of a priori databases using six WRF microphysics schemes on passive microwave rainfall retrievals, *J. Atmos. Oceanic Technol.*, **30**, 2367–2381.

Kienzle, S. W. (2008), A new temperature based method to separate rain and snow, *Hydrol. Process*., **22**, 5067-5085.

Kneifel, S., M. S. Kulie, and R. Bennartz (2011), A triple□frequency approach to retrieve microphysical snowfall parameters, *J. Geophys. Res.*, **116**, D11203.

Kneifel, S., A. von Lerber, J. Tiira, D. Moisseev, P. Kollias, and J. Leinonen (2015), Observed relations between snowfall microphysics and triple-frequency radar measurements, *J. Geophys. Res. Atmos*, **120**, 6034-6055.

Kneifel, S., P. Kollias, A. Battaglia, J. Leinonen, M. Maahn, H. Kalesse, and F. Tridon (2016), First observations of triple-frequency radar Doppler spectra in snowfall: Interpretation and

applications, *Geophys. Res. Lett.*, **43**, 2225–223.

Kubota, T., T. Iguchi, M. Kojima, L. Liao, T. Masaki, H. Hanado, R. Meneghini, and R. Oki (2016), A Statistical Method for Reducing Sidelobe Clutter for the Ku-Band Precipitation Radar on board the GPM Core Observatory, *J. Atmos. Oceanic Technol.,* **33**, 1413–1428.

Kulie M. S., R. Bennartz, T. J. Greenwald, Y. Chen, and F. Weng (2010), Uncertainties in microwave properties of frozen precipitation: Implications for remote sensing and data assimilation, *J. Atmos. Sci.*, **67**, 3471-87.

Kulie, M. S., M. J. Hiley, R. Bennartz, S. Kneifel, and S. Tanelli (2014), Triple frequency radar reflectivity signatures of snow: Observations and comparisons to theoretical ice particle scattering models, *J. Appl. Meteorol. Climatol.*, **53**, 1080–1098.

Kulie, M. S., L. Milani, N. B. Wood, S. A. Tushaus, R. Bennartz, and T. S. L'Ecuyer (2016), A Shallow Cumuliform Snowfall Census Using Spaceborne Radar, *J. Hydrometeor.*, **17**, 1261–1279.

Kunkee, D. B., S. D. Swadlley, G. A. Poe, Y. Hong, and M. F. Werner (2008), Special Sensor Microwave Imager Sounder (SSMIS) radiometric calibration anomalies—Part I: Identification and characterization, *IEEE Trans. Geosci. Remote Sens.*, **46**, 1017–1033.

Kummerow, C., and Coauthors (2000), The status of the Tropical Rainfall Measuring Mission (TRMM) after two years in orbit, *J. Appl. Meteor.*, **39**, 1965–1982.

Kummerow, C., and Coauthors (2001), The evolution of the Goddard profiling algorithm (GPROF) for rainfall estimation from microwave sensors, *J. Appl. Meteor*., **40**, 1801–1820.

Kummerow, C., S. Ringerud, J. Crook, D. Randel, and W. Berg (2011), An observationally generated a priori database for microwave rainfall retrievals, *J. Atmos. Oceanic Technol.*, **28**, 113–130.

Kummerow, C., D. Randel, M. Kulie, N-Y Wang, R. Ferraro, S. J. Munchak, and V. Petkovic (2015), The evolution of the Goddard profiling algorithm to a fully parametric scheme, *J. Atmos. Oceanic Technol.*, **32**, 2265–2280.

Levizzani, V., S. Laviola, and E. Cattani (2011), Detection and Measurement of Snowfall from Space, *Remote Sens.*, **3**, 145–166.

Leinonen, J., S. Kneifel, D. Moisseev, J. Tyynelä, S. Tanelli, and T. Nousiainen (2012), Nonspheroidal behavior in millimeter-wavelength radar observations of snowfall, *J. Geophys. Res.*, **117**, D18205.

Leinonen, J., and D. Moisseev (2015), What do triple-frequency radar signatures reveal about aggregate snowflakes? *J. Geophys. Res. Atmos.*, **120**, 229–239.

Leinonen, J., and W. Szyrmer (2015), Radar signatures of snowflake riming: A modeling study, *Earth and Space Science*, **2**, 346–358.

Liu, G. (1998), A fast and accurate model for microwave radiance calculations, *J. Meteor. Soc. Japan*, **76**, 335–343.

Liu, G., and J. A. Curry (1997), Precipitation characteristics in the GIN seas determined using satellite microwave data, *J. Geophys. Res.*, **102**, 13,987–13,997.

Liu, G., and J. A. Curry (1999), Tropical ice water amount and its relations to other atmospheric hydrological parameters as inferred from satellite data, *J. Appl. Meteorol.*, **38**, 1182–1194.

Liu, G. (2004), Approximation of single scattering properties of ice and snow particles for high microwave frequencies, *J. Atmos. Sci.*, **61**, 2441–2456.

Liu, G. (2008a), Deriving snow cloud characteristics from CloudSat observations, *J. Geophys. Res.*, **113**, D00A09.

Liu, G. (2008b), A database of microwave single-scattering properties for nonspherical ice particles, *Bull. Am. Met. Soc.*, **89**, 1563–1570.

Liu, G., and E.-K. Seo (2013), Detecting snowfall over land by satellite high-frequency microwave observations: The lack of scattering signature and a statistical approach, *J. Geophys. Res. Atmos.*, **118**, 1376–1387.

Liu, Q., and F. Weng (2005), One-dimensional variational retrieval algorithm of temperature, water vapor, and cloud water profiles from advanced microwave sounding unit (AMSU), *IEEE Trans. Geosci. Remote Sens.*, **43**, 1087–1095.

Lu, Q., W. Bell, P. Bauer, N. Bormann, and C. Peubey (2011), Characterizing the FY-3A Microwave Temperature Sounder Using the ECMWF Model, *J. Atmos. Oceanic Technol.*, **28**, 1373–1389.

Manabe T., H. Liebe, and G. Hufford (1987), Complex permittivity of water between 0 and 30 THz, Cof. Dig., Twelfth Int. Cof. on Infrared and Millimeter Waves, Lake Buena Vista, Florida, 229–230.

Marzano, F. S., A. Mugnai, G. Panegrossi, N. Pierdicca, E.A. Smith, and J. Turk (1999), Bayesian estimation of precipitating cloud parameters from combined measurements of spaceborne microwave radiometer and radar, *IEEE Trans. Geosci. Remote Sens.*, **37**, 596–613.

Matrosov, S. Y. (2007), Modeling backscatter properties of snowfall at millimeter wavelengths, *J. Atmos. Sci.*, **64**, 1727 – 1736.

Matrosov, S. Y. (2015), Evaluations of the Spheroidal Particle Model for Describing Cloud Radar Depolarization Ratios of Ice Hydrometeors, *J. Atmos. Oceanic Technol.*, **32**, 865–879.

Matrosov, S. Y., A. J. Heymsfield, and Z. Wang (2005), Dual-frequency radar ratio of nonspherical atmospheric hydrometeors, *Geophys. Res. Lett.,* **32,** L13816.

Matrosov, S. Y., and A. Battaglia (2009), Influence of multiple scattering on CloudSat measurements in snow: A model study, *Geophys. Res. Lett.*, **36**, L12806.

Meng, H., J. Dong, R. Ferraro, B. Yan, L. Zhao, C. Kongoli, N.-Y. Wang, and B. Zavodsky (2017), A 1DVAR-based snowfall rate retrieval algorithm for passive microwave radiometers, *J. Geophys. Res. Atmos.*, **122**, 6520–6540**.**

Moreau, E., P. Bauer, and F. Chevallier (2003), Variational retrieval of rain profiles from spaceborne passive microwave radiance observations, *J. Geophys. Res.*, **108(D16)**, 4521.

Mugnai, A., E. A. Smith, and G. J. Tripoli (1993), Foundations for statistical–physical precipitation retrieval from passive microwave satellite measurements. Part II: Emission-source and generalized weighting-function properties of a time-dependent cloud-radiation model, *J. Appl. Meteor.*, **32**, 17–39.

Noh, Y.-J., G. Liu, E.-K. Seo, J. R. Wang, and K. Aonashi (2006), Development of a snowfall retrieval algorithm at high microwave frequencies, *J. Geophys. Res.*, **111**, D22216.

Nowell, H., G. Liu, and R. Honeyager (2013), Modeling the microwave single- scattering properties of aggregate snowflakes, *J. Geophys. Res. Atmos.*, **118**, 7873–7885.

Olson, W. S., H. Masunaga, and the GPM Combined Radar-Radiometer Algorithm Team (2011), GPM Combined Radar-Radiometer Precipitation ATBD (Version 2).

Olson, W. S., C. D. Kummerow, G. M. Heymsfield, and L. Giglio (1996), A method for combined passive-active microwave retrievals of cloud and precipitation profiles, *J. Appl. Meteorol.*, **35**, 1763– 1789.

Passive Microwave Algorithm Team Facility (2017), Global Precipitation Measurement (GPM) Mission Algorithm Theoretical Basis Document (GPROF2017 Version 1).

Panegrossi, G., and Coauthors (1998), Use of cloud model microphysics for passive microwave-based precipitation retrieval: Significance of consistency between model and measurement manifolds, *J. Atmos. Sci.*, **55**, 1644–1673.

Petty, G. W. (2006), A First Course in Atmospheric Radiation, Sundog Publishing, Madison, 2nd edition.

Petty, G. W., and W. Huang (2010), Microwave back scatter and extinction by soft ice spheres and complex snow aggregates, *J. Atmos. Sci.*, **67**, 769–87.

Pruppacher, H. R., J. D. Klett (1997), Microphysics of Clouds and Precipitation: Second Revised and Enlarged Edition with an Introduction to Cloud Chemistry and Cloud Electricity, Kluwer Academic Publishers, Norwell, Massachusetts.

Rysman, J.-F., G. Panegrossi, P. Sanò, A. C. Marra, S. Dietrich, L. Milani, and M. S. Kulie (2018), SLALOM: An All-Surface Snow Water Path Retrieval Algorithm for the GPM Microwave Imager, *Remote Sens.*, **10**, 1278.

Rodgers, C. D. (1976), Retrieval of atmospheric temperature and composition from remote measurements of thermal radiation, *R. Geophys. Space Phys.*, **14**, 609-624.

Salonen, E., and S. Uppala (1991), New prediction method of cloud attenuation, *Electron. Lett.*, **27**, 1106–1108.

Sassen, K., and Z. Wang (2008), Classifying clouds around the globe with the CloudSat radar: 1-year of results, *Geophys. Res. Lett.*, **35**, L04805.

Senn, P., and E. Barthazy (2004), In-situ observations and modeling of aggregation of snowfall, *Proc. European Conf. on Radar Meteorology* (ERAD-2004), Visby, Sweden, Copernicus GmbH, 253–256.

Schluessel, P., and H. Luthardt (1991), Surface wind speeds over the North Sea from Special Sensor Microwave/Imager observations, *J. Geophys. Res.*, **96**, 4845–4853.

Segelstein, D. J. (1981), The complex refractive index of water, master thesis, University of Missouri-Kansas City.

Sekhon, R. S., and R. C. Srivastava (1970), Snow size spectra and radar reflectivity, *J. Atmos. Sci.*, **27**, 299– 307.

Seo, E.-K., and G. Liu (2005), Retrievals of cloud ice water path by combining ground cloud radar and satellite high-frequency microwave measurements near the ARM SGP site, *J. Geophys. Res.*, **110**, D14203.

Seo, E.-K., S. Yang, M. Grecu, G. Ryu, G. Liu, S. Hristova-Veleva, Y. Noh, Z. Haddad, and J. Shin (2016), Optimization of Cloud-Radiation Databases for Passive Microwave Precipitation Retrievals over Ocean, *J. Atmos. Oceanic Technol.*, **33**, 1649–1671.

Sims, E.M., and G. Liu (2015), A Parameterization of the Probability of Snow–Rain Transition, *J. Hydrometeor.*, **16**, 1466–1477.

Skofronick-Jackson, G. M., M.-J. Kim, J. A. Weinman, and D.-E. Chang (2004), A physical model to determine snowfall over land by microwave radiometry, *IEEE Trans. Geosci. Remote Sens.*, **42**, 1047– 1058.

Skofronick-Jackson, G. M., B. T. Johnson and S. J. Munchak (2013), Detection Thresholds of Falling Snow From Satellite-Borne Active and Passive Sensors, *IEEE Trans. Geosci. Remote Sens.*, **51**, 4177-4189.

Stein, T. H. M., C. D. Westbrook, and J. C. Nicol (2014), Fractal geometry of aggregate snowflakes revealed by triple-wavelength radar measurements, *Geophys. Res. Lett.*, **42**, 176–183.

Stephens, G. L. (1994), Remote Sensing of the Lower Atmosphere: an Introduction, Oxford University Press, Oxford.

Stephens, G. L., et al. (2002), The CloudSat mission and the A-Train, *Bull. Am. Meteorol. Soc.*, **83**, 1771–1790.

Strutt, J. (1871), On the light from the sky, its polarization and colour. *Philos. Mag.*, **41**, 107–120, 274–279.

Toyoshima, K., H. Masunaga, and F. A. Furuzawa (2015), Early Evaluation of Ku- and Ka-Band Sensitivities for the Global Precipitation Measurement (GPM) Dual-Frequency Precipitation Radar (DPR), *SOLA*, **11**, 14–17.

Trenberth, K., L. Smith, T. Qian, A. Dai, and J. Fasullo (2007), Estimates of the global water budget and its annual cycle using observational and model data, *J. Hydrometeor.,* **8**, 758–769.

Turk, J. (2017), CloudSat-GPM Coincidence Dataset (version 2A).

Tyynelä, J., and V. Chandrasekar (2014), Characterizing falling snow using multi frequency dual-polarization measurements, *J. Geophys. Res. Atmos.*, **119**, 8268–8283.

Vivekanandan, J., G. Zhang, and M. K. Politovich (2001), An Assessment of Droplet Size and Liquid Water Content Derived from Dual-Wavelength Radar Measurements to the Application of Aircraft Icing Detection, *J. Atmos. Oceanic Technol.,* **18**, 1787–1798.

Viltard, N., C. Burlaud, and C. D. Kummerow (2006), Rain Retrieval from TMI Brightness Temperature Measurements Using a TRMM PR–Based Database, *J. Appl. Meteor. Climatol.*, **45**, 455–466.

Wang, Y., G. Liu, E-K Seo, and Y. Fu (2013), Liquid water in snowing clouds: Implications for satellite remote sensing of snowfall, *Atmos. Res.*, **131**, 60–72.

Warren, S. G., and R. E. Brandt (2008), Optical constants of ice from the ultraviolet to the microwave: A revised compilation, *J. Geophys. Res.*, **113**, D14220.

Weng, F., X. Zou, X. Wang, S. Yang, and M. D. Goldberg (2012), Introduction to Suomi national polar-orbiting partnership advanced technology microwave sounder for numerical weather prediction and tropical cyclone applications, *J. Geophys. Res.*, **117**, D19112.

Wood, N. B., T. S. L'Ecuyer, A. J. Heymsfield, G. L. Stephens, D. R. Hudak, and P. Rodrigues (2014), Estimating snow microphysical properties using collocated multisensor observations, *J. Geophys. Res. Atmos.*, **119**, 8941–8961.

BIOGRAPHICAL SKETCH

Mengtao Yin was born in Chengdu, Sichuan Province, China. He transferred to FSU in Fall, 2011. He received his Bachelor's degree in Meteorology at FSU in Spring, 2013. He then continued his graduate study at FSU. His Master's research is related to the applications of satellite hyperspectral infrared sounders on numerical forecasting. He received his Master's degree in Meteorology at FSU in Spring, 2015. He joined Dr. Guosheng Liu's lab in Fall, 2015 and mainly studies the applications of satellite microwave measurements on snowfall retrievals. He will graduate with his PhD degree in Spring, 2019.